CZECH TECHNICAL UNIVERSITY
IN PRAGUE

FACULTY OF NUCLEAR SCIENCES AND PHYSICAL
ENGINEERING

Department of Physics

MASTER'S THESIS

Structure of light hypernuclei in the framework of Fermionic Molecular Dynamics

B.C. Martin Schäfer

2015

Supervisor: RNDr. Jiří Mareš, CSc.

ČESKÉ VYSOKÉ UČENÍ TECHNICKÉ
V PRAZE

FAKULTA JADERNÁ A FYZIKÁLNĚ INŽENÝRSKÁ

Katedra fyziky

DIPLOMOVÁ PRÁCE

Struktura hyperjader v přístupu Fermionic Molecular Dynamics

B.c. Martin Schäfer

2015

Školitel: RNDr. Jiří Mareš, CSc.

Prohlášení

Prohlašuji, že jsem svou diplomovou práci vypracoval samostatně a použil jsem pouze podklady (literaturu, projekty, SW, atd.) uvedené v přiloženém seznamu.

Nemám závažný důvod proti použití tohoto školního díla ve smyslu § 60 Zákona č. 121/2000 Sb., o právu autorském, o právech souvisejících s právem autorským a o změně některých zákonů (autorský zákon).

Declaration

I declare that I wrote my Master's thesis independently and exclusively within the use of cited bibliography.

I agree with the usage of this thesis in the purport of the Act 121/2000 (Copyright Act).

V Praze dne ....

Martin Schäfer

Acknowledgement

Thesis tittle:	**Structure of light hypernuclei in the framework of Fermionic Molecular Dynamics**
Author:	Martin Schäfer
Department:	Department of Physics FNSPE CTU in Prague
Branch of study:	Experimental Nuclear and Particle Physics
Kind of thesis:	Master's thesis
Supervisor:	RNDr. Jiří Mareš, CSc.

Abstract: This thesis presents results of the first variational calculations of the s-shell hypernuclei $^4_\Lambda$H, $^4_\Lambda$He, and $^5_\Lambda$He and the p-shell hypernucleus $^7_\Lambda$Li, using our recently developed Fermionic Molecular Dynamics (FMD) code. The relevance of the variation of the parity projected trial state (VAP$^\pi$) is discussed. We found rather weak dependence of the Λ separation energies on the type of the V_{NN} potential in $^4_\Lambda$H and $^4_\Lambda$He, however, it significantly increased in $^5_\Lambda$He. We observed a substantial difference between the Λ separation energy spectra calculated using various $V_{\Lambda N}$ potentials. The proper choice of $V_{\Lambda N}$ as well as the Fermi momentum k_F, which enters the YNG $V_{\Lambda N}$ potentials as a parameter, is thus crucial. The YNG $V_{\Lambda N}$ potentials without charge symmetry breaking terms yield the shift between the Λ separation energy spectra of the mirror hypernuclei $^4_\Lambda$H and $^4_\Lambda$He which is opposite to that observed. The nuclear core modifications due to the presence of Λ in s-shell hypernuclei are negligible. However, in $^7_\Lambda$Li, the Λ pulls the α and d clusters in the ^{6}Li nuclear core closer together, which confirms the "glue-like" role of the Λ hyperon.

Název práce:	**Struktura hyperjader v přístupu Fermionic Molecular Dynamics**
Autor:	Martin Schäfer
Katedra:	Katedra fyziky FJFI ČVUT v Praze
Obor studia:	Experimentální jaderná a částicová fyzika
Druh práce:	Diplomová práce
Školitel:	RNDr. Jiří Mareš, CSc.

Abstrakt: Tato diplomová práce prezentuje výsledky prvních variačních výpočtů hyperjader s-slupky ${}^{4}_{\Lambda}$H, ${}^{4}_{\Lambda}$He, and ${}^{5}_{\Lambda}$He a hyperjádra p-slupky ${}^{7}_{\Lambda}$Li provedených prostřednictvím námi vyvinutého Fermionic Molecular Dynamics (FMD) kódu. Diskutovali jsme důležitost variace paritně vyprojektovaných testovacích stavů (VAP$^{\pi}$). U výpočtů ${}^{4}_{\Lambda}$H a ${}^{4}_{\Lambda}$He jsme zjistili velmi slabou závislost separačních energií Λ hyperonu na typu V_{NN} potenciálu, nicméně se významně zvýšila u ${}^{5}_{\Lambda}$He. Pozorovali jsme podstatný rozdíl mezi spektry separačních energií Λ pro různé $V_{\Lambda N}$. Správná volba $V_{\Lambda N}$, jakož i Fermiho hybnosti k_{F}, která vstupuje do YNG $V_{\Lambda N}$ potenciálů jako parametr je zásadní. YNG $V_{\Lambda N}$ potenciály neobsahující narušení nábojové symetrie dávají posun mezi spektry separačních energií Λ zrcadlových hyperjader ${}^{4}_{\Lambda}$H a ${}^{4}_{\Lambda}$He, který je opačný k pozorovanému. Modifikace jaderné struktury vlivem Λ je u hyperjader s-slupky zanedbatelná. Nicméně v případě ${}^{7}_{\Lambda}$Li dochází vlivem Λ k vzájemnému přiblížení α a d clusteru uvnitř ^{6}Li, což potvrzuje přitažlivou schopnost Λ hyperonu.

Klíčová slova: hyperjádra, FMD model, struktura jader, YNG potenciály, separační energie Λ, vazebná energie, rms poloměr, jednočásticová hustota

Contents

Chapter 1

Introduction

Hypernucleus is a nuclear system with non-zero strangeness containing besides neutrons and protons also one or more hyperons ($Y = \Lambda$, Σ, Ξ, Ω^-). The study of hypernuclei provides a unique opportunity to test models of baryon-baryon interactions, as well as various nuclear models. Since hyperons are not affected by Pauli blocking in the nucleus, they can penetrate deep in the nuclear interior and thus serve as a probe of the nuclear medium. Moreover, hypernuclear production and decay provide valuable information about reaction mechanisms and weak interaction.

Due to a rather short lifetime of hyperons (10^{-10} s) [1] the hyperon-nucleon scattering data are rather scarce and the form of the YN interaction is not so strictly constrained as in the NN case. Therefore, selected hypernuclear data are used as an input for various YN interaction models.

The range of experimentally observed hypernuclei is quite broad. It starts from the lightest hypernuclear system $^{3}_{\Lambda}$H and ends with the heavy hypernuclei $^{208}_{\Lambda}$Pb and $^{209}_{\Lambda}$Bi. So far, about 30 species of Λ hypernuclei have been observed. The most precise information, including γ-ray transitions, is available for s-shell and p-shell Λ hypernuclei up to mass number A=15 [2]. In general, Σ hypernuclei do not form bound systems, except $^{4}_{\Sigma}$He [3]. The existence of Ξ hypernuclei has not been confirmed with certainty yet. Finally, there is no evidence of Ω hypernuclei at present. As concerns systems with more than one hyperon, only three $\Lambda\Lambda$ hypernuclei were measured: $^{6}_{\Lambda\Lambda}$He [4], $^{10}_{\Lambda\Lambda}$Be [5] and $^{13}_{\Lambda\Lambda}$B [6].

The systematic study of hypernuclei has been performed for more than 60 years. The first hypernucleus was discovered by Danysz and Pniewski in 1953 [7]. They registered in emulsion experiment a slowly decaying nuclear fragment (hypernucleus) coming from the collision of the high energy (30 GeV) proton from cosmic rays with the Ag or Br nucleus. In the late 1950's and during 1960's, numerous hypernuclei were discovered in nuclear emulsions exposed to proton, pion, or K^- beams. However, at this time the experimental data were limited only to the Λ separation

energies of the ground states of hypernuclei up to mass A=15 [8].

Considerable progress in hypernuclear physics started with the advent of counter experiments in the 1970's. The number of discovered hypernuclear species has been more than doubled and their excitation spectra have been measured as well. Up to now, many experimental laboratories and collaborations have contributed to the increasing amount of information - CERN, BNL, KEK, JLab, JPARC, FINUDA, GSI, and MAMI-C [9, 10, 11, 12, 13] and the hypernuclear spectroscopy became well established experimental discipline. A new insight into the hypernuclear structure was provided by the high-resolution γ-ray spectroscopy using 4π Ge detectors [9] which allowed to measure excitation spectra of hypernuclei with astonishing resolution of few keV. Moreover, shrinking of the $^{7}_{\Lambda}$Li nuclear core due to the presence of Λ was measured for the first time [14]. The above mentioned scientific advances in experiment call for new, more sophisticated theoretical approaches.

The few-body Faddeev and Faddeev-Yakubovsky calculations are mainly limited by the size of a hypernucleus – they are used in the description of 3-body and 4-body hypernuclear systems ($^{3}_{\Lambda}$H, $^{4}_{\Lambda}$H, and $^{4}_{\Lambda}$He). Their advantage is that they can incorporate bare NN as well as ΛN interactions and also explicitly include $\Lambda N - \Sigma N$ mixing. Few-body calculations of weakly bound $^{3}_{\Lambda}$H [15, 16] and the Λ separation energy spectra of $^{4}_{\Lambda}$H, and $^{4}_{\Lambda}$He [16, 17] served as a precise test of various phenomenological as well as chiral NN and ΛN potential models.

The intrinsic structure of hypernuclear systems is often studied within various variational cluster calculations. In this approach, the nuclear core is represented by explicit neutron (n), proton (p), deuteron (d), triton (t), ^{3}He, and alpha (α) degrees of freedom. Until recently, there have been performed 3-body and 4-body calculations up to $^{13}_{\Lambda}$C ($\alpha\alpha\alpha\Lambda$) [18, 19]. Hiyama et al. have presented very recently the 5-body cluster calculation of $^{11}_{\Lambda\Lambda}$Be ($\alpha\alpha n\Lambda\Lambda$) [20]. This method uses predominantly effective G-matrix transformed NN, ΛN, and $\Lambda\Lambda$ potentials [21] which are further folded to the two-body interactions between the considered clusters.

The No Core Shell Model (NCSM) approach appeared suitable for the description of light Λ hypernuclei in the same range as cluster models. The *ab initio* nature of these calculations, as well as explicitly included Σ degrees of freedom make their theoretical predictions highly valuable. The s-shell $^{3}_{\Lambda}$H, $^{4}_{\Lambda}$H, and $^{4}_{\Lambda}$He hypernuclei [22] and p-shell Λ hypernuclei up to $^{13}_{\Lambda}$C [23] were calculated using the NN and ΛN chiral interactions.

The Λ separation energy spectra of s-shell, p-shell, and sd-shell hypernuclei were reproduced with relatively high precision using shell-model calculations [2, 24]. In this model, the core nucleus is described with a phenomenological Hamiltonian that allows to reproduce its nuclear structure very accurately. The ΛN interaction in

hypernuclei can thus be studied closely without being obscured by the NN part. The Λ hyperon is directly coupled to the eigenstates of well reproduced nuclear core in total angular momentum and isospin. The ΛN interaction is purely effective, however, $\Lambda N - \Sigma N$ mixing is considered explicitly.

The study of Λ hypernuclei up to $^{48}_{\Lambda}$Sc were performed using the Antisymmetrized Molecular Dynamics (AMD) model extended to hypernuclei (HyperAMD) [25, 26]. In AMD, each nucleon is represented by a Gaussian wave packet consisting of spatial, spin, and isospin parts. The Gaussian width parameters are equal for each nucleon but their position, spin, and isospin parameters may vary. The antisymmetrization of the many-body wave function is ensured by its Slater determinant form. The HyperAMD adopts the AMD approach for nucleons but also defines the Λ single-particle wave function as a superposition of several Gaussian wave packets which have the same width parameter as nucleons but their position and spin may be arbitrary. The values of variational parameters of single-particle states are obtained by minimizing the binding energy of the hypernuclear system.

Due to a large number of particles, heavier hypernuclei are exclusively described by mean field models. The most commonly used is the Relativistic Mean Field (RMF) approach [27] and Skyrme Hartree-Fock model [28, 29].

In recent studies [30, 31], the Fermionic Molecular Dynamics (FMD) model proved to be a valuable tool for the nuclear structure studies. Like AMD, it approximates the many-body wave function by a Slater determinant of Gaussian wave packets consisting of spatial, spin, and isospin parts. But unlike AMD, each nucleon of the system is represented by a Gaussian wave packet with its own width parameter. This property of the single-particle wave functions appeared to be crucial. It provides the FMD calculations with very flexible single-particle basis, which is suitable for the description of the cluster structure of light nuclei including halo nuclei. The clusterization in the nucleus emerges as a consequence of the underlying interactions between nucleons. However, the above virtues of FMD are achieved at the cost of greater computational complexity as well as theoretical difficulty. It is a question of serious interest how the presence of the Λ hyperon would affect the clusterization phenomena in nuclear system. The study of hypernuclei within FMD could yield new information about the ΛN interaction as well as Λ hypernuclear structure.

In this thesis, we present the first application of the Fermionic Molecular Dynamics model [32, 33, 34] in the structure calculations of the light s-shell Λ hypernuclei $^{4}_{\Lambda}$He, $^{4}_{\Lambda}$H, and $^{5}_{\Lambda}$He as well as the p-shell hypernucleus $^{7}_{\Lambda}$Li. We evaluated the Λ separation energy and rms radii of the hypernuclear ground and excited states for different NN and ΛN effective potentials in order to explore model dependence of

the calculations. We studied the effects in the nuclear core caused by the presence of Λ. In Chapter 2, we briefly introduce the FMD model together with applied projection techniques. The NN and ΛN interactions as well as V_{NN} and $V_{\Lambda N}$ potential models used in this work are presented in Chapter 3. The results of hypernuclear structure calculations are discussed in Chapter 4. We summarize our findings in Chapter 5 where our future plans are given as well. The antisymmetrization of the many-body wave function and definitions of calculated expectation values are briefly presented in Appendix A, while the details of analytical calculations of derivatives used during the minimization of the binding energy are summarized in Appendix B. The parameters and the operator form of the V_{NN} and $V_{\Lambda N}$ potentials are given in Appendix C. The FMD program developed for the purpose of this work is briefly introduced in Appendix D.

Chapter 2

Fermionic Molecular Dynamics model

Fermionic Molecular Dynamics is a non-relativistic many-body variational model which describes systems of N interacting fermions. The antisymmetrized many-body wave function is approximated by a Slater determinant with underlying single-particle wave functions represented by Gaussian wave packets.

The model was first introduced by Feldmeier in 1990 [32] in order to study heavy-ion reactions at energies below particle production. Already in this pioneering article, the first mention of the possibility of using FMD model to calculations of ground states properties of nuclei appeared. First FMD calculations of binding energies, R_{rms} radii and one-body densities in ^{4}He, ^{6}Li, ^{7}Li, ^{8}Be, ^{12}C and ^{16}O were published in 1995 [33]. Few years later, Feldmeier, Neff, Roth, and Schnack developed the new Unitary Correlation Operator Method (UCOM) [35] which allowed to describe nuclear ground states using more sophisticated NN potentials, such as Afnan-Tang S3M [36] or Malfliet-TjonV [37] potentials. The UCOM was further extended by Neff to include tensor correlations [38], which enabled to performed FMD calculations with the realistic Argonne V18 and CD-Bonn potentials up to mass A=60 [30]. Other FMD calculations of nuclei using realistic NN potentials followed [30, 31, 39, 40].

2.1   Model many-body state

In this work we study baryonic systems consisting of nucleons and a Λ hyperon. The baryons are treated as basic degrees of freedom with their internal structure described by Gaussian wave packets, in analogy with molecules for which 'molecular dynamics' was originally formulated [41]. Since we are dealing with systems of N

baryons, the wave function of the antisymmetrized many body state is described by a Slater determinant

$$\langle x_1, \ldots, x_N | \hat{A} | Q \rangle = \frac{1}{N!} \sum_{P_i} \text{sgn}(P_i) \langle x_1 | q_{P_i(1)} \rangle \ldots \langle x_N | q_{P_i(N)} \rangle$$

$$= \frac{1}{N!} \text{Det} \begin{vmatrix} \langle x_1 | q_1 \rangle & \cdots & \langle x_1 | q_N \rangle \\ \vdots & \ddots & \vdots \\ \langle x_N | q_1 \rangle & \cdots & \langle x_N | q_N \rangle \end{vmatrix}, \qquad (2.1)$$

where x_i stands for generalized coordinate with space, spin and isospin parts, P_i is the i-th permutation among single-particle states $|q_i\rangle$, and $\hat{A}$ is the antisymmetrization operator (see Appendix A). If not specified explicitly, we will omit the antisymmerization operator and will denote the antisymmetrized state by $|Q\rangle$ in the following.

In the FMD model, each single-particle state $|q_k\rangle$ is represented by a Gaussian wave packet

$$|q_k\rangle = |a_k, \boldsymbol{b_k}\rangle \otimes \left| \chi_k^\uparrow, \chi_k^\downarrow \right\rangle \otimes |\xi_k\rangle, \qquad (2.2)$$

where $\left| \chi_k^\uparrow, \chi_k^\downarrow \right\rangle$ ($|\xi_k\rangle$) denotes a spin (isospin) part. The shape of Gaussian wave packet in coordinate space is

$$\langle \boldsymbol{x} | a_k, \boldsymbol{b_k} \rangle = \exp\left(-\frac{(\boldsymbol{x} - \boldsymbol{b_k})^2}{2 a_k} \right), \qquad (2.3)$$

where a_k stands for a complex width and $\boldsymbol{b_k}$ denotes a complex vector. It is to be stressed that in FMD each baryon is in principle described by a different Gaussian width parameter. This represents a crucial difference from the otherwise very similar AMD model [42]. It allows FMD to describe exotic effects in nuclear systems like halo structure and clusterization [39, 40]. The spin part of a single-particle state $\left| \chi_k^\uparrow, \chi_k^\downarrow \right\rangle$ is treated as a most general complex spinor. This formulation ensures good rotational properties – it enables to rotate the state $|q_k\rangle$ by an arbitrary space angle Ω. In this work we study hypernuclear systems composed of the nuclear core and the Λ hyperon and we do not consider change of the third projection of isospin ξ_k of the k-th particle. Therefore, the isospin part $|\xi_k\rangle$ remains fixed during the whole calculation and is represented by vectors $|1/2\rangle$, $|-1/2\rangle$ for nucleons and $|0\rangle$ for Λ.

In principle one can define the single-particle state $|q_k\rangle$ as a superposition of an arbitrary number of Gaussians

$$|q_k\rangle = \sum_i C_{ki} |a_{ki}, \boldsymbol{b_{ki}}\rangle \otimes \left| \chi_{ki}^\uparrow, \chi_{ki}^\downarrow \right\rangle \otimes |\xi_k\rangle, \qquad (2.4)$$

which leads to more precise description of exotic nuclear systems [30]. However, since each additional Gaussian form in the sum increases the computational complexity considerably, we will use just one Gaussian wave packet following (2.2).

An important advantage of the FMD single-particle basis are its properties under translation, boost, parity and rotation operations. The action of the translation operator $\hat{U}(\boldsymbol{d})$ on the Gaussian wave packet can be expressed as

$$\hat{U}(\boldsymbol{d}) \left|a, \boldsymbol{b}\right\rangle \otimes \left|\chi^{\uparrow}, \chi^{\downarrow}\right\rangle \otimes \left|\xi\right\rangle = \left|a, \boldsymbol{b} + \boldsymbol{d}\right\rangle \otimes \left|\chi^{\uparrow}, \chi^{\downarrow}\right\rangle \otimes \left|\xi\right\rangle; \qquad (2.5)$$

and the boost operation with velocity $\boldsymbol{v}$ is

$$\hat{B}(\boldsymbol{v}) \left|a, \boldsymbol{b}\right\rangle \otimes \left|\chi^{\uparrow}, \chi^{\downarrow}\right\rangle \otimes \left|\xi\right\rangle = \left|a, \boldsymbol{b} + \mathrm{i}ma\boldsymbol{v}\right\rangle \otimes \left|\chi^{\uparrow}, \chi^{\downarrow}\right\rangle \otimes \left|\xi\right\rangle \cdot \exp\left\{\mathrm{i}m\boldsymbol{b} \cdot \boldsymbol{v} - \frac{a}{2}m^2\boldsymbol{v}^2\right\}, \tag{2.6}$$

where m denotes the mass of the particle represented by the Gaussian wave packet. The parity operation represented by $\hat{\Pi}$ can be written as

$$\hat{\Pi} \left|a, \boldsymbol{b}\right\rangle \otimes \left|\chi^{\uparrow}, \chi^{\downarrow}\right\rangle \otimes \left|\xi\right\rangle = \left|a, -\boldsymbol{b}\right\rangle \otimes \left|\chi^{\uparrow}, \chi^{\downarrow}\right\rangle \otimes \left|\xi\right\rangle. \tag{2.7}$$

In the case of rotation by a space angle Ω, represented by the operator $\hat{R}(\Omega)$, we must take into account that it acts both in the coordinate and spin space $\hat{R}(\Omega) = \hat{R}_{\mathrm{coor}}(\Omega) \otimes \hat{R}_{\mathrm{spin}}(\Omega)$ and thus

$$\begin{aligned}\hat{R}(\Omega) \left\{\left|a, \boldsymbol{b}\right\rangle \otimes \left|\chi^{\uparrow}, \chi^{\downarrow}\right\rangle \otimes \left|\xi\right\rangle\right\} &= \hat{R}_{\mathrm{coor}}(\Omega) \left|a, \boldsymbol{b}\right\rangle \otimes \hat{R}_{\mathrm{spin}}(\Omega) \left|\chi^{\uparrow}, \chi^{\downarrow}\right\rangle \otimes \left|\xi\right\rangle = \\ &= \left|a, \hat{R}_{\mathrm{coor}}(\Omega)\boldsymbol{b}\right\rangle \otimes \hat{R}_{\mathrm{spin}}(\Omega) \left|\chi^{\uparrow}, \chi^{\downarrow}\right\rangle \otimes \left|\xi\right\rangle.\end{aligned} \tag{2.8}$$

For the antisymmetrized many-body state the translation by a vector $\boldsymbol{d}$, boost by a velocity $\boldsymbol{v}$, rotation by an angle Ω, and the parity inversion are expressed by N-body unitary operators in the following form

$$\begin{aligned}\hat{U}(\boldsymbol{d}) &= \exp\left\{-\mathrm{i}\boldsymbol{d} \cdot \hat{\boldsymbol{P}}_{\mathrm{cm}}\right\} = \exp\left\{-\mathrm{i}\sum_i \boldsymbol{d} \cdot \hat{\boldsymbol{p}}_i\right\} = \hat{U}_1(\boldsymbol{d}) \otimes \ldots \otimes \hat{U}_N(\boldsymbol{d}), \\ \hat{B}(\boldsymbol{v}) &= \exp\left\{-\mathrm{i}M\boldsymbol{v} \cdot \hat{\boldsymbol{X}}_{\mathrm{cm}}\right\} = \exp\left\{-\mathrm{i}\sum_i m_i\boldsymbol{v} \cdot \hat{\boldsymbol{x}}_i\right\} = \hat{B}_1(\boldsymbol{v}) \otimes \ldots \otimes \hat{B}_N(\boldsymbol{v}), \\ \hat{R}(\Omega) &= \exp\left\{-\mathrm{i}\boldsymbol{\Omega} \cdot \hat{\boldsymbol{J}}\right\} = \exp\left\{-\mathrm{i}\sum_i \boldsymbol{\Omega} \cdot \hat{\boldsymbol{J}}_i\right\} = \hat{R}_1(\Omega) \otimes \ldots \otimes \hat{R}_N(\Omega), \\ \hat{\Pi} &= \hat{\Pi}_1 \otimes \ldots \otimes \hat{\Pi}_N.\end{aligned} \tag{2.9}$$

This means that the shift of the whole Slater determinant by a vector $\boldsymbol{d}$ is equivalent to the same shift of each single-particle state. The same holds also for the boost,

rotation and parity operations.

2.1.1 Intrinsic state

In the study of (hyper)nuclear structure we are interested in intrinsic properties of the many-body system and not in its center of mass (cms) position and momentum. It is desirable to fully separate the intrinsic and cms part of the many-body wave function

$$\langle \boldsymbol{x}_1, \ldots, \boldsymbol{x}_n | \, Q \rangle = \langle \boldsymbol{\zeta}_1, \ldots, \boldsymbol{\zeta}_n | \, Q_{\text{intr}} \rangle \, \langle \boldsymbol{X}_{\text{cm}} | \, Q_{\text{cm}} \rangle , \tag{2.10}$$

where $\langle \boldsymbol{X}_{\text{cm}} | \, Q_{\text{cm}} \rangle$ denotes the cms component and $\boldsymbol{X}_{\text{cm}}$ the cms coordinate. The $\langle \boldsymbol{\zeta}_1, \ldots, \boldsymbol{\zeta}_n | \, Q_{\text{intr}} \rangle$ stands for the intrinsic wave function with the following definition of intrinsic coordinates

$$\boldsymbol{\zeta}_i = \boldsymbol{x}_i - \boldsymbol{X}_{\text{cm}}, \qquad \boldsymbol{X}_{\text{cm}} = \frac{1}{M} \sum_i m_i \boldsymbol{x}_i, \tag{2.11}$$

where m_i is a mass of the i-th particle and M is the total mass of the system. The resulting intrinsic wave function would not depend on the choice of the reference frame and would be translationally invariant. However, the aforementioned factorization becomes quite difficult in the Slater determinant basis and can be applied only in a few special cases. One of them is a Slater determinant composed of Gaussian wave packets of equal width parameter a, as in AMD [43].

Unlike the AMD model we would like to use different width parameters, which enables better description of the cluster structure. This is the reason why we cannot follow the above separation of the cms motion and have to choose other approaches to suppress unfavorable cms effects.

Since we are not able to separate the cms part of the many-body wave function perfectly, it remains entangled with the intrinsic state and the FMD many-body state $|Q\rangle$ is not translationally invariant. We would like to have ensured, that the symmetry operations like parity and rotation (2.9) acting on the many-body state $|Q\rangle$ affect only its intrinsic part. But since

$$\langle \boldsymbol{x}_1, \ldots, \boldsymbol{x}_n | \, \hat{\Pi} \, | Q \rangle = \langle -\boldsymbol{x}_1, \ldots, -\boldsymbol{x}_n | \, Q \rangle ,$$
$$\boldsymbol{x}_i = \boldsymbol{\xi}_i + \boldsymbol{X}_{\text{cm}} \rightarrow -\boldsymbol{x}_i = -\boldsymbol{\xi}_i - \boldsymbol{X}_{\text{cm}},$$

$$\tag{2.12}$$

$$\langle \boldsymbol{x}_1, \ldots, \boldsymbol{x}_n | \, \hat{R}(\Omega) \, | Q \rangle = \left\langle \hat{R}^{-1}(\Omega)\boldsymbol{x}_1, \ldots, \hat{R}^{-1}(\Omega)\boldsymbol{x}_n \, \middle| \, Q \right\rangle ,$$
$$\boldsymbol{x}_i = \boldsymbol{\xi}_i + \boldsymbol{X}_{\text{cm}} \rightarrow \hat{R}^{-1}(\Omega)\boldsymbol{x}_i = -\hat{R}^{-1}(\Omega)\boldsymbol{\xi}_i + \hat{R}^{-1}(\Omega)\boldsymbol{X}_{\text{cm}},$$

this is fulfilled only when the center of mass position is equal to zero.

2.2 Expectation values

The FMD single-particle state basis is not orthogonal as can be clearly seen from the single-particle state overlap matrix n_{kl}

$$n_{kl} = \langle q_k | q_l \rangle = R_{kl} S_{kl} T_{kl},$$

$$R_{kl} = \langle a_k, \boldsymbol{b}_k | a_l, \boldsymbol{b}_l \rangle = \left(2\pi \frac{a_k^* a_l}{a_k^* + a_l} \right)^{3/2} \exp \left(-\frac{\boldsymbol{b}_k^* - \boldsymbol{b}_l}{2(a_k^* + a_l)} \right), \qquad (2.13)$$

$$S_{kl} = \left\langle \chi_k^\uparrow, \chi_k^\downarrow \middle| \chi_l^\uparrow, \chi_l^\downarrow \right\rangle = \chi_k^{\uparrow *} \chi_l^\uparrow + \chi_k^{\downarrow *} \chi_l^\downarrow,$$

$$T_{kl} = \langle \xi_k | \xi_l \rangle = \delta_{kl},$$

with space R_{kl}, spin S_{kl} and isospin T_{kl} overlap matrices.

Because of the nonorthogonality of the single-particle basis we express the expectation values of one and two-body operators $\hat{O}^{[1]}$ and $\hat{O}^{[2]}$ through inverse overlap matrices [33]

$$O^{[1]} = \frac{\langle Q | \hat{O}^{[1]} | Q \rangle}{\langle Q | Q \rangle} = \sum_{kl} \langle q_k | \hat{O}^{[1]} | q_l \rangle \, o_{lk},$$

$$(2.14)$$

$$O^{[2]} = \frac{\langle Q | \hat{O}^{[2]} | Q \rangle}{\langle Q | Q \rangle} = \sum_{klmn} \langle q_k, q_l | \hat{O}^{[2]} | q_m, q_n \rangle \, (o_{mk} o_{nl} - o_{nk} o_{ml}).$$

where o_{lk} stands for an element of the inverse overlap matrix $o = n^{-1}$. Hence we must evaluate the matrix o together with one or two-body matrix elements of an arbitrary operator $\hat{O}$. For derivation of the expectation value formula for one-body operators $\hat{O}^{[1]}$ see Appendix A.

2.3 Time-independent variational method

The Hamiltonian describing a hypernuclear system is defined in the form

$$\hat{H} = \hat{T}_{\text{intr}} + \hat{V}_{NN} + \hat{V}_{\Lambda N}, \qquad (2.15)$$

where $\hat{T}_{\text{intr}}$ denotes the intrinsic kinetic energy operator and $\hat{V}_{NN}$ ($\hat{V}_{\Lambda N}$) is the two-body NN (ΛN) potential.

To determine the form of the intrinsic kinetic energy operator $\hat{T}_{\text{intr}}$, i.e. kinetic energy of the internal motion, we express first the intrinsic momentum operator $\hat{\boldsymbol{\eta}}_i$ of the i-th baryon

$$\hat{\boldsymbol{\eta}}_i = \hat{\boldsymbol{p}}_i - m_i \hat{\boldsymbol{V}}_{\text{cm}} = \hat{\boldsymbol{p}}_i - \frac{m_i}{M} \hat{\boldsymbol{P}}_{\text{cm}}, \quad \hat{\boldsymbol{P}}_{\text{cm}} = \sum_i \hat{\boldsymbol{p}}_i, \tag{2.16}$$

where we take into account the definition of intrinsic coordinates (2.11). Here, $\hat{\boldsymbol{V}}_{\text{cm}}$ and $\hat{\boldsymbol{P}}_{\text{cm}}$ denotes the velocity and momentum operator of the center of mass, respectively, and $\hat{\boldsymbol{p}}_i$ is the momentum operator of the i-th baryon. The operator $\hat{T}_{\text{intr}}$ is then defined as

$$\hat{T}_{\text{intr}} = \sum_i \frac{\hat{\boldsymbol{\eta}}_i^2}{2m_i} = \sum_i \left[\hat{\boldsymbol{p}}_i - \frac{m_i}{M} \hat{\boldsymbol{P}}_{\text{cm}} \right]^2 = \sum_i \frac{\hat{\boldsymbol{p}}_i^2}{2m_i} - \frac{1}{2M} \sum_{ij} \hat{\boldsymbol{p}}_i \hat{\boldsymbol{p}}_j =$$
$$= \hat{T} - \sum_i \frac{\hat{\boldsymbol{p}}_i^2}{2M} - \frac{1}{M} \sum_{i<j} \hat{\boldsymbol{p}}_i \hat{\boldsymbol{p}}_j = \hat{T} - \hat{T}_{\text{cm}}^{[1]} - \hat{T}_{\text{cm}}^{[2]} = \hat{T} - \hat{T}_{\text{cm}}. \tag{2.17}$$

The Hamiltonian can be then expressed in the form

$$\hat{H} = \hat{T} - \hat{T}_{\text{cm}} + \hat{V}_{NN} + \hat{V}_{\Lambda N}. \tag{2.18}$$

The ground state of a hypernuclear system is determined within the time-independend variational method. The binding energy E_{B} of the many-body system is defined as a minimum

$$E_{\text{B}} = \min_{q_1,\ldots,q_N} \frac{\langle Q | \hat{H} | Q \rangle}{\langle Q | Q \rangle},$$

under following conditions

$$< \hat{\boldsymbol{X}}_{\text{cm}} >^2 = 0, \quad < \hat{\boldsymbol{P}}_{\text{cm}} >^2 = 0, \quad Re(a_k) > 0, \tag{2.19}$$

where the expectation value of the intrinsic Hamiltonian $\hat{H}$ is minimized with respect to single-particle state parameters $q_1, \ldots, q_N$. In this sense the symbol q_i means a set of twelve independent real parameters of th i-th single-particle state $|q_i\rangle$.

To solve this problem numerically we implemented the Sequential Quadratic Programming (SQP) method for nonlinear optimization with equality or inequality constraints [44]. The equality bounds $< \hat{\boldsymbol{X}}_{\text{cm}} >^2 = 0$ and $< \hat{\boldsymbol{P}}_{\text{cm}} >^2 = 0$ ensure that we can later safely use symmetry operators (2.9) and project out parity and total angular momentum eigenstates of the hypernuclear system. The condition $Re(a_k) > 0$ must be met in order to have well-define Gaussian wave packets. The case $Re(a_k) = 0$ describes situation when a Gaussian wave packet turns into a delta

function with localized position and infinite momentum. Gaussian wave packets with $Re(a_k) < 0$ are not integrable functions.

To conclude, we obtain as a result the value of the binding energy E_B and sets of the parameters of single-particle states $q_1, \ldots, q_N$ which define the many-body state $|Q\rangle$ with the lowest energy with respect to the constraints.

2.4 Parity and total angular momentum eigenstates

So far we discussed the antisymmetrized many-body state $|Q\rangle$ as a result of variational principle. However, this state need not be an eigenstate of the total angular momentum and parity and hence we would not describe hypernuclear ground and excited states properly. In fact, the result of the minimization process $|Q\rangle$ is in general a linear combination of individual eigenstates of the total angular momentum and parity $|Q; J^\pi \kappa\rangle$

$$|Q\rangle = \sum_\kappa |Q; J^\pi \kappa\rangle \, C^{J^\pi \kappa}. \tag{2.20}$$

Since we want to calculate observables for the hypernuclear states with well-defined quantum numbers, we introduce two kinds of projections. The first one is performed by the parity projection operator $\hat{P}^\pi$ and the second one by the total angular momentum projection operator $\hat{P}^J_{MK}$, followed by a K-mixing procedure.

2.4.1 Parity eigenstates

In the definition of a parity eigenstate we make us of the parity projection operator

$$\hat{P}^\pi = \frac{1}{2}\left(1 + \pi\hat{\Pi}\right), \tag{2.21}$$

where π stands for the parity eigenvalue. The eigenstate is then defined as

$$|Q; \pi\rangle = \frac{1}{2}\left(|Q\rangle + \pi\hat{\Pi}|Q\rangle\right) \tag{2.22}$$

and the expectation value of an arbitrary operator $\hat{O}$ has the form

$$
\begin{aligned}
O &= \frac{\langle Q; \pi| \hat{O} |Q; \pi\rangle}{\langle Q; \pi| Q; \pi\rangle} = \\
&= \frac{\langle Q| \hat{O} |Q\rangle + \pi \langle Q| \hat{O}\hat{\Pi} |Q\rangle - \frac{1}{2}\left(\langle Q| \left[\hat{\Pi}, \hat{Q}\right] \hat{\Pi} |Q\rangle + \pi \langle Q| \left[\hat{\Pi}, \hat{Q}\right] |Q\rangle\right)}{\langle Q| Q\rangle + \pi \langle Q| \hat{\Pi} |Q\rangle}.
\end{aligned} \tag{2.23}
$$

2.4.2 Total angular momentum eigenstates

The total angular momentum projection is performed using the Generator Coordinate Method (GCM). We take into account properties of the rotational group SO(3) generated by the total angular momentum operator $\hat{\boldsymbol{J}}$ and we use the corresponding projection operator [45]

$$\hat{P}^J_{MK} = \frac{2J+1}{8\pi^2} \int d\Omega D^J_{MK}{}^*(\Omega)\hat{R}(\Omega). \tag{2.24}$$

Here, $\hat{R}(\Omega)$ denotes the rotation operator (2.8), J is the total angular momentum eigenvalue, M and K its third projection in the laboratory and intrinsic reference frame, respectively , and $D^J_{MK}{}^*(\Omega)$ stands for the Wigner D-function

$$D^J_{MM'}(\Omega) = \langle JM| \hat{R}(\Omega) |JM'\rangle. \tag{2.25}$$

The projection operator fulfills the following relation [45]

$$\hat{P}^{J\dagger}_{M'K'}\hat{P}^J_{MK} = \delta_{M'M}\hat{P}^J_{K'K}. \tag{2.26}$$

Parity and total angular momentum projected states are then expressed as

$$|Q; J^\pi MK\rangle = \hat{P}^J_{MK} |Q; \pi\rangle = \frac{2J+1}{8\pi^2} \int d\Omega D^J_{MK}{}^*(\Omega)\hat{R}(\Omega) |Q; \pi\rangle. \tag{2.27}$$

Since the projected states (2.27) are not linearly independent, we define orthogonal eigenstates as

$$|Q; J^\pi M\kappa\rangle = \sum_K |Q; J^\pi MK\rangle C^{J^\pi\kappa}_K, \tag{2.28}$$

where the complex coefficients $C^{J^\pi\kappa}_K$ are obtained by diagonalizing the Hamiltonian $\hat{H}$ (2.18) in a subspace spanned by the projected states $|Q; J^\pi MK\rangle$. This leads to a generalized eigenvalue problem

$$\sum_{K'} H^{J^\pi}_{KK'}C^{J^\pi\kappa}_{K'} = E^{J^\pi\kappa} \sum_{K''} N^{J^\pi}_{KK''}C^{J^\pi\kappa}_{K''}, \tag{2.29}$$

where $H^{J^\pi}_{KK'}$ and $N^{J^\pi}_{KK''}$ are defined as

$$\begin{aligned}
H^{J^\pi}_{K,K'} &= \langle Q; J^\pi MK| \hat{H} |Q; J^\pi M'K'\rangle = \langle Q;\pi| \hat{H}\hat{P}^J_{KK'} |Q;\pi\rangle, \\
N^{J^\pi}_{K,K''} &= \langle Q; J^\pi MK| Q; J^\pi M''K''\rangle = \langle Q;\pi| \hat{P}^J_{KK''} |Q;\pi\rangle.
\end{aligned} \tag{2.30}$$

It is exacting to calculate the matrices $H^{J^\pi}_{KK'}$ and $N^{J^\pi}_{KK''}$ due to the integration

over the space angle Ω in the projection operator (2.24). After expressing the integration in terms of Euler angles α, β and γ, the Hamiltonian and overlap matrix acquire the form

$$
\begin{aligned}
H_{KK'}^{J^\pi} &= \frac{2J+1}{8\pi} \int d\alpha \, d\beta \, d\gamma D_{KK'}^{J}{}^*(\alpha, \beta, \gamma) \langle Q; \pi| \hat{H}\hat{R}(\alpha, \beta, \gamma) |Q; \pi \rangle, \\
N_{KK''}^{J^\pi} &= \frac{2J+1}{8\pi} \int d\alpha \, d\beta \, d\gamma D_{KK''}^{J}{}^*(\alpha, \beta, \gamma) \langle Q; \pi| \hat{R}(\alpha, \beta, \gamma) |Q; \pi \rangle.
\end{aligned}
\tag{2.31}
$$

The Wigner D-functions can be further expressed as

$$
D_{KK'}^{J}(\alpha, \beta, \gamma) = e^{-\mathrm{i}K\alpha} d_{KK'}^{J}(\beta) e^{-\mathrm{i}K'\gamma},
\tag{2.32}
$$

where $d_{KK'}^{J}(\beta)$ denotes the small Wigner d-function. The integration is performed numerically on the grid. We take 10 grid points for the integrations over angles α and γ and 20 Gauss-Legendre grid points over angle β, as suggested in Ref. [46].

The expectation value of an arbitrary scalar operator is calculated for the parity and total angular momentum eigenstates as [45]

$$
O^{J^\pi \kappa} = \frac{\langle Q; J^\pi M\kappa| \hat{O} |Q; J^\pi M\kappa \rangle}{\langle Q; J^\pi M\kappa| Q; J^\pi M\kappa \rangle} = \frac{\sum_{KK'} C_K^{J^\pi \kappa} C_{K'}^{J^\pi \kappa} O_{KK'}^{J^\pi}}{\sum_{KK''} C_K^{J^\pi \kappa} C_{K''}^{J^\pi \kappa} N_{KK''}^{J^\pi}},
$$

where

$$
O_{KK'}^{J^\pi} = \frac{2J+1}{8\pi} \int d\alpha \, d\beta \, d\gamma D_{KK'}^{J}{}^*(\alpha, \beta, \gamma) \langle Q; \pi| \hat{O}\hat{R}(\alpha, \beta, \gamma) |Q; \pi \rangle.
\tag{2.33}
$$

2.5 Variation after projection

As we discussed in section 2.4, the result of the variational method, the many-body state $|Q\rangle$, is a linear combination of the individual eigenstates $|Q; J^\pi \kappa\rangle$. Quite frequently, only a limited number of eigenstates is relevant in the linear combination (2.20) while the other states are realized at a level of numerical noise. The projection of these 'suppressed' eigenstates is not meaningful and thus it is reasonable to exclude them. One possibility is to perform variation of a projected state (VAP). In this work, we perform variation after parity projection (VAP$^\pi$) due to manageable computational requirements. This procedure increases the abundance of odd or even parity eigenstates in the resulting state. It is also possible to apply variation of the angular momentum projected state (VAP^J) or the angular momentum plus parity projected state (VAP$^{J^\pi}$). These three options were compared in calculations of ^{12}C [46]. Another possibility is to put additional constraints during variation (2.19). The expectation value of the Hamiltonian is then minimized with respect to fixed values of experimentally observed quantities.

Chapter 3

Interactions

Due to the variational nature of the FMD model, it is necessary to express each interaction matrix element analytically as a function of the single-particle states variational parameters. Therefore, we are limited to potentials that are expressed in operator form. The most general operator structure of the V_{NN} potential allowed by symmetries [47] is

$$
\begin{aligned}
\hat{V}_{NN} =& V_c(\hat{\boldsymbol{r}}^{\boldsymbol{2}}, \hat{\boldsymbol{p}}^{\boldsymbol{2}}, \hat{\boldsymbol{L}}^{\boldsymbol{2}}) + V^\sigma(\hat{\boldsymbol{r}}^{\boldsymbol{2}}, \hat{\boldsymbol{p}}^{\boldsymbol{2}}, \hat{\boldsymbol{L}}^{\boldsymbol{2}})\hat{\boldsymbol{\sigma}}_{\boldsymbol{1}}.\hat{\boldsymbol{\sigma}}_{\boldsymbol{2}} + V_T(\hat{\boldsymbol{r}}^{\boldsymbol{2}}, \hat{\boldsymbol{p}}^{\boldsymbol{2}}, \hat{\boldsymbol{L}}^{\boldsymbol{2}})\hat{S}_{12}(\hat{\boldsymbol{r}})+ \\
&+ V_{LS}(\hat{\boldsymbol{r}}^{\boldsymbol{2}}, \hat{\boldsymbol{p}}^{\boldsymbol{2}}, \hat{\boldsymbol{L}}^{\boldsymbol{2}})\hat{\boldsymbol{L}}.\hat{\boldsymbol{S}} + V_{(LS)^2}(\hat{\boldsymbol{r}}^{\boldsymbol{2}}, \hat{\boldsymbol{p}}^{\boldsymbol{2}}, \hat{\boldsymbol{L}}^{\boldsymbol{2}})(\hat{\boldsymbol{L}}.\hat{\boldsymbol{S}})^2+ \\
&+ V_{Tp}(\hat{\boldsymbol{r}}^{\boldsymbol{2}}, \hat{\boldsymbol{p}}^{\boldsymbol{2}}, \hat{\boldsymbol{L}}^{\boldsymbol{2}})S_{12}(\hat{\boldsymbol{p}}) + V_c^\tau(\hat{\boldsymbol{r}}^{\boldsymbol{2}}, \hat{\boldsymbol{p}}^{\boldsymbol{2}}, \hat{\boldsymbol{L}}^{\boldsymbol{2}})(\hat{\boldsymbol{\tau}}_{\boldsymbol{1}}.\hat{\boldsymbol{\tau}}_{\boldsymbol{2}})+ \\
&+ V^{\sigma\tau}(\hat{\boldsymbol{r}}^{\boldsymbol{2}}, \hat{\boldsymbol{p}}^{\boldsymbol{2}}, \hat{\boldsymbol{L}}^{\boldsymbol{2}})(\hat{\boldsymbol{\sigma}}_{\boldsymbol{1}}.\hat{\boldsymbol{\sigma}}_{\boldsymbol{2}})(\hat{\boldsymbol{\tau}}_{\boldsymbol{1}}.\hat{\boldsymbol{\tau}}_{\boldsymbol{2}}) + V_T^\tau(\hat{\boldsymbol{r}}^{\boldsymbol{2}}, \hat{\boldsymbol{p}}^{\boldsymbol{2}}, \hat{\boldsymbol{L}}^{\boldsymbol{2}})S_{12}(\hat{\boldsymbol{r}})(\hat{\boldsymbol{\tau}}_{\boldsymbol{1}}.\hat{\boldsymbol{\tau}}_{\boldsymbol{2}})+ \\
&+ V_{LS}^\tau(\hat{\boldsymbol{r}}^{\boldsymbol{2}}, \hat{\boldsymbol{p}}^{\boldsymbol{2}}, \hat{\boldsymbol{L}}^{\boldsymbol{2}})(\hat{\boldsymbol{L}}.\hat{\boldsymbol{S}})(\hat{\boldsymbol{\tau}}_{\boldsymbol{1}}.\hat{\boldsymbol{\tau}}_{\boldsymbol{2}}) + V_{(LS)^2}^\tau(\hat{\boldsymbol{r}}^{\boldsymbol{2}}, \hat{\boldsymbol{p}}^{\boldsymbol{2}}, \hat{\boldsymbol{L}}^{\boldsymbol{2}})(\hat{\boldsymbol{L}}.\hat{\boldsymbol{S}})^2(\hat{\boldsymbol{\tau}}_{\boldsymbol{1}}.\hat{\boldsymbol{\tau}}_{\boldsymbol{2}})+ \\
&+ V_{Tp}^\tau(\hat{\boldsymbol{r}}^{\boldsymbol{2}}, \hat{\boldsymbol{p}}^{\boldsymbol{2}}, \hat{\boldsymbol{L}}^{\boldsymbol{2}})\hat{S}_{12}(\hat{\boldsymbol{p}})(\hat{\boldsymbol{\tau}}_{\boldsymbol{1}}.\hat{\boldsymbol{\tau}}_{\boldsymbol{2}}),
\end{aligned}
\tag{3.1}
$$

where each of the operator terms can be accompanied by an arbitrary combination of the squares of the relative distance, momentum, and orbital angular momentum operators denoted as $\hat{\boldsymbol{r}}^2$, $\hat{\boldsymbol{p}}^2$, and $\hat{\boldsymbol{L}}^2$, respectively. Here, $\hat{\boldsymbol{S}}$ is the total spin operator of the two-nucleon system $\hat{\boldsymbol{S}} = \hat{\boldsymbol{s}}_{\boldsymbol{1}} + \hat{\boldsymbol{s}}_{\boldsymbol{2}}$ and $\hat{\boldsymbol{\sigma}} = (\sigma^{(1)}, \sigma^{(2)}, \sigma^{(3)})$ ($\hat{\boldsymbol{\tau}} = (\sigma^{(1)}, \sigma^{(2)}, \sigma^{(3)})$) denotes the vector of the Pauli matrices $\sigma^{(i)}$ acting in spin (isospin) space. The tensor operators $\hat{S}_{12}(\hat{\boldsymbol{p}})$ and $\hat{S}_{12}(\hat{\boldsymbol{r}})$ can be expressed as $\hat{S}_{12}(\hat{\boldsymbol{p}}) = 2[3(\hat{\boldsymbol{S}}.\hat{\boldsymbol{p}})^2 - \hat{\boldsymbol{S}}^2]$ and $\hat{S}_{12}(\hat{\boldsymbol{r}}) = 2[3(\hat{\boldsymbol{S}}.\hat{\boldsymbol{r}})^2 - \hat{\boldsymbol{S}}^2]$.

Among the NN interactions that are given in operator form different versions of the Argonne V_{NN} potentials are widely used. The Argonne V14 potential [48] does not consider the dependence on $\hat{\boldsymbol{p}}^2$ and $\hat{S}_{12}(\hat{\boldsymbol{p}})$ and consists of 14 operator terms. The Argonne V18 potential [49] has the same operator structure as V14 but it contains in addition four operator terms describing the charge symmetry breaking (CSB) of nuclear forces.

In contrast to the NN interaction, the form of the hyperon-nucleon V_{YN} potential is not so strictly constrained by limited YN scattering data and hypernuclear data. Therefore, it does not make much sense to consider its full operator structure and a simplified V_{YN} operator form is often used instead [2]

$$\hat{V}_{YN} = V_c(\hat{\boldsymbol{r}}^2) + V^\sigma(\hat{\boldsymbol{r}}^2)\hat{\boldsymbol{\sigma}}_1.\hat{\boldsymbol{\sigma}}_2 + V_T(\hat{\boldsymbol{r}}^2)S_{12}(\hat{\boldsymbol{r}}) + V_{LS+}(\hat{\boldsymbol{r}}^2)\hat{\boldsymbol{L}}.\hat{\boldsymbol{S}}^+ + V_{LS-}(\hat{\boldsymbol{r}}^2)\hat{\boldsymbol{L}}.\hat{\boldsymbol{S}}^-,$$
(3.2)

where $\hat{\boldsymbol{L}}.\hat{\boldsymbol{S}}^+$ and $\hat{\boldsymbol{L}}.\hat{\boldsymbol{S}}^-$ stand for a symmetric $\hat{\boldsymbol{L}}.(\hat{\boldsymbol{s}}_Y+\hat{\boldsymbol{s}}_N)$ and antisymmetric $\hat{\boldsymbol{L}}.(\hat{\boldsymbol{s}}_Y-\hat{\boldsymbol{s}}_N)$ spin-orbit interaction. In this work, we consider only $V_{\Lambda N}$ potentials.

The three-body forces play an important role in nuclear as well as Λ hypernuclear structure calculations. It was found that they successfully refine theoretical predictions of the binding energies [50, 51, 52]. In the case of realistic in-medium ΛN interactions the conversion between Λ and Σ hyperon known as the $\Lambda N - \Sigma N$ mixing has to be considered. Since the ΛN scattering data are rather scarce, few-body calculations of light Λ hypernuclei play an important role in testing of various $V_{\Lambda N}$ potential models. Several types of $V_{\Lambda N}$ potential models which take into account $\Lambda N - \Sigma N$ mixing have been suggested - the Nijmegen SC89 [53], Nijmegen SC97a-f [54], Nijmegen ESC04 [55, 56], and Jülich '04 [57]. However, their predictions for hypernuclei differ from each other. Nogga et al. concluded that out of the SC89, SC97a-f, and Jülich '04 potentials only SC89, SC97e, SC97f, and Jülich '04 give the bound hypertriton $^3_\Lambda$H [16, 17]. They also showed that the theoretical predictions of the Λ separation energy and the level ordering of the $^4_\Lambda$He 0^+ ground and 1^+ excited state vary among different $V_{\Lambda N}$ potential models [16]. Akaishi et al. performed consistent study of the $\Lambda N - \Sigma N$ coupling in s-shell Λ hypernuclei [58, 59]. They found, that the binding problem of the $^3_\Lambda$H, $^4_\Lambda$H, $^4_\Lambda$He, and $^5_\Lambda$He hypernuclei can be solved by the attractive coherent and repulsive incoherent parts of the $\Lambda N - \Sigma N$ coupling. Moreover, the main contribution of the attractive part was found equivalent to the three-body ΛNN force.

Nowadays, the NN potentials based on the chiral pertrubation theory (ChPT) [60, 61, 62] play a dominant role in structure calculations of light hypernuclei. Haidenbauer et al. extended the formalism to the strangeness sector and derived YN interaction in the leading order (LO) [63] and next-to-leading order (NLO) [64] of the ChPT. The LO YN interaction together with N^{3}LO NN interaction [65] were successfully used in the first *ab initio* No Core Shell Model (NCSM) calculations of the s-shell [22] and p-shell Λ hypernuclei up to $^{13}_\Lambda$C [23].

The realistic as well as effective NN and ΛN potentials are strongly repulsive at short distances between two particles. This behavior reflects the internal structure of baryons and prevents them to get too close to each other, to a distance of less

than about 0.5 fm (approximate size of N and Λ). Various many-body models (including FMD) use a Slater determinant as an approximation of an antisymmetrized many-body wave function. However, the structure of the Slater determinant is not able to reflect the hole in the two-body density caused by the strong short-ranged correlations due to the repulsive core of interaction. Moreover, the non-vanishing two-body density at relative distance close to zero gives unrealistically high momenta and hence high kinetic energy which makes it impossible to describe bound systems [30]. There are several transformation methods which fix this incompatibility and soften or remove the repulsive core. In this work, we applied the G-matrix transformed ΛN interaction [21] and the Unitary Correlation Operator Method (UCOM) transformed V_{NN} potentials [35].

3.1   Potentials used in this work

We use several types of relatively simple V_{NN} and $V_{\Lambda N}$ potentials which were available during the recent development of our FMD code. The three-body NNN and YNN forces were not considered in our calculations at this point and the $\Lambda N - \Sigma N$ mixing is not explicitly taken into account, however, its contribution is included in the $V_{\Lambda N}$ potentials through the G-matrix. The operator structure of the applied V_{NN} and $V_{\Lambda N}$ potentials, their parameters, as well as the manner in which the Coulomb interaction V_C is taken into account are given in Appendix D.

3.1.1   V$_{\text{NN}}$ potentials

In our calculations, we adopted following two-body V_{NN} potentials - the Volkov V2 (V2M0.0 and V2M0.6) [66] , Afnan-Tang S3M (ATS3M) [36], and Malfliet-Tjon V (MTV) [37]. The last two interactions have too strong repulsive core, therefore we use their UCOM transformed versions [35].

The Volkov V2 potential was introduced as an effective soft-core NN interaction which may be used in many-body techniques based on Slater determinants. It was constructed with respect to three criteria: "the s-wave scattering length should not be too far from the singlet and triplet scattering lengths, the effective range should not be too different from the triplet and singlet effective ranges, and the binding energy and size of ^{4}He should be given with the appropriate shell-model Slater determinant" [66].

The Afnan-Tang S3 V_{NN} potential [67] was determined by fitting the low-energy nucleon-nucleon scattering data (up to 100 MeV) and experimental binding energies and radii of ^{3}H and ^{4}He. The modified version S3M of this potential has in addition

a phenomenological repulsive term in the odd channel which allows to describe heavier systems. Since the modified version includes the strongly repulsive core, we implement UCOM transformed version in our calculations.

The Malfliet-Tjon V was designed to reproduce the binding energy of ^{3}H and the nucleon-nucleon phase shifts up to 300 MeV. Due to its strongly repulsive core we use again its UCOM softened version.

3.1.2 $V_{\Lambda N}$ potentials

Hypernuclear calculations presented in this work are performed using G-matrix transformed YNG ΛN interactions [21]. We implemented five different two-body $V_{\Lambda N}$ potentials: YNG-JA (JA), YNG-JB (JB), YNG-ND (ND), YNG-NF (NF), and YNG-NS (NS). The important feature of the YNG interactions is their Fermi momentum dependence which describes the nuclear medium surrounding the Λ hyperon. Therefore, it is necessary to use a different Fermi momentum parameter k_{F} for each hypernuclear system. The k_{F} dependence is rather steep, hence, the determination of the suitable value of k_{F} may become a delicate problem. In most cases, the Fermi momentum value is selected to reproduce the experimental value of the Λ separation energy [18].

The YNG-JA and YNG-JB ΛN potentials are based on the G-matrix transformed Jülich model-A and model-B [68], respectively. The model-A considers only single-particle exchange diagrams whereas the model-B contains also higher order processes. The YNG-ND, NF, and NS ΛN interactions are determined to simulate the G-matrix transformed one-boson-exchange Nijmegen potential model-D, F and soft core model-S [53], respectively.

Chapter 4

Results

In this chapter, we present the first results of the calculations of light hypernuclei using our recently developed FMD code.

The physical quantities used as an input in this work are given in Table 4.1. We applied identical values of the proton and neutron rest masses [69] as in the previous FMD nuclear structure studies [34, 35], which allowed us to compare directly the nuclear part of our FMD program with the earlier calculations. The rest mass of the Λ hyperon m_Λ and the value of the neutron charge mean-square radius $\langle r_n^2 \rangle$ were taken from [1]. We used the experimental value of the proton charge rms radius $\sqrt{\langle r_p^2 \rangle}$ extracted from the ep scattering data (2010 CODATA) [70].

Table 4.1: The experimental values of the physical quantities used in our calculations: proton (m_p), neutron (m_n), and Λ (m_Λ) rest mass, neutron charge mean-square radius $\langle r_n^2 \rangle$ and proton rms radius $\sqrt{\langle r_p^2 \rangle}$.

Physical input		
m_p	938.27231	MeV
m_n	939.56563	MeV
m_Λ	1115.683	MeV
$\langle r_n^2 \rangle$	-0.1161	fm^2
$\sqrt{\langle r_p^2 \rangle}$	0.8775	fm

4.1 Numerical solution of the variational method (convergence, VAP$^\pi$)

First, we study the convergence of the FMD model within two different minimization algorithms - the SQP [44] and L-BFGS-B [71]. In SQP, the expectation value of

the binding energy E_{B} is minimized under additional constraints - with respect to equality bounds $< \hat{\boldsymbol{X}}_{\mathrm{cm}} >^2 = 0$, $< \hat{\boldsymbol{P}}_{\mathrm{cm}} >^2 = 0$, and box constraints $Re(a_{\mathrm{k}}) > 0$. In L-BFGS-B, E_{B} is minimized only with respect to box constraints $Re(a_{\mathrm{k}}) > 0$. In Section 2.1.1, we mentioned that the action of a parity operator on a many-body state $|Q\rangle$ affects only the intrinsic coordinates if $< \hat{\boldsymbol{X}}_{\mathrm{cm}} > = \boldsymbol{0}$. Since L-BFGS-B does not consider the equality bounds, we do not apply this algorithm to minimization involving parity operators. Hence, we use L-BFGS-B only in the case of nuclear calculations performed by variation of the basic FMD state (V) to test the more advanced SQP algorithm.

In Figure 4.1, we compare the convergence of the ^{3}He FMD calculations using both L-BFGS-B and SQP minimization algorithms. The variation is performed for the basic FMD state (V) and the V_{NN} ATS3M potential. In the case of L-BFGS-B algorithm (left panel), we plot the value of the binding energy E_{B} of ^{3}He in each iteration step. We observe that the algorithm converges to $E_{\mathrm{B}} = -5.403$ MeV.
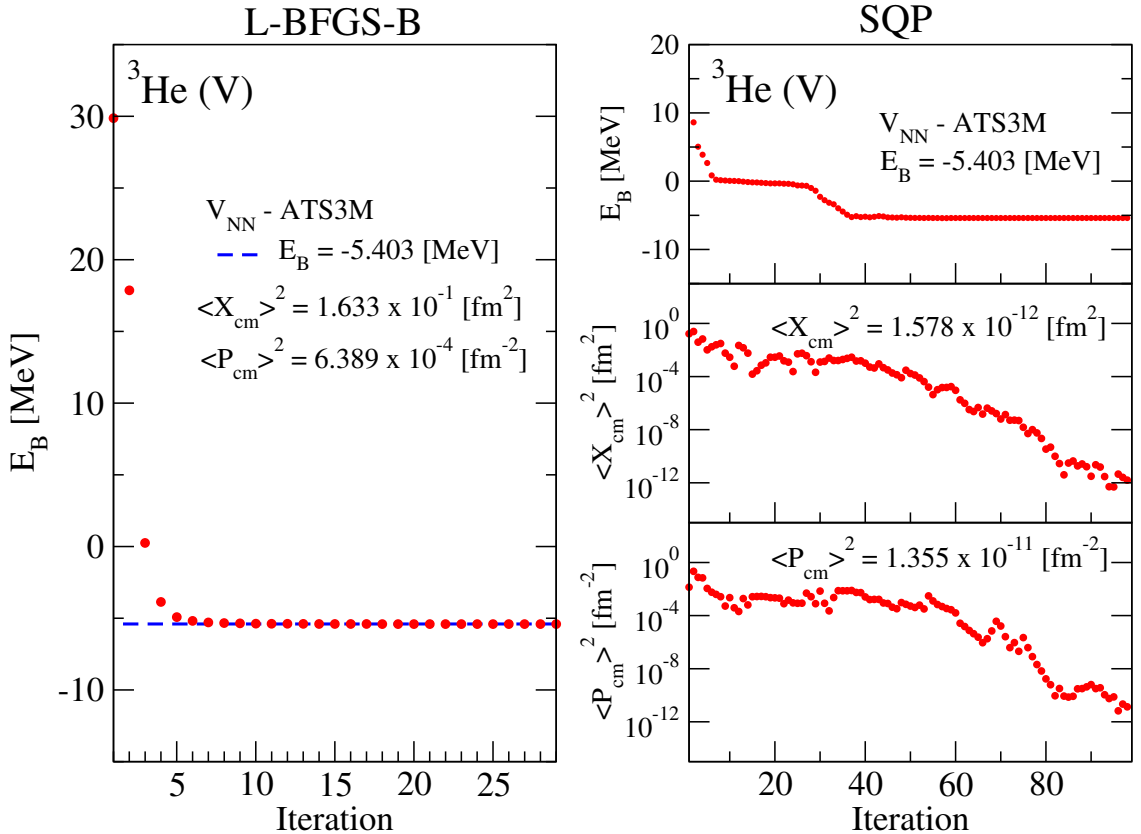
Figure 4.1: The convergence of the ^{3}He FMD calculations using the L-BFGS-B (left panel) and SQP (right panel) algorithms. The binding energy E_{B} is shown in each iteration step. In case of SQP algorithm, the values of $< \hat{\boldsymbol{X}}_{\mathrm{cm}} >^2$ and $< \hat{\boldsymbol{P}}_{\mathrm{cm}} >^2$ in each iteration are presented as well. Both calculations are performed by variation of the basic FMD trial state (V) using the ATS3M V_{NN} potential.

However, the resulting state $|Q\rangle$ does not have the position and momentum of the center of mass square equal to zero. The right panel of Fig. 4.1 shows the convergence of the ^{3}He calculation using the SQP algorithm with equality bounds $< \hat{X}_{cm} >^2= 0$ and $< \hat{P}_{cm} >^2= 0$. We plot the values of E_B, $< \hat{X}_{cm} >^2$, and $< \hat{P}_{cm} >^2$ in each iteration step. Due to the non-trivial minimization of the binding energy E_B with respect to the equality bounds the SQP algorithm converges much slower. Both algorithms converge to the same value of the ^{3}He binding energy, however the resulting state $|Q\rangle$ in SQP in addition satisfies the bounds $< \hat{X}_{cm} >^2= 0$ and $< \hat{P}_{cm} >^2= 0$ within desired precision. We successfully tested the consistency between aforementioned algorithms on the ^{3}H, ^{4}He, ^{6}Li, and ^{7}Li nuclei using various V_{NN} potentials.

The minimization of the binding energy E_B with respect to $< \hat{X}_{cm} >^2= 0$ allows to perform the variation of the parity projected trial FMD state VAP$^\pi$ and to apply the YNG $V_{\Lambda N}$ potentials in their spin-parity channels (see Appendix C). In Fig-
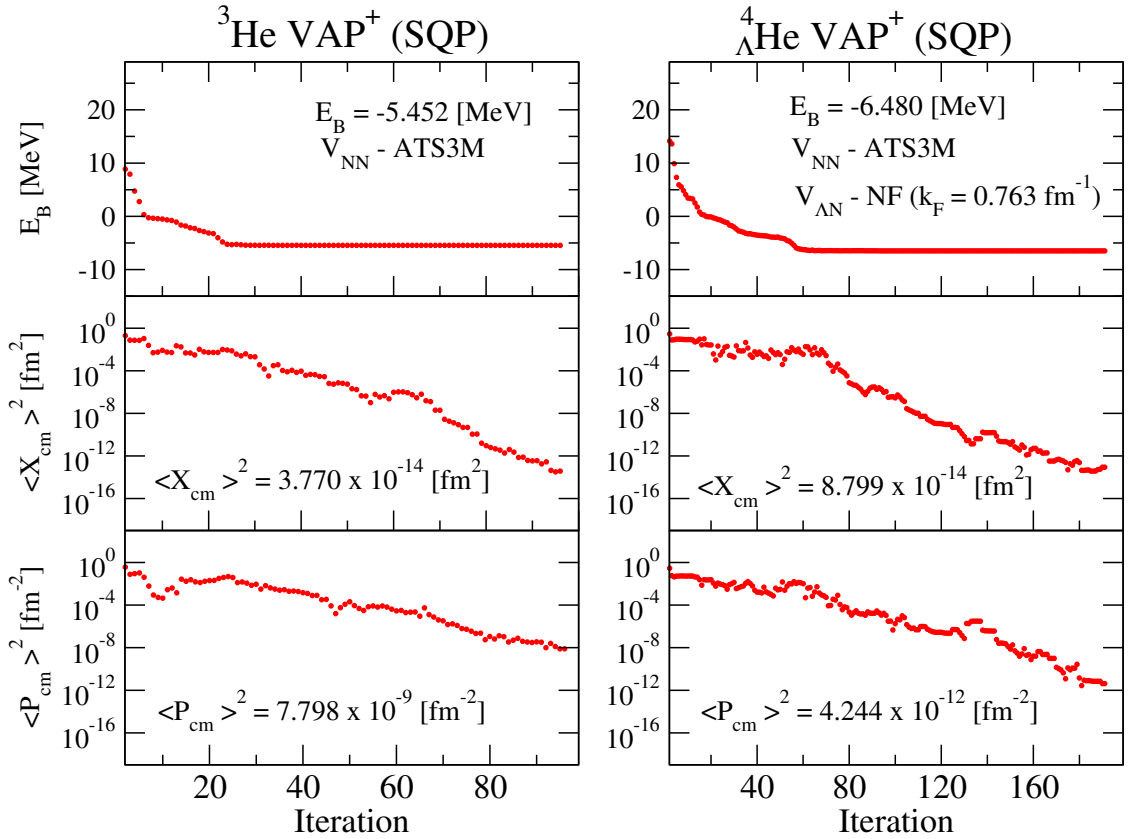
Figure 4.2: The convergence of the ^{3}He (left panel) and $^4_\Lambda$He (right panel) FMD calculations using the SQP algorithm. The binding energy E_B as well as the values of $< \hat{X}_{cm} >^2$ and $< \hat{P}_{cm} >^2$ in each iteration step are presented. Both calculations are performed by variation of the even parity projected FMD trial state (VAP$^+$) using the ATS3M V_{NN} potential. In the case of $^4_\Lambda$He, the $V_{\Lambda N}$ part is described by the NF potential.

ure 4.2, we show the minimization of the ^{3}He and $^4_\Lambda$He binding energies with respect to $< \hat{\boldsymbol{X}}_{\mathrm{cm}} >^2 = 0$ and $< \hat{\boldsymbol{P}}_{\mathrm{cm}} >^2 = 0$ using the SQP algorithm. In both calculations, we used the ATS3M V_{NN} potential and we performed the variation of the even parity projected FMD state (VAP$^+$). In the case of $^4_\Lambda$He, we described the ΛN interaction using the YNG-NF potential with $k_{\mathrm{F}} = 0.763\ \mathrm{fm}^{-1}$. We observe, that the VAP$^+$ minimization of the ^{3}He binding energy converges to the value $E_{\mathrm{B}} = -5.452$ MeV which lies slightly below the minimum $E_{\mathrm{B}} = -5.403$ MeV calculated with the variation of the basic FMD state (V) in Figure 4.1. The reason of this improvement is that the VAP$^+$ trial state is the even eigenstate of the parity operator, therefore, it provides better description of the $1/2^+$ ground state of ^{3}He. From Figure 4.2, we can directly assess the Λ separation energy as $B_\Lambda \approx E_{\mathrm{B}}(^3\mathrm{He}; +) - E_{\mathrm{B}}(^4_\Lambda\mathrm{He}; +) = 1.028$ MeV, neglecting the total angular momentum projection.

The $^4_\Lambda$He hypernucleus has the 0^+ ground state and 1^+ excited state. The Λ separation energies in the parity and total angular momentum projected 0^+ and 1^+ states of $^4_\Lambda$He, calculated using the ATS3M V_{NN} and YNG-NF $V_{\Lambda N}$ (NF) potentials are shown in Figure 4.3. The results of the variation of a basic FMD trial state (V) are compared with the results for the even parity projected trial FMD state (VAP$^+$). Clearly, the VAP$^+$ leads to larger Λ separation energies of the both 0^+
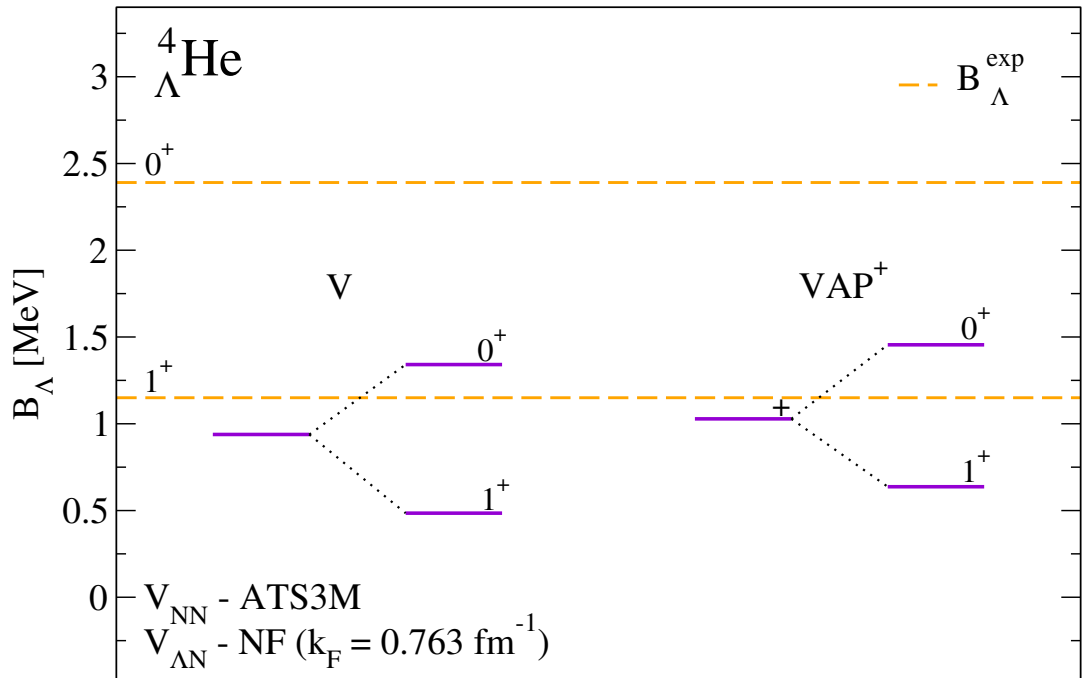

Figure 4.3: The Λ separation energies B_Λ of $^4_\Lambda$He obtained using the variation of a trial FMD state (V) and variation of an even parity projected trial FMD state (VAP$^+$), calculated with the ATS3M V_{NN} and NF $V_{\Lambda N}$ potentials. Variated trial states are further projected on the 0^+ ground and 1^+ excited states.

and 1^+ states while the $0^+ - 1^+$ splitting remains almost unchanged. This finding holds for all V_{NN} and $V_{\Lambda N}$ potentials used in our calculations.

It is to be noted that the results of previous calculations of ordinary nuclei [46] suggest that the effect of VAP$^\pi$ would be larger in more deformed hypernuclei. In the following we will present only the VAP$^\pi$ results which we consider more suitable for the description of hypernuclear bound states.

4.2   s-shell Λ hypernuclei

4.2.1 $^4_\Lambda$He hypernucleus

In this part, we present our theoretical study of $^4_\Lambda$He in the framework of FMD model. In order to check our numerical code, we first calculated the core nucleus ^{3}He and compared our results with similar calculations done by Neff using the same input [72]. In Table 4.2, we present the binding energy E_B, total rms radius R_T, and charge rms radius R_{charge} in ^{3}He calculated for the angular momentum and parity projected state $1/2^+$. The calculations were performed for the variation of the even parity projected state (VAP$^+$) using the V2M0.0, V2M0.6, MTV, and ATS3M potentials. The experimental values of ^{3}He binding energy and charge rms radius are shown in Table 4.2 for comparison.

Table 4.2: The binding energies E_B, total rms radii R_T, and charge rms radii R_{charge} of ^{3}He obtained using the variation of an even parity projected trial FMD state (VAP$^+$) and further projection on $1/2^+$ state. The calculations are performed using the V2M0.0, V2M0.6, MTV, and ATS3M V_{NN} potentials. The results are compared to the experimental values of E_B and R_{charge}.

^{3}He ($1/2^+$)	V2M0.0	V2M0.6	MTV	ATS3M	Exp.
E_B [MeV]	-7.180	-7.180	-6.449	-5.554	-7.718043(2) [73]
R_T [fm]	1.581	1.581	1.441	1.422	
R_{charge} [fm]	1.792	1.792	1.670	1.670	1.9506(14) [74]

In the $^4_\Lambda$He hypernucleus, the Λ separation energies $B_\Lambda = E_B(^3\text{He}; 1/2^+) - E_B(^4_\Lambda\text{He}; J^+)$ in the 0^+ ground state and 1^+ excited state were measured – $B_\Lambda^{exp}(0^+) = 2.39(3)$ MeV [75] and $B_\Lambda^{exp}(1^+) = 1.15(4)$ MeV [76]. In Figure. 4.4, we compare the Λ separation energy spectra in $^4_\Lambda$He calculated with the ATS3M V_{NN} potential and five different $V_{\Lambda N}$ potentials - the JA, JB, ND, NF, and NS. The value of Fermi momentum $k_F = 0.8$ fm^{-1} adopted from previous hypernuclear cluster calculations [21] was used for each $V_{\Lambda N}$. In the case of the JA, JB, and ND ΛN potentials, the variation procedure VAP$^+$ reaches the binding energy minimum that almost

Figure 4.4: The Λ separation energies B_Λ of $^4_\Lambda$He obtained using the variation of an even parity projected trial FMD state (VAP$^+$), calculated with the JA, JB, ND, NF, and NS $V_{\Lambda N}$ potentials ($k_F = 0.8$ fm^{-1}) and the ATS3M V_{NN} potential. Variated trial states ($+$) are further projected on the 0^+ and 1^+ eigenstates. In case of the JA, JB, and ND $V_{\Lambda N}$ potentials the projected 0^+ states were not obtained with sufficient numerical accuracy, therefore, their B_Λ is not shown.

exactly corresponds to the 1^+ ground state. This fact was checked by calculating their corresponding $< \hat{L}^2 >$, $< \hat{S}^2 >$, and $< \hat{J}^2 >$ expectation values. Consequently, we were not able to project out 0^+ eigenstates with a sufficient numerical accuracy. Therefore, they are not plotted in the figure. The resulting 1^+ ground state is in contradiction to experiment. This indicates a wrong ordering of the energy levels, which was also supported by previous calculations [21]. The minimization of the binding energy for the NF and NS $V_{\Lambda N}$ potentials yields the correct order of the Λ separation energy levels, in agreement with experiment. However, the NS $V_{\Lambda N}$ potential clearly overestimates the experimental value of the $0^+ - 1^+$ splitting. Thus, we consider the YNG-NF $V_{\Lambda N}$ potential as the most reliable out of the ΛN potentials discussed here and we applied it in the following $^4_\Lambda$He FMD calculations.

In Figure 4.5, we plot the total, nucleon, and Λ one-body densities in $^4_\Lambda$He many-body state $|Q\rangle$ denoted as ρ ($^4_\Lambda$He), ρ_{nuc}($^4_\Lambda$He), and ρ_Λ($^4_\Lambda$He), respectively. The parameters of the $^4_\Lambda$He many-body state are determined with the variation of the even parity projected trial FMD state $|Q; +\rangle = \frac{1}{2}(|Q\rangle + \hat{\Pi}|Q\rangle)$ (VAP$^+$) using the ATS3M V_{NN}, and NF ($k_F = 0.8$ fm^{-1}) $V_{\Lambda N}$ potentials. For comparison, we also show the total one-body density of the ^{3}He ρ (^{3}He) calculated with the VAP$^+$ using

the same V_{NN} potential. We observe that ρ_Λ ($^4_\Lambda$He) is slightly shifted to the right from the coordinate origin while the ρ_{nuc}($^4_\Lambda$He) is shifted to the left. Nevertheless, the center of mass of the $^4_\Lambda$He is located in the center. It is to be noted that after the projection on the total angular momentum J all densities are located in the center. The distribution of the total density of $^4_\Lambda$He in the plot seems to be spherical, however, the calculated inertia tensor indicates small deformation of the $^4_\Lambda$He state $|Q\rangle$. A thorough comparison of ρ_{nuc} ($^4_\Lambda$He) and ρ (^{3}He) shows that ρ_{nuc} ($^4_\Lambda$He) is slightly more dilute due to the presence of Λ. This finding is in agreement with the
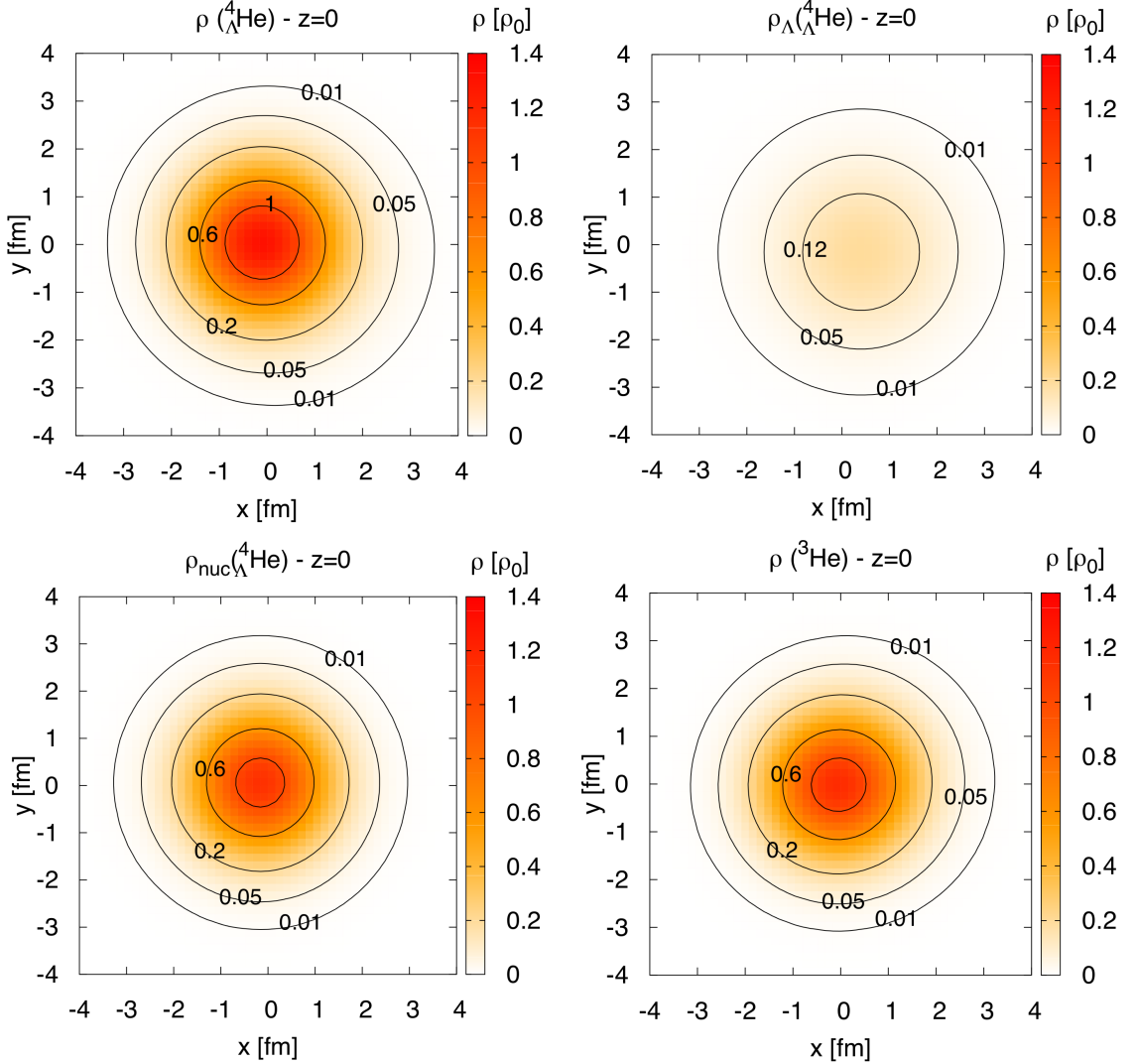
Figure 4.5: The total (ρ ($^4_\Lambda$He)), nucleon (ρ_{nuc}($^4_\Lambda$He)), and Λ (ρ_Λ($^4_\Lambda$He)) one-body densities of the $^4_\Lambda$He state $|Q\rangle$, shown in the xy,z=0 plane. The total one-body density of the ^{3}He state $|Q\rangle$ (ρ (^{3}He)) is presented as well. The parameters of the $^4_\Lambda$He and ^{3}He states $|Q\rangle$ are calculated by variation of the even parity projected states $|Q;+\rangle = \frac{1}{2}(|Q\rangle + \hat{\Pi}|Q\rangle)$ with the V_{NN} ATS3M potential. The $V_{\Lambda N}$ part of $^4_\Lambda$He is described by the NF potential ($k_{\text{F}} = 0.8$ fm^{-1}). The densities are in units of the nuclear saturation density $\rho_0 = 0.16$ fm^{-3}.
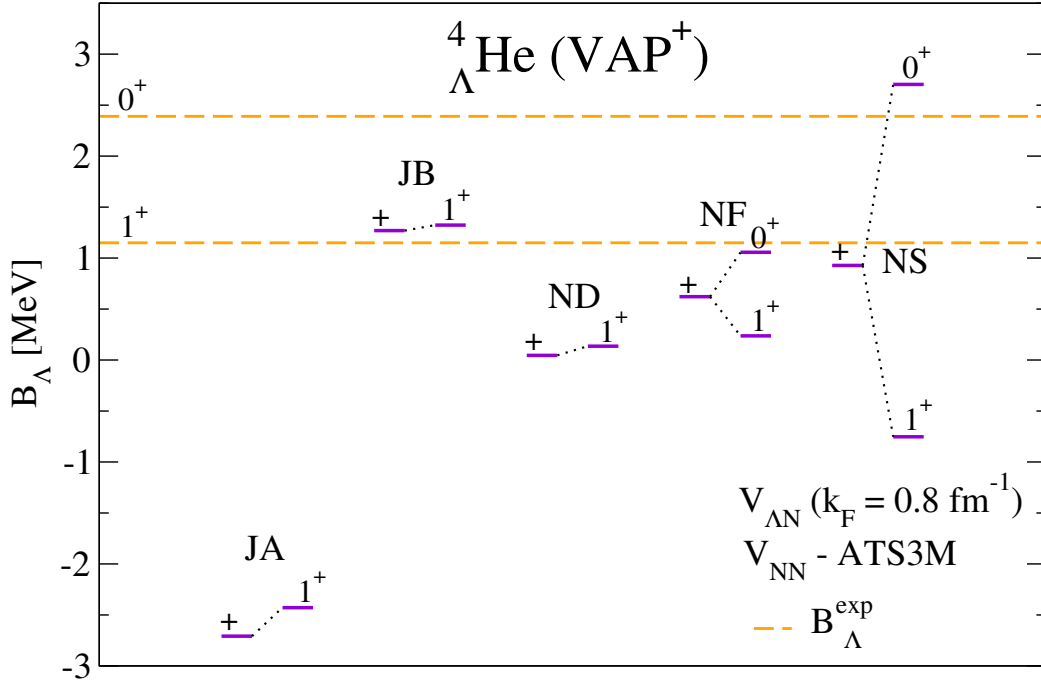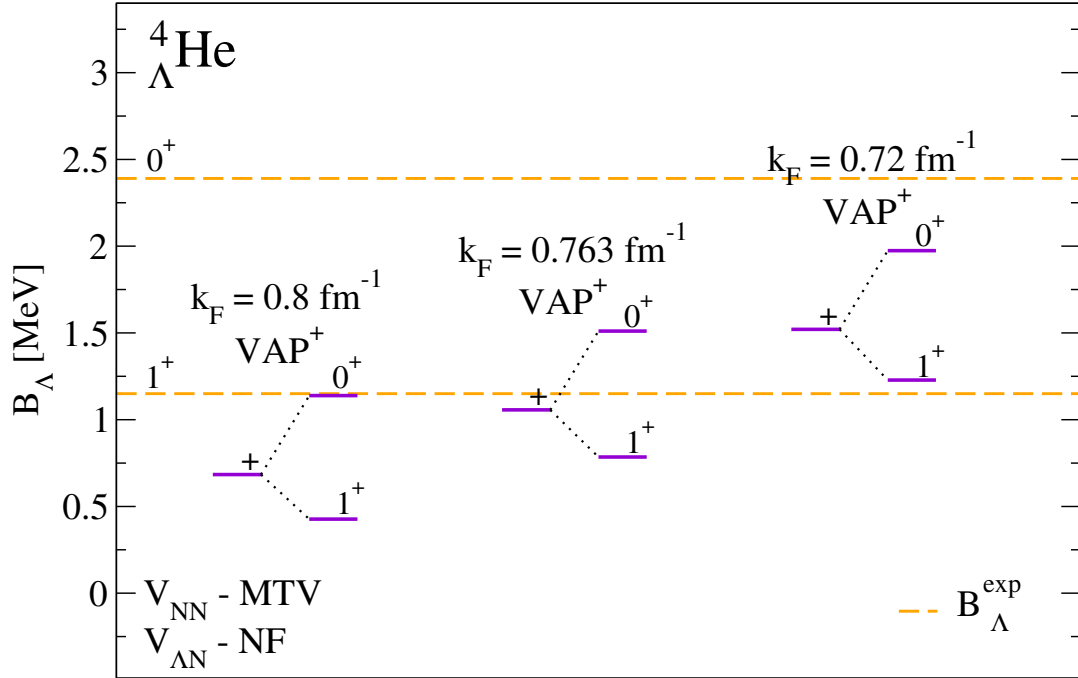
Figure 4.6: The Λ separation energies B_Λ of $^4_\Lambda$He obtained using the variation of an even parity projected trial FMD state (VAP$^+$) calculated with the MTV V_{NN} potential. The $V_{\Lambda N}$ part is described by the NF potential with different values of the Fermi momentum k_F. The variated states $(+)$ are further projected on the 0^+ ground and 1^+ excited states.

difference between $R_{\text{core}}(^4_\Lambda\text{He})$ and $R_{\text{T}}(^3\text{He})$ presented in Table 4.3 and Table 4.2, respectively.

An important aspect of the YNG potentials is their Fermi momentum dependence. The calculations presented so far were performed for one particular value of the Fermi momentum, $k_F = 0.8$ fm^{-1}. In Figure 4.6, we present the Λ separation energies B_Λ in $^4_\Lambda$He, calculated with the same V_{NN} and $V_{\Lambda N}$ potentials, but three different values of k_F. The value $k_F = 0.763$ fm^{-1} was determined from the calculations of the ^{3}He rms radius [77] and $k_F = 0.72$ fm^{-1} was used as a test value. We observe that the Fermi momentum acts as a scaling factor - Λ separation energies increase rapidly with decreasing k_F. The $0^+ - 1^+$ splitting changes only slightly (tens of keV) and also has an increasing tendency with decreasing k_F.

The k_F affects not only the binding of the Λ hyperon in the nuclear medium but also the modification of the nuclear core. In Table 4.3, we present our results of $^4_\Lambda$He calculations for three different k_F. Each calculation is performed using the NF ΛN interaction and the VAP$^+$ variation. We show the results for two different V_{NN} potentials - MTV (only central) and ATS3M (spin-isospin dependent). We observe that the total, Λ, and nucleon rms radii decrease with decreasing k_F. Therefore, we conclude that the $^4_\Lambda$He hypernucleus becomes more compact with decreasing Fermi

Table 4.3: The binding energies E_B, total rms radii R_T, charge rms radii R_charge, Λ rms radii R_Λ, rms radii of the nuclear core R_core, and differences $\Delta R_\mathrm{core} = R_\mathrm{core}(^4_\Lambda\mathrm{He}; J^+) - R_\mathrm{T}(^3\mathrm{He}; 1/2^+)$ of $^4_\Lambda\mathrm{He}$ obtained using the variation of an even parity projected trial FMD state (VAP$^+$) and further projection on the 0^+ ground state and 1^+ excited states. The calculations are performed using the MTV, and ATS3M V_{NN} potentials. The $V_{\Lambda N}$ part is described by the NF potential with different values of the Fermi momentum k_F.

$^4_\Lambda$He		MTV		ATS3M	
		0^+	1^+	0^+	1^+
$k_\mathrm{F} = 0.8$ fm^{-1}	E_B [MeV]	-7.588	-6.876	-6.611	-5.791
	R_T [fm]	1.649	1.649	1.635	1.636
	R_charge [fm]	1.812	1.812	1.815	1.816
	R_Λ [fm]	1.761	1.761	1.751	1.753
	R_core [fm]	1.442	1.442	1.428	1.428
	ΔR_core [fm]	0.001	0.001	0.006	0.006
$k_\mathrm{F} = 0.763$ fm^{-1}	E_B [MeV]	-7.960	-7.234	-7.009	-6.191
	R_T [fm]	1.629	1.629	1.616	1.617
	R_charge [fm]	1.801	1.801	1.805	1.805
	R_Λ [fm]	1.726	1.726	1.715	1.716
	R_core [fm]	1.435	1.435	1.421	1.421
	ΔR_core [fm]	-0.006	-0.006	-0.001	-0.001
$k_\mathrm{F} = 0.72$ fm^{-1}	E_B [MeV]	-8.424	-7.677	-7.508	-6.658
	R_T [fm]	1.607	1.607	1.595	1.595
	R_charge [fm]	1.788	1.788	1.792	1.793
	R_Λ [fm]	1.686	1.686	1.677	1.677
	R_core [fm]	1.426	1.426	1.412	1.413
	ΔR_core [fm]	-0.015	-0.015	-0.010	-0.009

momentum.

The comparison of the $^4_\Lambda$He rms radius of the nuclear core R_core in Table 4.3 with the total rms radius R_T in ^{3}He, given in Table 4.2, indicates the extent of the changes in the nuclear core due to the presence of Λ. The corresponding difference $\Delta R_\mathrm{core} = R_\mathrm{core}(^4_\Lambda\mathrm{He}) - R_\mathrm{core}(^3\mathrm{He})$ is shown in Table 4.3. We observe that for $k_\mathrm{F} = 0.8$ fm^{-1} the ^{3}He nuclear core slightly increases when Λ is bound in the system. On the other hand, in the case of $k_\mathrm{F} = 0.763$ fm^{-1} and $k_\mathrm{F} = 0.72$ fm^{-1} the nuclear core shrinks.

Figure 4.7 illustrates the modification of the nucleon one-body density distribu-
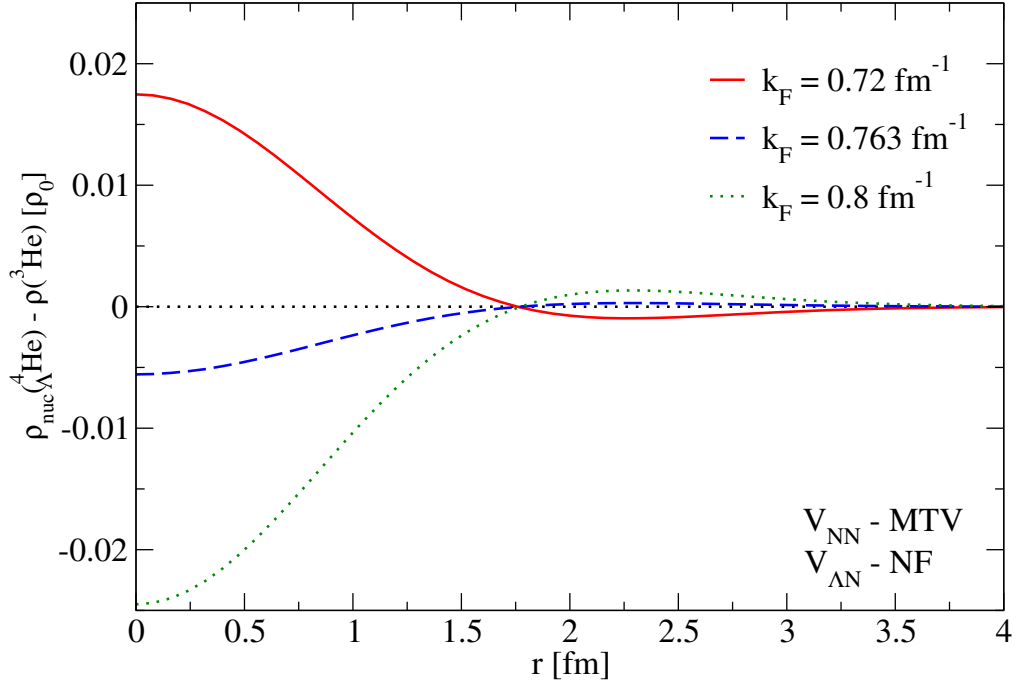
Figure 4.7: The difference between the nucleon radial one-body density ($\rho_{\mathrm{nuc}}(^4_\Lambda\mathrm{He})$) of the $^4_\Lambda$He state $|Q\rangle$ and total radial one-body density (ρ (^{3}He)) of the ^{3}He state $|Q\rangle$. The parameters of the $^4_\Lambda$He and ^{3}He states $|Q\rangle$ are calculated by variation of the basic FMD state (V) with the V_{NN} MTV potential. The $V_{\Lambda N}$ part of $^4_\Lambda$He is described by the NF potential with different values of the Fermi momentum k_F. The densities are in units of the nuclear saturation density $\rho_0 = 0.16$ fm^{-3}.

tion in the $^4_\Lambda$He hypernucleus with respect to ^{3}He. The FMD calculations of ^{3}He and $^4_\Lambda$He were performed using the MTV V_{NN} and NF $V_{\Lambda N}$ potentials by the variation of the basic FMD trial state (V). In this case the resulting many-body states of the variation process $|^3\mathrm{He}; Q\rangle$ and $|^4_\Lambda\mathrm{He}; Q\rangle$ are spherically symmetric. This allows us to study the radial density distribution difference $\rho_{\mathrm{nuc}}(^4_\Lambda\mathrm{He})(\mathrm{r}) - \rho$ (^{3}He)(r) for three selected values of k_F. We observe that for $k_F = 0.72$ fm^{-1} the difference is positive around the center of coordinates while it becomes negative for $k_F = 0.763$ fm^{-1}. The difference near the origin is even more negative for $k_F = 0.8$ fm^{-1}.

To a first approximation, the binding of the Λ hyperon in a nuclear system is mainly determined by the ΛN interaction. However, since the nuclear part of the total Hamiltonian (2.18) also participates in the variation process, the impact of the presence of the hyperon on the nuclear structure should depend on the V_{NN} potential as well. This feature allows us to indicate the effects coming from the nuclear core description. In Figure 4.8, we plot the Λ separation energies B_Λ of the $^4_\Lambda$He hypernucleus calculated for the same $V_{\Lambda N}$ potential (NF) but three different V_{NN} potentials - the MTV, ATS3M, and V2M0.6 potentials. We observe, that the separation energy B_Λ corresponding to an intrinsic state before the angular momentum
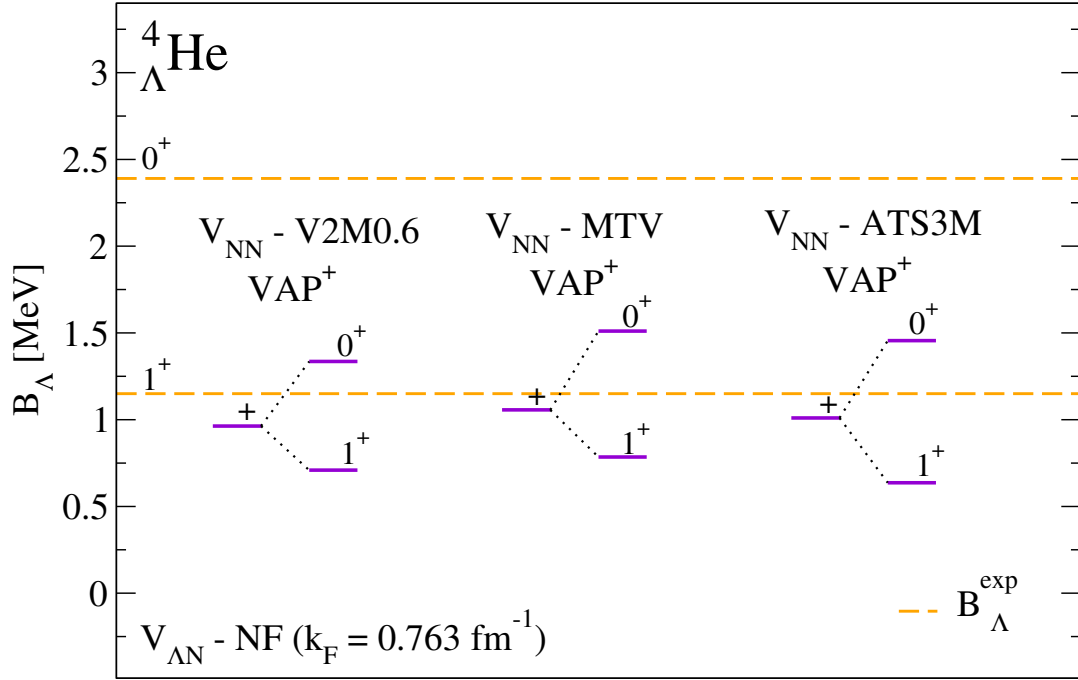
Figure 4.8: The Λ separation energies B_Λ of $^4_\Lambda$He obtained using the variation of an even parity projected trial FMD state (VAP$^+$) calculated with the V2M0.6, MTV, and ATS3M V_{NN} potentials and the NF $V_{\Lambda N}$ potential. The variated trial states (+) are further projected on the 0^+ ground and 1^+ excited states.

projection (denoted by '+') varies only slightly within tens of keV. However, after the angular momentum projection the Λ separation energies of the ground 0^+ and excited 1^+ states differ by few hundreds of keV, which is also reflected in the $0^+ - 1^+$ splitting.

In Table 4.4, we present energy differences between the individual contributions to the binding energies of the 0^+ and 1^+ states in $^4_\Lambda$He, calculated with the V2M0.0,

Table 4.4: The differences between the $B_\Lambda(0^+)$ and $B_\Lambda(1^+)$ Λ separation energies expressed in the form of individual contributions to the 0^+ - 1^+ splitting (in MeV). The T_{int}, V_{NN}, V_{NN}^σ, $V_{\Lambda N}$ and $V_{\Lambda N}^\sigma$ denote intrinsic kinetic energy, spin-independent part of V_{NN}, spin-dependent part of V_{NN}, spin-independent part of $V_{\Lambda N}$ and spin-dependent part of $V_{\Lambda N}$. The calculations are performed with the V2M0.0, V2M0.6, MTV, and ATS3M V_{NN} potentials and the NF ($k_{\text{F}} = 0.763$ fm^{-1}) $V_{\Lambda N}$ potential.

V_{NN} potential	ΔT_{int}	ΔV_{NN}	ΔV_{NN}^σ	$\Delta V_{\Lambda N}$	$\Delta V_{\Lambda N}^\sigma$	$|B_\Lambda(0^+) - B_\Lambda(1^+)|$
V2M0.0	10^{-4}	10^{-4}	-	10^{-5}	0.626	0.626
V2M0.6	10^{-4}	10^{-5}	10^{-5}	10^{-4}	0.625	0.626
MTV-UCOM	10^{-4}	10^{-5}	-	10^{-4}	0.726	0.726
ATS3M-UCOM	0.023	0.027	0.048	0.006	0.767	0.817

V2M0.6, MTV, and ATS3M V_{NN} potentials and the NF ($k_{\mathrm{F}} = 0.763$ fm^{-1}) $V_{\Lambda N}$ potential. We observe that the size of the $|B_\Lambda(0^+) - B_\Lambda(1^+)|$ splitting comes dominantly from the spin-dependent part of the $V_{\Lambda N}$ potential ($\Delta V_{\Lambda N}^\sigma$). Furthermore, the size of B_Λ splitting changes considerably for various V_{NN} potentials, as they predict a different level of the nuclear core modifications due to the presence of Λ.

4.2.2 $^4_\Lambda$H hypernucleus. Mirror hypernuclei $^4_\Lambda$He and $^4_\Lambda$H

Properties of the NN and ΛN interactions can be studied through mirror hypernuclei $^4_\Lambda$He and $^4_\Lambda$H. In the latter hypernuclear system, the experiment measures the same order of the Λ separation energy B_Λ levels as in the case of $^4_\Lambda$He - the 0^+ ground state and one 1^+ excited state. The experimental values are $B_\Lambda^{\mathrm{exp}}(^4_\Lambda$H$; 0^+) = 2.04(4)$ MeV [75] and $B_\Lambda^{\mathrm{exp}}(^4_\Lambda$H$; 1^+) = 1.04(5)$ MeV [76]. The differences between the Λ separation energies of $^4_\Lambda$He and $^4_\Lambda$H denoted as $E_{\mathrm{shift}} = B_\Lambda(^4_\Lambda$He$) - B_\Lambda(^4_\Lambda$H$)$ in the individual B_Λ levels are $E_{\mathrm{shift}}^{\mathrm{exp}}(0^+) = 0.35$ MeV and $E_{\mathrm{shift}}^{\mathrm{exp}}(1^+) = 0.11$ MeV. Since the YNG potentials do not distinguish between neutron and proton, the difference between the Λ separation energies comes exclusively from the NN-potential description of the nuclear core.

The binding energy E_{B}, total rms radius R_{T}, and charge rms radius R_{charge} of ^{3}H which forms the core of the $^4_\Lambda$H are shown in Table 4.5. The calculations are performed with the VAP$^+$ using the V2M0.0, V2M0.6, MTV, and ATS3M V_{NN} potentials. Again we compared our results with the FMD calculations of Neff [72]. Experimental value of E_{B} is shown for comparison.

Table 4.5: The binding energies E_{B}, total rms radii R_{T}, and charge rms radii R_{charge} of ^{3}H obtained using the variation of an even parity projected trial FMD state (VAP$^+$) and further projection on the $1/2^+$ state. The calculations are performed using the V2M0.0, V2M0.6, MTV, and ATS3M V_{NN} potentials. The results are compared to the experimental value of E_{B}.

^{3}H ($1/2^+$)	V2M0.0	V2M0.6	MTV	ATS3M	Exp.
E_{B} [MeV]	-7.191	-7.191	-6.463	-5.545	-8.481798(2) [73]
R_{T} [fm]	1.581	1.581	1.440	1.422	
R_{charge} [fm]	1.743	1.743	1.617	1.568	

In Table 4.6, we summarize the results of our VAP$^+$ calculations of the 0^+ and 1^+ states in $^4_\Lambda$H. The Λ separation energy B_Λ, change in the rms radius of the nuclear core ΔR_{core}, and the energy difference $E_{\mathrm{shift}} = B_\Lambda(^4_\Lambda$He$) - B_\Lambda(^4_\Lambda$H$)$ were calculated using the V2M0.0, V2M0.6, MTV, and ATS3M V_{NN} potentials and the YNG-NF $V_{\Lambda N}$ potential with $k_{\mathrm{F}} = 0.763$ fm^{-1}. We observe that the nuclear core of

Table 4.6: The binding energies E_B, Λ separation energies B_Λ, differences $B_\Lambda(^4_\Lambda\mathrm{He})-B_\Lambda(^4_\Lambda\mathrm{H})$, total rms radii R_T, charge rms radii R_charge, Λ rms radii R_Λ, rms radii of the nuclear core R_core, and differences $\Delta R_\mathrm{core} = R_\mathrm{core}(^4_\Lambda\mathrm{H}; J^+) - R_\mathrm{T}(^3\mathrm{H}; 1/2^+)$ of $^4_\Lambda\mathrm{H}$ obtained using the variation of an even parity projected trial FMD state (VAP$^+$) and further projection on the 0^+ ground and 1^+ excited states. The calculations are performed using the V2M0.0, V2M0.6, MTV, and ATS3M V_{NN} potentials. The $V_{\Lambda N}$ part is described by the NF potential with the value of Fermi momentum $k_\mathrm{F} = 0.763\ \mathrm{fm}^{-1}$.

$^4_\Lambda\mathrm{H}$	V2M0.0		V2M0.6	
	0^+	1^+	0^+	1^+
E_B [MeV]	-8.529	-7.892	-8.529	-7.899
B_Λ [MeV]	1.338	0.701	1.338	0.708
$B_\Lambda(^4_\Lambda\mathrm{He}) - B_\Lambda(^4_\Lambda\mathrm{H})$	-0.020	-0.005	-0.020	-0.016
R_T [fm]	1.734	1.734	1.734	1.734
R_charge [fm]	1.857	1.858	1.858	1.858
R_Λ [fm]	1.798	1.799	1.799	1.799
R_core [fm]	1.553	1.553	1.553	1.553
ΔR_core [fm]	-0.028	-0.028	-0.028	-0.028
$^4_\Lambda\mathrm{H}$	MTV		ATS3M	
	0^+	1^+	0^+	1^+
E_B [MeV]	-7.976	-7.243	-7.048	-6.209
B_Λ [MeV]	1.513	0.780	1.503	0.664
$B_\Lambda(^4_\Lambda\mathrm{He}) - B_\Lambda(^4_\Lambda\mathrm{H})$	-0.002	0.005	-0.048	-0.027
R_T [fm]	1.629	1.629	1.616	1.616
R_charge [fm]	1.749	1.749	1.700	1.700
R_Λ [fm]	1.726	1.726	1.716	1.716
R_core [fm]	1.435	1.435	1.420	1.421
ΔR_core [fm]	-0.005	-0.005	-0.002	-0.001

the $^4_\Lambda\mathrm{H}$ hypernucleus shrinks due to the presence of Λ for all V_{NN} potential types. The negative value of E_shift for all NN interactions indicates that the calculated spectrum of $^4_\Lambda\mathrm{H}$ lies slightly above the $^4_\Lambda\mathrm{He}$ spectrum (the difference is about tens of keV). Our results are thus in contrast to current experimental data.

Coulomb interaction

We tried to fix the aforementioned inconsistency in the calculated spectra of the mirror hypernuclei $^4_\Lambda\mathrm{He}$ and $^4_\Lambda\mathrm{H}$ by considering the Coulomb interaction. In Table 4.7, we present our VAP$^+$ results for the $^3\mathrm{He}$ nuclear system calculated including the

Coulomb interaction for the V2M0.0, V2M0.6, MTV, and ATS3M V_{NN} potentials. The contribution of the Coulomb interaction to the binding energy E_C calculated as the difference between the binding energies of the system with and without the Coulomb repulsion, $E_\mathrm{C} = E_\mathrm{B}^{\mathrm{Coul}} - E_\mathrm{B}$, is also presented. As expected, the ^{3}He rms radii increase due to the Coulomb repulsion. The contribution E_C to the ^{3}He binding energy differs only slightly for various V_{NN} potentials (tens of keV).

Table 4.7: The binding energies E_B, Coulomb energies $E_\mathrm{C} = E_\mathrm{B}^{\mathrm{Coul}} - E_\mathrm{B}$, total rms radii R_T, and charge rms radii R_charge of ^{3}He obtained using the variation of an even parity projected trial FMD state (VAP$^+$) and further projection on the $1/2^+$ ground state. The calculations are performed using the V2M0.0, V2M0.6, MTV, and ATS3M V_{NN} potentials with ($+$C) and without (no C) the Coulomb repulsion.

^{3}He ($1/2^+$)	V2M0.0		V2M0.6		MTV		ATS3M	
	no C	$+$ C	no C	$+$ C	no C	$+$ C	no C	$+$ C
E_B [MeV]	-7.180	-6.457	-7.180	-6.457	-6.449	-5.656	-5.554	-4.753
E_C [MeV]	0.723		0.723		0.793		0.801	
R_T [fm]	1.518	1.595	1.581	1.595	1.441	1.454	1.422	1.434
R_charge [fm]	1.792	1.807	1.792	1.806	1.670	1.683	1.670	1.681

In Table 4.8, we show the VAP$^+$ results of $^4_\Lambda$He calculations using the V2M0.0, V2M0.6, MTV, and ATS3M V_{NN} potentials. The hypernuclear part is described by the YNG-NF $V_{\Lambda N}$ potential with $k_\mathrm{F} = 0.763$ fm^{-1} and the Coulomb repulsion between protons is considered. We observe that the contribution of the Coulomb interaction to the $^4_\Lambda$He binding energy E_C is only slightly different from E_C in ^{3}He presented in Table 4.7. Consequently, the Λ separation energy remains almost unchanged and we do not observe any significant modification of E_shift.

The Coulomb interaction shifts the calculated $B_\Lambda(0^+)$ and $B_\Lambda(1^+)$ energy levels in $^4_\Lambda$He slightly downwards, even more below the B_Λ levels in $^4_\Lambda$H. The calculated Λ separation energies in the mirror hypernuclei $^4_\Lambda$He and $^4_\Lambda$H thus remain in conflict with experimental spectra. We conclude that the relative position of the calculated B_Λ spectra in $^4_\Lambda$He and $^4_\Lambda$H mainly depend on the applied ΛN interaction. The YNG $V_{\Lambda N}$ potentials used in our calculations do not contain the Charge Symmetry Breaking (CSB) operator terms which would distinguish between the Λp and Λn interactions. There are several attempts which describe the CSB effects in $^4_\Lambda$He and $^4_\Lambda$H by adding a phenomenological operator term to the $V_{\Lambda N}$ potential [19, 78]. Another way is to include $\Lambda - \Sigma$ mixing explicitly in the hypernuclear calculations [17].

Table 4.8: The binding energies E_{B}, Coulomb energies $E_{\mathrm{C}} = E_{\mathrm{B}}^{\mathrm{Coul}} - E_{\mathrm{B}}$, Λ separation energies B_{Λ}, differences $B_{\Lambda}(^4_{\Lambda}\mathrm{He}) - B_{\Lambda}(^4_{\Lambda}\mathrm{H})$, total rms radii R_{T}, charge rms radii R_{charge}, Λ rms radii R_{Λ}, rms radii of the nuclear core R_{core}, and differences $\Delta R_{\mathrm{core}} = R_{\mathrm{core}}(^4_{\Lambda}\mathrm{He}; J^+) - R_{\mathrm{T}}(^3\mathrm{He}; 1/2^+)$ of $^4_{\Lambda}\mathrm{He}$ obtained using the variation of an even parity projected trial FMD state (VAP$^+$) and further projection on the 0^+ ground and 1^+ excited states. The calculations are performed using the V2M0.0, V2M0.6, MTV, and ATS3M V_{NN} potentials considering the Coulomb repulsion. The $V_{\Lambda N}$ part is described by the NF potential with the value of Fermi momentum $k_{\mathrm{F}} = 0.763$ fm^{-1}.

$^4_{\Lambda}$He (Coulomb)	V2M0.0		V2M0.6	
	0^+	1^+	0^+	1^+
E_{B} [MeV]	-7.775	-7.153	-7.773	-7.149
E_{C} [MeV]	0.741	0.732	0.742	0.740
B_{Λ} [MeV]	1.318	0.696	1.316	0.692
$B_{\Lambda}(^4_{\Lambda}\mathrm{He}) - B_{\Lambda}(^4_{\Lambda}\mathrm{H})$	-0.020	-0.005	-0.022	-0.016
R_{T} [fm]	1.745	1.745	1.745	1.745
R_{charge} [fm]	1.919	1.919	1.918	1.918
R_{Λ} [fm]	1.806	1.806	1.806	1.806
R_{core} [fm]	1.564	1.564	1.564	1.564
ΔR_{core} [fm]	-0.031	-0.031	-0.031	-0.031
$^4_{\Lambda}$He (Coulomb)	MTV		ATS3M	
	0^+	1^+	0^+	1^+
E_{B} [MeV]	-7.157	-6.429	-6.224	-5.430
E_{C} [MeV]	0.803	0.805	0.785	0.761
B_{Λ} [MeV]	1.501	0.773	1.471	0.677
$B_{\Lambda}(^4_{\Lambda}\mathrm{He}) - B_{\Lambda}(^4_{\Lambda}\mathrm{H})$	-0.012	-0.007	-0.032	0.013
R_{T} [fm]	1.638	1.638	1.624	1.625
R_{charge} [fm]	1.812	1.812	1.814	1.814
R_{Λ} [fm]	1.731	1.732	1.721	1.722
R_{core} [fm]	1.445	1.445	1.430	1.430
ΔR_{core} [fm]	-0.009	-0.009	-0.004	-0.004

4.2.3 $^5_{\Lambda}$He hypernucleus

An important feature of the $^5_{\Lambda}$He hypernucleus is its rather compact ^{4}He nuclear core, which is a double magic nucleus. Therefore, the modifications of the ^{4}He core due to the presence of the Λ hyperon are expected to be almost negligible. In the case of $^5_{\Lambda}$He, only the energy of the $1/2^+$ ground state was measured, $B_{\Lambda} = 3.12(2)$ MeV [75].

First, we present our VAP$^+$ results for the ^{4}He core nucleus. In Table 4.9, we show

the binding energy E_B, total rms radius R_T, and charge rms radius R_{charge} of ^{4}He for the V2M0.0, V2M0.6, MTV, and ATS3M V_{NN} potentials. The experimental values of the ^{4}He are shown for comparison. We observe that the V2M0.0 and V2M0.6 V_{NN} potentials provide reasonable description of ^{4}He, while the MTV potential overbinds the system.

Table 4.9: The binding energies E_B, total rms radii R_T, and charge rms radii R_{charge} of ^{4}He obtained using the variation of an even parity projected trial FMD state (VAP$^+$) and further projection on the 0^+ ground state. The calculations are performed using the V2M0.0, V2M0.6, MTV, and ATS3M V_{NN} potentials. The results are compared to the experimental values of E_B, and R_{charge}.

^{4}He (0^+)	V2M0.0	V2M0.6	MTV	ATS3M	Exp.
E_B [MeV]	-28.794	-28.794	-30.399	-28.095	-28.296† [79]
R_T [fm]	1.454	1.454	1.320	1.327	
R_{charge} [fm]	1.664	1.664	1.549	1.554	1.681(4) [80]

†no error reported

In the previous calculations [18], the Fermi momentum parameter k_F of YNG $V_{\Lambda N}$ potentials was chosen to reproduce the experimental Λ separation energy in the $^5_\Lambda$He ground state. In our FMD calculations, we adopted the same approach for different V_{NN} potentials in order to investigate model dependence.

In Figure 4.9, we plot the calculated Λ separation energy B_Λ in $1/2^+$ ground state of $^5_\Lambda$He using the YNG-NF ΛN interaction with different values of k_F - 0.880, 0.895, 0.910, 0.925, and 0.940 fm^{-1}. Various V_{NN} potential models are considered - V2M0.0, V2M0.6, MTV, and ATS3M. We observe that the value of B_Λ increases linearly with decreasing k_F for all NN interactions. In the case of the V2M0.0 and V2M0.6 NN potentials we receive identical behavior of the $B_\Lambda(k_F)$. The MTV V_{NN} potential model shifts the $B_\Lambda(k_F)$ upward, while for the ATS3M NN potential the $B_\Lambda(k_F)$ line is moved downward. The optimal values of k_F that reproduce the experimental Λ separation energy for each V_{NN} potential are then determined using the linear regression. We receive the following Fermi momenta - $k_F^{V2M0.0} = 0.904$ fm^{-1}, $k_F^{V2M0.6} = 0.904$ fm^{-1}, $k_F^{MTV} = 0.909$ fm^{-1}, and $k_F^{ATS3M} = 0.892$ fm^{-1}. We clearly see that the optimal values of k_F for the above NN potentials are rather different.

In Table 4.10, we summarize our FMD VAP$^+$ results for $^5_\Lambda$He using the V2M0.0, V2M0.6, MTV, and ATS3M V_{NN} potentials. The ΛN interaction is described by the YNG-NF potential. Based on the above discussion, we adopt the value of the Fermi momentum parameter $k_F = 0.900$ fm^{-1} that best reproduces (in bulk) the experimental value of the $B_\Lambda(1/2^+)$ for various V_{NN} interactions used in this work.
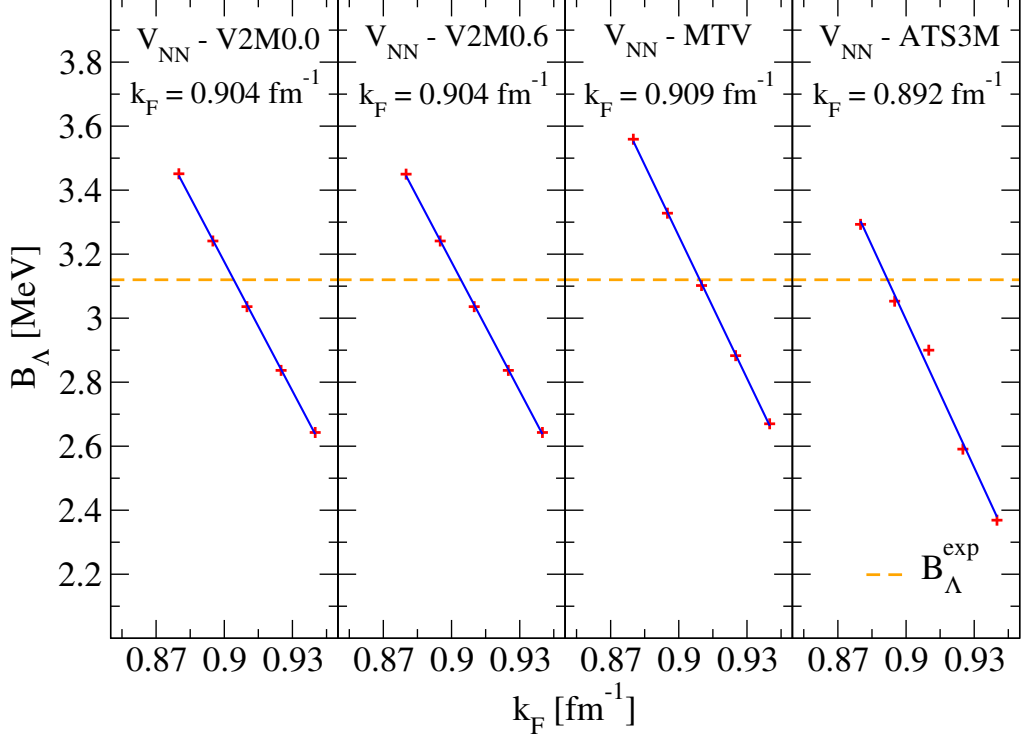
Figure 4.9: The dependence of the Λ separation energy B_Λ in the $1/2^+$ ground state of $^5_\Lambda$He on the value of the Fermi momentum k_F, calculated using the VAP$^+$ and the V2M0.0, V2M0.6, MTV, and ATS3M V_{NN} potentials. The $V_{\Lambda N}$ part is described by the NF potential. The dependence for each V_{NN} potential is fitted (blue line) and the optimal value of k_F which reproduces the $B_\Lambda = 3.12(2)$ MeV [75] (dashed line) is determined.

Table 4.10: The binding energies E_B, Λ separation energies B_Λ, total rms radii R_T, charge rms radii R_{charge}, Λ rms radii R_Λ, rms radii of the nuclear core R_{core}, and differences $\Delta R_{\text{core}} = R_{\text{core}}(^5_\Lambda\text{He}; 1/2^+) - R_T(^4\text{He}; 0^+)$ of $^5_\Lambda$He obtained using the variation of an even parity projected trial FMD state (VAP$^+$) and further projection on the $1/2^+$ ground state. The calculations are performed using the V2M0.0, V2M0.6, MTV, and ATS3M V_{NN} potentials. The $V_{\Lambda N}$ part is described by the NF potential with the value of Fermi momentum $k_F = 0.900$ fm^{-1}.

$^5_\Lambda$He $(1/2^+)$	V2M0.0	V2M0.6	MTV	ATS3M
E_B [MeV]	-31.966	-31.966	-33.651	-31.070
B_Λ [MeV]	3.172	3.172	3.252	2.975
R_T [fm]	1.598	1.598	1.501	1.501
R_{charge} [fm]	1.740	1.740	1.636	1.641
R_Λ [fm]	1.780	1.780	1.742	1.724
R_{core} [fm]	1.446	1.446	1.324	1.333
ΔR_{core} [fm]	-0.008	-0.008	0.004	0.006

4.3 p-shell Λ hypernucleus $^{7}_{\Lambda}$Li

In this section, we present our study of the p-shell hypernucleus $^{7}_{\Lambda}$Li. The γ-ray transitions between the individual energy levels of $^{7}_{\Lambda}$Li allowed to measure the Λ single-particle spectrum with relatively high accuracy [9]. Therefore, the study of $^{7}_{\Lambda}$Li serves as a good test of various hypernuclear models as well as $V_{\Lambda N}$ potentials.

In our calculations of $^{7}_{\Lambda}$Li, we were limited to the ATS3M V_{NN} potential, as the only potential out of those considered here capable of describing the nuclear core heavier than ^{4}He. The V2M0.0, V2M0.6, and MTV V_{NN} interactions noticeably overbind the ^{6}Li core and therefore do not yield physically meaningful results.

In order to check our numerical code, we first calculated the core nucleus ^{6}Li and compared our results with similar calculations done by Neff using the same ATS3M V_{NN} potential [72]. In Table 4.11, we present the binding energies E_{B}, total rms radii R_{T}, and charge rms radii R_{charge} in ^{6}Li determined for the angular momentum and parity projected states ('J^{+}'). The calculations were performed for the variation of the even parity projected state (VAP^{+}). The experimental values of the 1^{+} ground state binding energy in ^{6}Li is shown in Table 4.11 for comparison. The calculated 1^{+} ground state in ^{6}Li is less bound (by about 8 MeV) and the R_{charge} is smaller than the experimental value, as well. We observe that our results of rms radii in all projected states differ only slightly from each other.

Table 4.11: The binding energies E_{B}, total rms radii R_{T}, and charge rms radii R_{charge} of ^{6}Li obtained using the variation of an even parity projected trial FMD state (VAP^{+}) and further projection on J^{+} states. Only the eigenstates obtained with sufficient numerical accuracy are shown. The calculations are performed using the ATS3M V_{NN} potential. The results are compared to the experimental values of E_{B} of the ^{6}Li ground state.

^{6}Li	ATS3M				Exp.
	1^{+}	3^{+}	2^{+}	1^{+}	
E_{B} [MeV]	-23.837	-20.299	-20.298	-20.297	-31.993† [79]
R_{T} [fm]	2.049	2.060	2.060	2.060	
R_{charge} [fm]	2.203	2.213	2.213	2.213	

†no error reported

The calculated excitation energy ($E_{\mathrm{x}} = E_{\mathrm{B}}(J^{+}) - E_{\mathrm{B}}^{\mathrm{g.s}}$) spectrum of ^{6}Li is compared with the measured excitation levels [81] in Figure 4.10. The ground state quantum numbers 1^{+} are in agreement with experiment. However, the excitation levels in ^{6}Li are not well reproduced. We observe a wrong ordering as well as position of individual excitation levels which are grouped around the $E_{\mathrm{x}} = 3.54$ MeV.
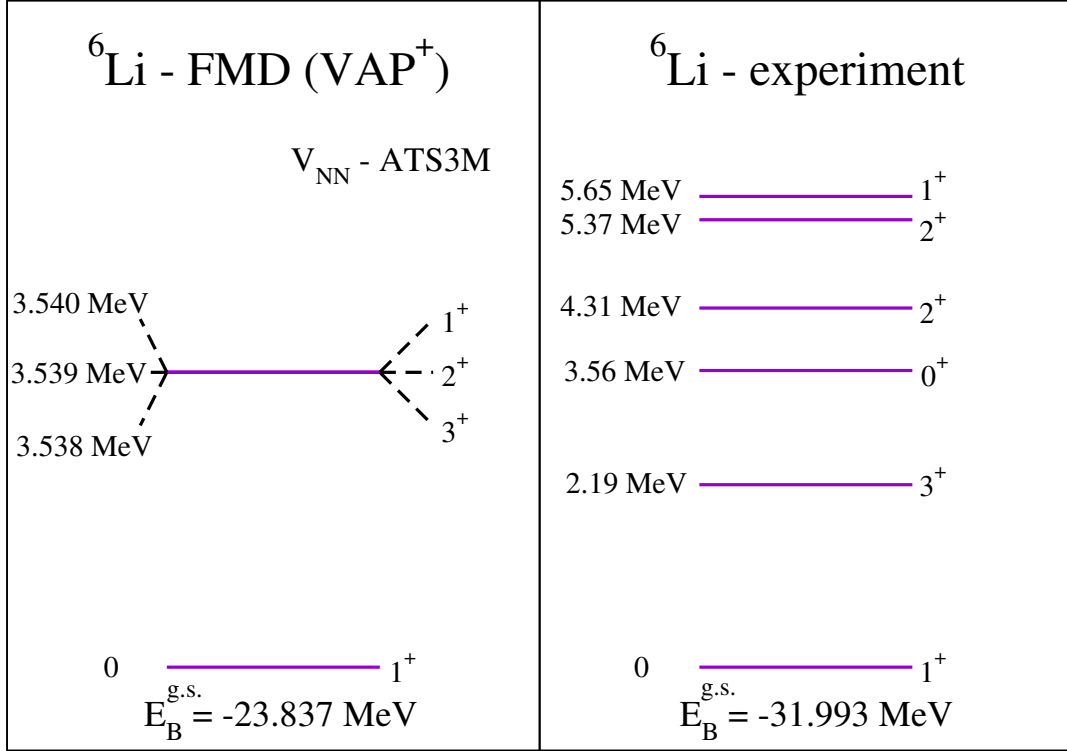
Figure 4.10: Comparison of the calculated (left panel) and experimental [81] (right panel) excitation spectra of ^{6}Li. The calculated energies $E_x(J^+) = E_B(J^+) - E_B^{g.s}$ of each J^+ level in ^{6}Li are determined from values in Table 4.11.

This indicates that a more sophisticated NN potential is required for the correct description of ^{6}Li.

We present our VAP$^+$ calculation of $^7_\Lambda$Li using the same ATS3M V_{NN} potential in Table 4.12. The ΛN interaction is described by the YNG-NS $V_{\Lambda N}$ potential with the Fermi momentum parameter $k_F = 0.95$ fm^{-1} adopted from the previous studies [21]. We also applied the YNG-NF ΛN interaction (using the same k_F), however, we did not get any Λ bound state in B_Λ in $^7_\Lambda$Li. For the YNG-NS $V_{\Lambda N}$ potential, the calculated Λ separation energy in the $^7_\Lambda$Li ground state is about 1.5 MeV off the experimental value $B_\Lambda^{g.s., \, exp} = 5.58(3)$ MeV [75], and moreover, its quantum numbers are $J^\pi = 3/2^+$ instead of experimentally determined $1/2^+$. The negative value of $\Delta R_{core} = R_{core}(^7_\Lambda\text{Li}; J^+) - R_T^{g.s}(^6\text{Li})$ in each angular momentum and parity projected state of $^7_\Lambda$Li indicates that the nuclear core shrinks due to the presence of Λ. This finding is in agreement with the observed nuclear core modification in $^7_\Lambda$Li which confirmed the "glue-like" role of the Λ hyperon [14].

In Figure 4.11, we compare the calculated excitation energy spectrum of $^7_\Lambda$Li with the results of hypernuclear γ-ray spectroscopy. Our calculation (left panel) exhibits considerable inconsistency with measured experimental data (right panel). This can be partly attributed to the rather simple ATS3M V_{NN} potential that is not

Table 4.12: The binding energies E_B, Λ separation energies B_Λ, total rms radii R_T, charge rms radii R_charge, Λ rms radii R_Λ, rms radii of the nuclear core R_core, and differences $\Delta R_\text{core} = R_\text{core}(^7_\Lambda\text{Li}; J^+) - R_\text{T}^\text{g.s.}(^6\text{Li})$ of $^7_\Lambda\text{Li}$ obtained using the variation of an even parity projected trial FMD state (VAP$^+$) and further projection on J^+ states. Only the eigenstates obtained with sufficient numerical accuracy are shown. The calculations are performed using the ATS3M V_{NN} potential and NF $V_{\Lambda N}$ potential with the value of Fermi momentum $k_\text{F} = 0.950$ fm^{-1}.

$^7_\Lambda\text{Li}$	ATS3M				
	$3/2^+$	$1/2^+$	$7/2^+$	$3/2^+$	$5/2^+$
E_B [MeV]	-27.853	-24.128	-24.115	-24.014	-23.930
B_Λ [MeV]	4.016	0.291	0.278	0.177	0.093
R_T [fm]	1.944	1.949	1.950	1.950	1.950
R_charge [fm]	2.124	2.130	2.130	2.130	2.130
R_Λ [fm]	1.845	1.843	1.843	1.843	1.843
R_core [fm]	1.929	1.936	1.936	1.936	1.936
ΔR_core [fm]	-0.120	-0.113	-0.113	-0.113	-0.113

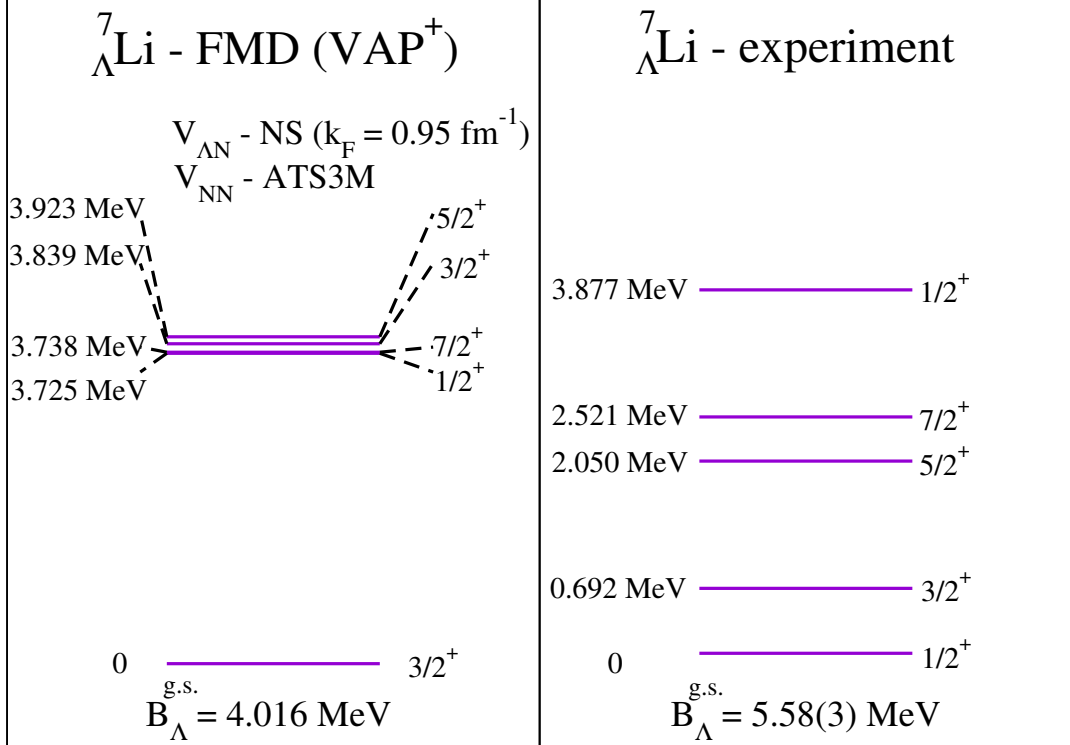

Figure 4.11: Comparison of the calculated (left panel) and experimental [9] (right panel) excitation spectra of $^7_\Lambda\text{Li}$. The calculated energies $E_\text{x}(J^+) = E_\text{B}(J^+) - E_\text{B}^\text{g.s}$ of each J^+ level in $^7_\Lambda\text{Li}$ are determined from values in Table 4.12.

able to satisfactorily describe the ^{6}Li nuclear core (see Fig. 4.11), which affects the theoretical prediction of the excitation spectrum in $^7_\Lambda$Li.

Cluster structure in $^7_\Lambda$Li

The effect of the Λ hyperon on the internal cluster structure of ^{6}Li is an interesting issue. Various cluster model calculations explicitly assume that the $^7_\Lambda$Li hypernuclear system is composed of the alpha, deuteron, and Λ degrees of freedom ($\alpha d\Lambda$) [21]. On the other hand, the FMD model allows us to study the structure of $^7_\Lambda$Li as a consequence of the variation method and the baryon-baryon interactions involved.

In Figure 4.12, we show the total, nucleon, and Λ one-body densities in $^7_\Lambda$Li many-body state $|Q\rangle$ denoted as $\rho\,(^7_\Lambda\text{Li})$, $\rho_\text{nuc}(^7_\Lambda\text{Li})$, and $\rho_\Lambda(^7_\Lambda\text{Li})$, respectively. The parameters of the $^7_\Lambda$Li many-body state are determined within the variation of the even parity projected trial FMD state $|Q; +\rangle = \frac{1}{2}(|Q\rangle + \hat{\Pi}\,|Q\rangle)$ (VAP$^+$) using the ATS3M V_{NN}, and YNG-NS ($k_\text{F} = 0.95$ fm^{-1}) $V_{\Lambda N}$ potentials. For comparison, we also present the total one-body density $\rho\,(^6\text{Li})$ calculated with the VAP$^+$ using the same V_{NN} potential. The $\rho_\text{nuc}(^7_\Lambda\text{Li})$ clearly indicates the internal $\alpha + d$ cluster structure of the nuclear core where the α (d) cluster is located in the upper-right (lower-left) part of the plot, while the $\rho_\Lambda(^7_\Lambda\text{Li})$ is affected by the the Λ hyperon which is located in the middle. The comparison between the $\rho_\text{nuc}(^7_\Lambda\text{Li})$ and $\rho\,(^6\text{Li})$ one-body densities reveals the "glue-like" role of Λ which moves the α and d clusters forming the nuclear core closer together.
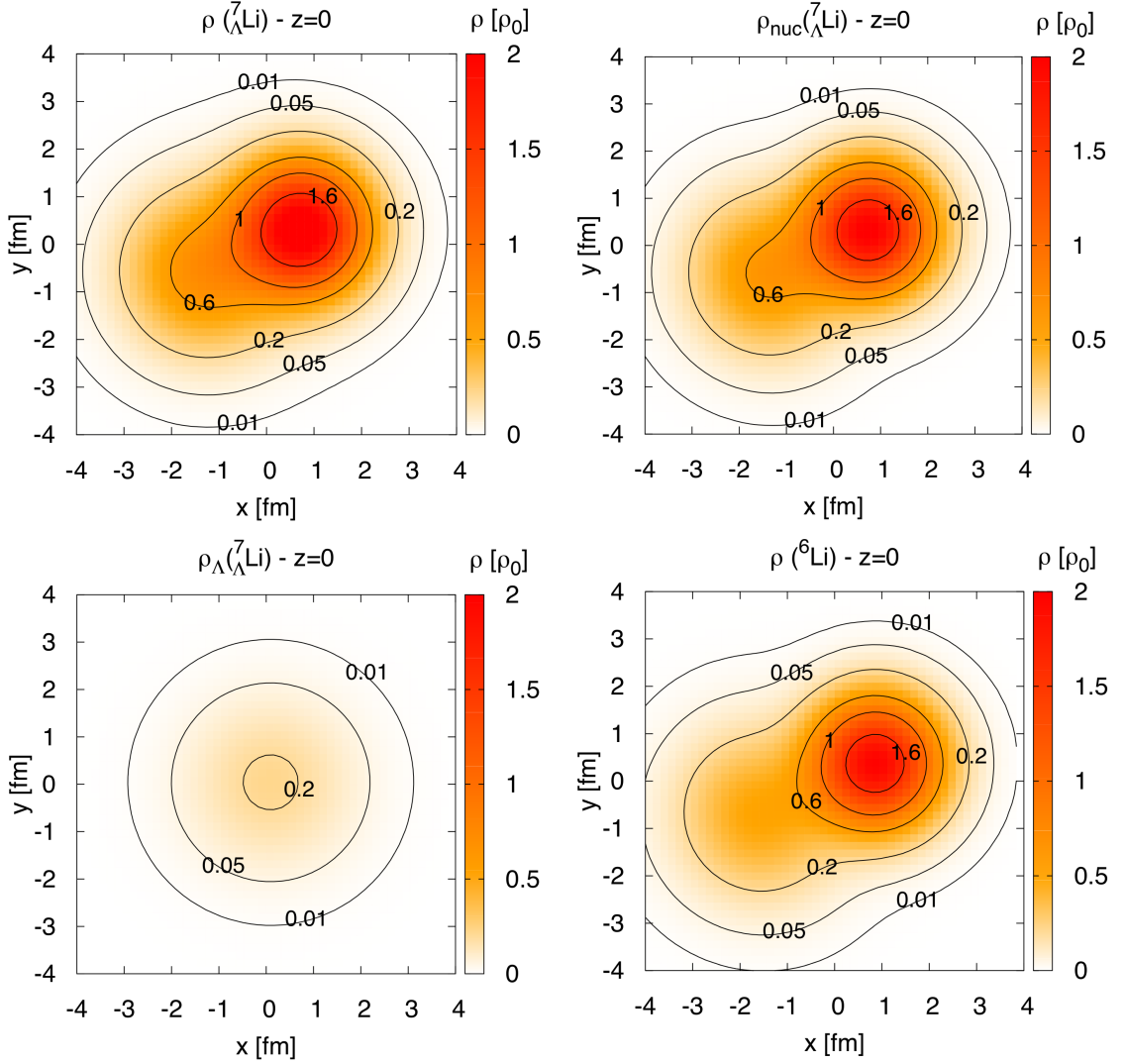
Figure 4.12: The total $\rho\left(^7_\Lambda\text{Li}\right)$, nucleon $(\rho_{\text{nuc}}(^7_\Lambda\text{Li}))$, and Λ $(\rho_\Lambda(^7_\Lambda\text{Li}))$ one-body densities of the $^7_\Lambda$Li state $|Q\rangle$, shown in the xy,z=0 plane. The total one-body density of the ^{6}Li state $|Q\rangle$ $(\rho\,(^6\text{Li}))$ is presented as well. The parameters of the $^7_\Lambda$Li and ^{6}Li states $|Q\rangle$ are calculated by variation of the even parity projected states $|Q;+\rangle = \frac{1}{2}(|Q\rangle + \hat{\Pi}\,|Q\rangle)$ with the V_{NN} ATS3M potential. The $V_{\Lambda N}$ part of $^7_\Lambda$Li is described by the NS potential ($k_\text{F} = 0.950$ fm^{-1}). The densities are in units of the nuclear saturation density $\rho_0 = 0.16$ fm^{-3}.

Chapter 5

Conclusions

In this work, we presented the first hypernuclear calculations using our recently developed Fermionic Molecular Dynamics (FMD) code. We studied the s-shell Λ hypernuclei $^4_\Lambda$H, $^4_\Lambda$He, and $^5_\Lambda$He and p-shell Λ hypernucleus $^7_\Lambda$Li in order to discuss main features of our calculations. The ground as well as excited states of hypernuclear systems were obtained variationally. We compared the convergence and the results of the variation for two different types of trial many-body states - the basic FMD state (V) and even parity projected FMD state (VAP$^+$). The NN and ΛN interactions were described by several kinds of relatively simple V_{NN} potentials - the V2M0.0, V2M0.6, MTV and ATS3M, and $V_{\Lambda N}$ potentials - the YNG-JA, JB, ND, NF, and NS which were available during the development of our FMD code. The wider range of NN and ΛN interactions allowed us to illustrate the potential model dependence of our calculations. We studied structure of light nuclear as well as Λ hypernuclear systems and the modification of the nuclear structure due to the presence of the Λ hyperon.

A substantial part of this work was devoted to the development of the FMD code. We used two different algorithms - the L-BFGS-B and SQP which minimize the expectation value of the binding energy. In order to test their correct implementation, we successfully checked that in case of nuclear calculations with the basic FMD trial state (V), both algorithms converged to the same minimum of the particular nuclear system. The implementation of the more advanced SQP algorithm proved to be crucial for later development of this work. It allowed us to impose additional equality bounds, and thus, minimize the expectation value of the binding energy involving parity operators. Therefore, we were able to apply the YNG $V_{\Lambda N}$ potentials in their spin-parity channels but also improve the variation using basic FMD trial state (V) by the variation using parity projected trial state (VAP$^\pi$). We revealed that the VAP$^\pi$ with the parity coinciding with the parity of the ground or excited states of (hyper)nuclei yields in general lower binding energy minimum and therefore pro-

vides better description of the variated system. However this improvement due to the consideration of equality bounds comes at a cost of greater computational complexity. The correctness of our FMD code was tested on hypernuclear calculations and its nuclear part was compared with the results of Neff [72].

We considered several versions of the YNG $V_{\Lambda N}$ potentials. We observed that their predictions for hypernuclei rather differ from each other, only the NF and NS $V_{\Lambda N}$ potentials reproduce correct ordering in the $^4_\Lambda$He excitation spectrum. However the NS clearly overestimates the experimental value of the $0^+ - 1^+$ splitting in $^4_\Lambda$He. In the calculation of $^7_\Lambda$Li, the NF potential did not bind the Λ in the ^{6}Li nuclear core, therefore, we presented our results for the YNG-NS $V_{\Lambda N}$ potential. We were not able to distinguish whether this inconsistency between NF and NS in the $^7_\Lambda$Li description was purely due to the $V_{\Lambda N}$ potentials or because of the ^{6}Li nuclear core which were not satisfactorily reproduced.

The influence of the Fermi momentum parameter k_{F} of the YNG $V_{\Lambda N}$ potentials on hypernuclear observables was studied as well. We found rather strong dependence on k_{F}. In the s-shell hypernuclei the Fermi momentum acts as a scaling factor – the Λ separation energies increase with decreasing k_{F}. The 0^+ and 1^+ splitting in $^4_\Lambda$H and $^4_\Lambda$He changes only slightly. We also observed that rms radii of s-shell hypernuclei decrease with decreasing k_{F}, and thus, they become more compact.

We tested the effect of various NN interactions on the predictions of hypernuclear observables. We found that the description of the nuclear core using different V_{NN} potentials has to be taken into account. The differences in the Λ separation energies between considered V_{NN} potentials are relatively small in $^4_\Lambda$H and $^4_\Lambda$He, however, their significance grows in $^5_\Lambda$He. We found that these effects could be partly solved in $^5_\Lambda$He by choosing a suitable value of k_{F} for each V_{NN} potential separately. However, this procedure can not be straightforwardly extended to hypernuclei with rather rich excitation spectrum, since the Fermi momentum also affects the spacing between individual excitation levels.

The Λ separation energies of s-shell hypernuclei were satisfactorily reproduced. However, the calculation of the p-shell $^7_\Lambda$Li hypernucleus yielded considerable inconsistency with experimental data, which we attributed to the rather simple ATS3M V_{NN} potential used. We conclude that in the future it will be necessary to apply more sophisticated NN interactions. We also studied the experimentally observed shift between the B_Λ spectra of mirror hypernuclei $^4_\Lambda$H and $^4_\Lambda$He with and without the Coulomb repulsion. Their relative position depends mainly on the applied ΛN interaction. The YNG $V_{\Lambda N}$ potentials used in our calculations do not contain the Charge Symmetry Breaking (CSB) operator terms which would distinguish between the Λp and Λn interactions. Therefore the calculated B_Λ spectrum in $^4_\Lambda$He is shifted

downward with respect to $^4_\Lambda$H, which is in contradiction to the experiments. There are several attempts which describe the CSB effects in $^4_\Lambda$He and $^4_\Lambda$H by adding a phenomenological operator term to the $V_{\Lambda N}$ potential [19, 78]. Another way is to include $\Lambda - \Sigma$ mixing explicitly in the hypernuclear calculations [17].

We conclude that the s-shell hypernuclei have too compact nuclear core to be noticeably modified by the presence of the Λ hyperon. In our s-shell calculations, the Λ hyperon is localized roughly in the center of nuclear core and causes almost negligible modifications. However, in $^7_\Lambda$Li, the Λ hyperon is localized just in the middle between the α and d cluster of the ^{6}Li nuclear core and pulls them closer together. This revealed the "glue-like" role of the Λ, which is in agreement with the experiment [14].

As a next step, we should incorporate more sophisticated V_{NN} and $V_{\Lambda N}$ potentials, such as those derived from chiral effective field theory. Moreover, $\Lambda - \Sigma$ mixing which plays important role in realistic hypernuclear calculations should be included. It is also desirable to study the role of three body forces. We also intend to extend our calculations to heavier hypernuclei and investigate the effect of the Λ hyperon on the intrinsic nuclear clusterization.

Appendix A

Expectation values of antisymmetrized many-body FMD state

In this Appendix, we briefly discuss the antisymmetrization of the FMD many-body wave function and we present the derivation of the one-body expectation value formula (2.14). We give a brief description of some observables and also techniques concerning their calculations. Since we evaluate the expectation values of the antisymmetrized many-body state $|Q\rangle$ analytically using Eqs. 2.14, we also present the expressions for one and two-body matrix elements of corresponding operators.

Antisymmetrized many-body wave function in FMD

We adopt the antisymmetrization operator $\hat{A}$ in a form

$$\hat{A} = \frac{1}{N!} \sum_{P_i} \mathrm{sgn}(P_i) \hat{P}_i, \tag{A.1}$$

where $\hat{P}_i$ denote the permutation operators acting among all particles in the N-body state. Consequently, the antisymmetrized many-body FMD wave function is expressed as a Slater determinant (2.1) where the generalized coordinate $|x_i\rangle = |\boldsymbol{x_i}, \chi_i, \xi_i\rangle$ stands for position, spin, and isospin of the i-th fermion. In this work, we describe systems consisting of three mutually distinguishable types of baryons - protons, neutrons, and the Λ hyperon.

In Eq. A.2, we demonstrate on the example of $^{5}_{\Lambda}\mathrm{He}$ that the many-body wave functions defined in Eq.2.1 are properly antisymmetrized. This is ensured by the third components of isospin.

We denote the isospin degrees of freedom as p (proton), n (neutron), and Λ. Only the diagonal single-particle state overlaps in isospin space (2.13), i.e. T_{pp}, T_{nn}, and $T_{\Lambda\Lambda}$, are equal to one, otherwise they are equal to zero.

$$\langle x_1^p; x_2^p; x_3^n; x_4^n; x_5^\Lambda | \hat{A} | Q \rangle = \frac{1}{N!} \sum_{P_i} \text{sgn}(P_i) \langle x_1^p | q_{P_i(1)}^p \rangle \langle x_2^p | q_{P_i(2)}^n \rangle \langle x_3^n | q_{P_i(3)}^n \rangle \langle x_4^n | q_{P_i(4)}^n \rangle \langle x_5^\Lambda | q_{P_i(5)}^\Lambda \rangle$$

$$= \frac{1}{N!} \text{Det} \begin{vmatrix}
\langle x_1^p|q_1^p\rangle T_{pp} & \langle x_1^p|q_2^p\rangle T_{pp} & \langle x_1^p|q_3^n\rangle T_{np} & \langle x_1^p|q_4^n\rangle T_{pn} & \langle x_1^p|q_5^\Lambda\rangle T_{p\Lambda} \\
\langle x_2^p|q_1^p\rangle T_{pp} & \langle x_2^p|q_2^p\rangle T_{pp} & \langle x_2^p|q_3^n\rangle T_{np} & \langle x_2^p|q_4^n\rangle T_{pn} & \langle x_2^p|q_5^\Lambda\rangle T_{p\Lambda} \\
\langle x_3^n|q_1^p\rangle T_{np} & \langle x_3^n|q_2^p\rangle T_{np} & \langle x_3^n|q_3^n\rangle T_{nn} & \langle x_3^n|q_4^n\rangle T_{nn} & \langle x_3^n|q_5^\Lambda\rangle T_{n\Lambda} \\
\langle x_4^n|q_1^p\rangle T_{np} & \langle x_4^n|q_2^p\rangle T_{np} & \langle x_4^n|q_3^n\rangle T_{nn} & \langle x_4^n|q_4^n\rangle T_{nn} & \langle x_4^n|q_5^\Lambda\rangle T_{n\Lambda} \\
\langle x_5^\Lambda|q_1^p\rangle T_{\Lambda p} & \langle x_5^\Lambda|q_2^p\rangle T_{\Lambda p} & \langle x_5^\Lambda|q_3^n\rangle T_{\Lambda n} & \langle x_5^\Lambda|q_4^n\rangle T_{\Lambda n} & \langle x_5^\Lambda|q_5^\Lambda\rangle T_{\Lambda\Lambda}
\end{vmatrix}$$

$$= \frac{1}{N!} \langle x_5^\Lambda|q_5^\Lambda\rangle \text{Det} \begin{vmatrix}
\langle x_1^p|q_1^p\rangle & \langle x_1^p|q_2^p\rangle & 0 & 0 \\
\langle x_2^p|q_1^p\rangle & \langle x_2^p|q_2^p\rangle & 0 & 0 \\
0 & 0 & \langle x_3^n|q_3^n\rangle & \langle x_3^n|q_4^n\rangle \\
0 & 0 & \langle x_4^n|q_3^n\rangle & \langle x_4^n|q_4^n\rangle
\end{vmatrix}$$

$$= \frac{1}{N!} \langle x_5^\Lambda|q_5^\Lambda\rangle \left[\langle x_1^p|q_1^p\rangle \langle x_2^p|q_2^p\rangle \text{Det}\begin{vmatrix} \langle x_3^n|q_3^n\rangle & \langle x_3^n|q_4^n\rangle \\ \langle x_4^n|q_3^n\rangle & \langle x_4^n|q_4^n\rangle \end{vmatrix} - \langle x_1^p|q_2^p\rangle \langle x_2^p|q_1^p\rangle \text{Det}\begin{vmatrix} \langle x_3^n|q_3^n\rangle & \langle x_3^n|q_4^n\rangle \\ \langle x_4^n|q_3^n\rangle & \langle x_4^n|q_4^n\rangle \end{vmatrix} \right]$$

$$= \frac{1}{N!} \langle x_5^\Lambda|q_5^\Lambda\rangle [\langle x_1^p|q_1^p\rangle \langle x_2^p|q_2^p\rangle (\langle x_3^n|q_3^n\rangle\langle x_4^n|q_4^n\rangle - \langle x_4^n|q_3^n\rangle\langle x_3^n|q_4^n\rangle) - \langle x_1^p|q_2^p\rangle \langle x_2^p|q_1^p\rangle (\langle x_3^n|q_3^n\rangle\langle x_4^n|q_4^n\rangle - \langle x_4^n|q_3^n\rangle\langle x_3^n|q_4^n\rangle)]$$

$$= \frac{1}{N!} \langle x_5^\Lambda|q_5^\Lambda\rangle [\langle x_3^n|q_3^n\rangle\langle x_4^n|q_4^n\rangle - \langle x_4^n|q_3^n\rangle\langle x_3^n|q_4^n\rangle][\langle x_1^p|q_1^p\rangle \langle x_2^p|q_2^p\rangle - \langle x_1^p|q_2^p\rangle \langle x_2^p|q_1^p\rangle].$$

$$(A.2)$$

As a result we obtain antisymmetrized many-body wave function of $^5_\Lambda$He.

In the following Eqs. A.3-A.6, we will explicitly denote the antisymmetrized many-body FMD state as $|Q_A\rangle$ to distinguish it from the non-antisymmetrized many-body state $|Q\rangle$. It is to be stressed that in the main text, the subscript 'A' for the antisymmetrized state is omitted. The expectation value formula (2.14) for a one-body operator $\hat{O}^{[1]}$ can be derived as follows

$$
\begin{aligned}
\frac{\langle Q_A|\, \hat{O}^{[1]}\, |Q_A\rangle}{\langle Q_A|\, Q_A\rangle} &= \frac{\langle Q|\, \hat{O}^{[1]}\, |Q_A\rangle}{\langle Q|\, Q_A\rangle} = \\
&= \frac{1}{\text{Det}|n|} \{\langle q_1| \otimes \ldots \otimes \langle q_N|\} \sum_k \hat{1} \otimes \ldots \otimes \hat{O}_k^{[1]} \otimes \ldots \otimes \hat{1} \\
&\{\frac{1}{N!} \sum_{P_i} \text{sgn}(P_i) |q_{P_i(1)}\rangle \otimes \ldots \otimes |q_{P_i(N)}\rangle\} = \\
&= \frac{1}{\text{Det}|n|} \sum_k \sum_{P_i} \text{sgn}(P_i) \langle q_1|\, q_{P_i(1)}\rangle \ldots \langle q_k|\, \hat{O}^{[1]}\, |q_{P_i(k)}\rangle \ldots \langle q_N|\, q_{P_i(N)}\rangle = \\
&= \frac{1}{\text{Det}|n|} \sum_k \sum_{P_i} \langle q_k|\, \hat{O}^{[1]}\, |q_{P_i(k)}\rangle \, \text{sgn}(P_i) \langle q_1|\, q_{P_i(1)}\rangle \ldots \\
&\ldots \langle q_{k-1}|\, q_{P_i(k-1)}\rangle \langle q_{k+1}|\, q_{P_i(k+1)}\rangle \ldots \langle q_N|\, q_{P_i(N)}\rangle = \\
&= \frac{1}{\text{Det}|n|} \sum_{kl} \langle q_k|\, \hat{O}^{[1]}\, |q_l\rangle (-)^{k+l} \sum_{P_i} \text{sgn}(P_i) \langle q_1|\, q_{P_i(1)}\rangle \ldots \\
&\ldots \langle q_{k-1}|\, q_{P_i(k-1)}\rangle \langle q_{k+1}|\, q_{P_i(k+1)}\rangle \ldots \langle q_n|\, q_{P_i(N)}\rangle = \\
&= \sum_{kl} \langle q_k|\, \hat{O}^{[1]}\, |q_l\rangle \frac{(-)^{k+l} \text{Det}|n_{k,l}|}{\text{Det}|n|} = \sum_{kl} \langle q_k|\, \hat{O}^{[1]}\, |q_l\rangle \, o_{lk},
\end{aligned}
\tag{A.3}
$$

where the element o_{lk} of the inverse matrix o is related to the single-particle overlap matrix n (2.13) as follows

$$
o_{lk} = \frac{(-)^{k+l} \text{Det}|n_{k,l}|}{\text{Det}|n|}.
\tag{A.4}
$$

The $\text{Det}|n_{k,l}|$ stand for the determinants of adjunct single-particle overlap matrices to n. The derivation of the expectation value of an arbitrary two-body operator $\hat{O}^{[2]}$ in Eqs. 2.14 is straightforward using the same procedure.

The overlap of two different antisymmetrized many-body FMD states $|Q_A^1\rangle$ and $|Q_A^2\rangle$ can be expressed as

$$
\begin{aligned}
\langle Q_A^1|\, Q_A^2\rangle = \langle Q^1|\, Q^2\rangle &= \frac{1}{N!} \sum_{P_i} \text{sgn}(P_i) \langle q_1^1, q_2^1, \cdots, q_N^1|\, q_{P_i(1)}^2, q_{P_i(2)}^2, \ldots, q_{P_i(N)}^2\rangle = \\
&= \frac{1}{N!} \text{Det}|\langle q_i^1|\, q_j^2\rangle| = \frac{1}{N!} \text{Det}|n^{12}|,
\end{aligned}
\tag{A.5}
$$

where $|q_i^1\rangle$ and $|q_j^2\rangle$ stand for the single-particle states (2.2) of the many-body state $|Q_A^1\rangle$ and $|Q_A^2\rangle$, respectively, and the $n^{12} = \langle q_i^1 | q_j^2 \rangle$ denotes their single-particle state overlap matrix (2.13).

The off-diagonal matrix elements of an arbitrary one-body operator $\hat{O}^{[1]}$ between two different FMD many-body states $|Q_A^1\rangle$ and $|Q_A^2\rangle$ can be expressed as

$$\langle Q_A^1 | \hat{O}^{[1]} | Q_A^2 \rangle = \sum_{kl} \langle q_k^1 | \hat{O}^{[1]} | q_l^2 \rangle o_{lk}^{12} \langle Q_A^1 | Q_A^2 \rangle$$

and in case of an arbitrary two-body operator $\hat{O}^{[2]}$ as

(A.6)

$$\langle Q_A^1 | \hat{O}^{[2]} | Q_A^2 \rangle = \sum_{klmn} \langle q_k^1, q_l^1 | \hat{O}^{[2]} | q_m^2, q_n^2 \rangle (o_{mk}^{12} o_{nl}^{12} - o_{nk}^{12} o_{ml}^{12}) \langle Q_A^1 | Q_A^2 \rangle .$$

Description of calculated observables

One-body densities

We use the definition of the total one-body density operator

$$\hat{\rho}(\boldsymbol{x}) = \sum_i \delta(\hat{\boldsymbol{x}_i} - \boldsymbol{x}) \tag{A.7}$$

which yields the one-body matrix elements in the form

$$\langle q_k | \delta(\hat{\boldsymbol{x}} - \boldsymbol{x}) | q_l \rangle = \exp\left(-\frac{(\boldsymbol{b}_k^* - \boldsymbol{x})^2}{2a_k^*}\right) \exp\left(-\frac{(\boldsymbol{b}_l - \boldsymbol{x})^2}{2a_l}\right) S_{kl} T_{kl}, \tag{A.8}$$

where a_l, $\boldsymbol{b}_l$ stand for the complex parameters of single-particle state $|q_l\rangle$ defined in (2.2). The S_{kl} and T_{kl} denote spin and isospin overlap matrix (2.13). The proton, neutron, nucleon, and Λ one-body density operators $\hat{\rho}_p(\boldsymbol{x})$, $\hat{\rho}_n(\boldsymbol{x})$, $\hat{\rho}_{nuc}(\boldsymbol{x})$, $\hat{\rho}_\Lambda(\boldsymbol{x})$ are given as follows

$$
\begin{aligned}
\hat{\rho}_p(\boldsymbol{x}) &= \sum_i \delta(\hat{\boldsymbol{x}_i} - \boldsymbol{x}) \hat{P}_i^p, & \hat{P}_i^p &= 2(\hat{\tau}_3 + 1/2)\hat{\tau}_3, \\
\hat{\rho}_n(\boldsymbol{x}) &= \sum_i \delta(\hat{\boldsymbol{x}_i} - \boldsymbol{x}) \hat{P}_i^n, & \hat{P}_i^n &= 2(\hat{\tau}_3 - 1/2)\hat{\tau}_3, \\
\hat{\rho}_{\text{nuc}}(\boldsymbol{x}) &= \sum_i \delta(\hat{\boldsymbol{x}_i} - \boldsymbol{x}) \hat{P}_i^{\text{nuc}}, & \hat{P}_i^{\text{nuc}} &= 2|\hat{\tau}_3|, \\
\hat{\rho}_\Lambda(\boldsymbol{x}) &= \sum_i \delta(\hat{\boldsymbol{x}_i} - \boldsymbol{x}) \hat{P}_i^\Lambda, & \hat{P}_i^\Lambda &= 2(1/2 - |\hat{\tau}_3|),
\end{aligned}
\tag{A.9}
$$

where the operator $\hat{\tau}_3$ is defined so that it returns the third projection of the isospin ξ_k of the single-particle state $|q_k\rangle$. The matrix elements yield the same analytical form as in (A.8) except that the selecting operators $\hat{P}_i^p$, $\hat{P}_i^n$, $\hat{P}_i^{\text{nuc}}$, and $\hat{P}_i^\Lambda$ are non-zero only for protons, neutrons, nucleons, and Λ, respectively.

Root mean-square radii

The operator of the total mean-square radius R_{T}^2 is defined in the form

$$
\begin{aligned}
\hat{R}_{\mathrm{T}}^2 &= \frac{1}{M} \sum_i m_i (\hat{\boldsymbol{x}}_{\boldsymbol{i}} - \hat{\boldsymbol{X}}_{\boldsymbol{cm}})^2 = \\
&= \sum_i \hat{\boldsymbol{x}}_{\boldsymbol{i}}^{\boldsymbol{2}} \frac{m_i(M - m_i)}{M} - \frac{2}{M} \sum_{i<j} \hat{\boldsymbol{x}}_{\boldsymbol{i}} \hat{\boldsymbol{x}}_{\boldsymbol{j}} m_i m_j,
\end{aligned}
\tag{A.10}
$$

where m_i denotes the mass of the i-th particle and the M stands for the total mass. The matrix elements of the one and two-body contributions to the $\hat{R}_{\mathrm{T}}^2$ are proportional to :

$$
\begin{aligned}
\langle q_k | \hat{\boldsymbol{x}}^{\boldsymbol{2}} | q_l \rangle &= (3\alpha_{kl} + \boldsymbol{\rho}_{\boldsymbol{kl}}^{\boldsymbol{2}}) n_{kl}, \quad \alpha_{kl} = \frac{a_k^* a_l}{a_k^* + a_l}, \quad \boldsymbol{\rho}_{\boldsymbol{kl}} = \frac{a_l \boldsymbol{b}_{\boldsymbol{k}}^{\boldsymbol{*}} + a_k^* \boldsymbol{b}_{\boldsymbol{l}}}{a_k^* + a_l}, \\
\langle q_k, q_l | \hat{\boldsymbol{x}} \otimes \hat{\boldsymbol{x}} | q_m, q_n \rangle &= (\boldsymbol{\rho}_{\boldsymbol{km}} \cdot \boldsymbol{\rho}_{\boldsymbol{ln}}) n_{km} n_{ln},
\end{aligned}
\tag{A.11}
$$

where n_{kl}, n_{km}, and n_{ln} are elements of the single-particle state overlap matrix (2.13). The operators of the proton, neutron, nucleon and Λ mass mean-square radii denoted as $\hat{R}_p^2$, $\hat{R}_n^2$, $\hat{R}_{\mathrm{nuc}}^2$, and $\hat{R}_\Lambda^2$ are defined as $R_x^2(x = p, n, \mathrm{nuc}, \Lambda)$

$$
\begin{aligned}
\hat{R}_x^2 &= \frac{1}{M_x} \sum_i \hat{P}_i^x m_i (\hat{\boldsymbol{x}}_{\boldsymbol{i}} - \hat{\boldsymbol{X}}_{\boldsymbol{cm}})^2 = \\
&= \sum_i \hat{\boldsymbol{x}}_{\boldsymbol{i}}^{\boldsymbol{2}} \left(\frac{m_i(M - 2m_i)}{M M_x} \hat{P}_i^x + \frac{m_i^2}{M^2} \right) + \sum_{i<j} \hat{\boldsymbol{x}}_{\boldsymbol{i}} \hat{\boldsymbol{x}}_{\boldsymbol{j}} \left(\frac{2M_x - (\hat{P}_i^x + \hat{P}_j^x)M}{M^2 M_x} \right) m_i m_j.
\end{aligned}
\tag{A.12}
$$

Where M_x is the total mass of the relevant kind of particles defined by the index x.

In our hypernuclear calculations, we calculate the mean-square radius of the nuclear core R_{core}^2 which is defined as the nucleon mean-square radius with respect to the nucleon center of mass

$$
\hat{\boldsymbol{X}}_{\mathbf{nuc}} = \frac{1}{M_{\mathrm{nuc}}} \sum_i m_i \hat{\boldsymbol{x}}_{\boldsymbol{i}} \hat{P}_i^{\mathrm{nuc}},
\tag{A.13}
$$

where M_{nuc} is the total mass of nucleons in the hypernuclear system. The $\hat{P}_i^{\mathrm{nuc}}$ is the selecting operator defined in Eqs. A.9. The operator $\hat{R}_{\mathrm{core}}^2$ has the form

$$
\begin{aligned}
\hat{R}_{\mathrm{core}}^2 &= \frac{1}{M_{\mathrm{nuc}}} \sum_i m_i \hat{P}_i^{\mathrm{nuc}} (\hat{\boldsymbol{x}}_{\boldsymbol{i}} - \hat{\boldsymbol{X}}_{\mathbf{nuc}})^2 = \\
&= \sum_i \hat{\boldsymbol{x}}_{\boldsymbol{i}}^{\boldsymbol{2}} \frac{m_i(M_{\mathrm{nuc}} - m_i)}{M_{\mathrm{nuc}}^2} \hat{P}_i^{nuc} - \frac{2}{M_{\mathrm{nuc}}^2} \sum_{i<j} \hat{\boldsymbol{x}}_{\boldsymbol{i}} \hat{\boldsymbol{x}}_{\boldsymbol{j}} m_i m_j \hat{P}_i^{nuc} \hat{P}_j^{nuc}.
\end{aligned}
\tag{A.14}
$$

We implement the definition of the charge rms radius R_{charge} as

$$R_{charge} = \sqrt{R_p^2 + \left\langle r_p^2 \right\rangle + \frac{N}{Z} \left\langle r_n^2 \right\rangle}, \tag{A.15}$$

where R_p^2 denotes calculated proton mean-square radius. The $\left\langle r_p^2 \right\rangle$ and $\left\langle r_n^2 \right\rangle$ stand for the experimentally measured values Table. 4.1 of the charge mean-square radii of the proton and neutron, respectively.

Appendix B

Analytical derivatives

The algorithms L-BFGS-B [71] and SQP [44] used in this work to minimize the expectation value of the Hamiltonian $\hat{H}$ (2.18) denoted as $\mathscr{H}$ require during the minimization process the evaluation of the gradient $\frac{\partial \mathscr{H}}{\partial \boldsymbol{p}}$ for a set of variational parameters. Here, $\boldsymbol{p}$ denotes the array of these single-particle state parameters (2.2). Its size may become quite large – for an N-body system, there are overall $12 \times N$ real parameters (six complex per each single-particle state (2.2)), and the same number of derivatives of $\mathscr{H}$ is to be calculated.

If one tries to evaluate each element of the gradient $\frac{\partial \mathscr{H}}{\partial \boldsymbol{p}}$ numerically, the approximate values of the derivatives could cause significant errors during the minimization and the aforementioned algorithms fail to converge. On the other hand, a sufficient accuracy of the numerical derivatives is connected with increased computational complexity, which makes the FMD calculations impracticable. Consequently, we must evaluate all derivatives analytically. In the following we give the brief description of these calculations which were partially introduced already in ref. [34].

In this Appendix we will denote the i-th complex parametr of the d-th single-particle state $|q_d\rangle$ as q_μ, where $\mu = (d, i)$. The expectation value of the Hamiltonian $\mathscr{H}$ is a function of the complex parameters q_μ (q_μ^*) of the $|q_d\rangle$ ($\langle q_d|$) vectors. The derivative of $\mathscr{H}$ with respect to the real part of the complex parameter q_μ can be expressed as

$$
\begin{aligned}
\frac{\partial \mathscr{H}}{\partial \operatorname{Re} q_\mu} &= \frac{\partial \mathscr{H}}{\partial q_\mu} \frac{\partial p}{\partial \operatorname{Re} q_\mu} + \frac{\partial \mathscr{H}}{\partial q_\mu^*} \frac{\partial q_\mu^*}{\partial \operatorname{Re} q_\mu} = \frac{\partial \mathscr{H}}{\partial q_\mu} + \frac{\partial \mathscr{H}}{\partial q_\mu^*} = \left(\frac{\partial \mathscr{H}}{\partial q_\mu^*} \right)^* + \frac{\partial \mathscr{H}}{\partial q_\mu^*} = \\
&= \operatorname{Re} \frac{\partial \mathscr{H}}{\partial q_\mu^*} - \mathrm{i} \operatorname{Im} \frac{\partial \mathscr{H}}{\partial q_\mu^*} + \operatorname{Re} \frac{\partial \mathscr{H}}{\partial q_\mu^*} + \mathrm{i} \operatorname{Im} \frac{\partial \mathscr{H}}{\partial q_\mu^*} = 2\operatorname{Re} \frac{\partial \mathscr{H}}{\partial q_\mu^*},
\end{aligned} \tag{B.1}
$$

and with respect to the imaginary part of q_μ as

$$\frac{\partial \mathcal{H}}{\partial \mathrm{Im}\, q_\mu} = \frac{\partial \mathcal{H}}{\partial q_\mu}\frac{\partial q_\mu}{\partial \mathrm{Im}\, q_\mu} + \frac{\partial \mathcal{H}}{\partial q_\mu^*}\frac{\partial q_\mu^*}{\partial \mathrm{Im}\, q_\mu} = \mathrm{i}\frac{\partial \mathcal{H}}{\partial q_\mu} - \mathrm{i}\frac{\partial \mathcal{H}}{\partial q_\mu^*} = \mathrm{i}\left(\frac{\partial \mathcal{H}}{\partial q_\mu^*}\right)^* - \mathrm{i}\frac{\partial \mathcal{H}}{\partial q_\mu^*} =$$

$$= \mathrm{i}\mathrm{Re}\frac{\partial \mathcal{H}}{\partial q_\mu^*} + \mathrm{Im}\frac{\partial \mathcal{H}}{\partial q_\mu^*} - \mathrm{i}\mathrm{Re}\frac{\partial \mathcal{H}}{\partial q_\mu^*} + \mathrm{Im}\frac{\partial \mathcal{H}}{\partial q_\mu^*} = 2\mathrm{Im}\frac{\partial \mathcal{H}}{\partial q_\mu^*},$$

(B.2)

where we take into account that the expectation value $\mathcal{H}$ is a real function. Consequently, the derivatives with respect to a real or imaginary part of q_μ can be both obtained by calculating the complex derivative of $\mathcal{H}$ with respect to complex conjugate parameters q_μ^* which simplifies their evaluation.

The derivatives of the one-body contributions $\mathcal{H}^{[1]}$ to the expectation value $\mathcal{H}$ with respect to q_μ^* can be analytically expressed as

$$\frac{\partial \mathcal{H}^{[1]}}{\partial q_\mu^*} = \frac{\partial}{\partial q_\mu^*}\left(\sum_{kl}\langle q_k|\,\hat{H}^{[1]}\,|q_l\rangle\, o_{lk}\right) =$$

$$= \sum_l \frac{\partial}{\partial q_\mu^*}\langle q_d|\,\hat{H}^{[1]}\,|q_l\rangle\, o_{ld} + \sum_{kl}\langle q_k|\,\hat{H}^{[1]}\,|q_l\rangle\,\frac{\partial}{\partial q_\mu^*} o_{lk},$$

(B.3)

where we take into account the analytical expression for $\mathcal{H}^{[1]}$ given in Eq. (2.14). The o_{ld} (o_{lk}) stands for the element of the inverse matrix o to the single-particle overlap matrix n (2.13). The derivative of o_{lk} with respect to q_μ^* can be obtained by multiplying n and $o = n^{-1}$

$$\sum_r n_{pr} o_{rk} = \sum_r \langle q_p|\, q_r\rangle\, o_{rk} = \delta_{pk},$$

(B.4)

applying derivative with respect to q_μ^*

$$\sum_r \frac{\partial}{\partial q_\mu^*}\langle q_p|\, q_r\rangle\, o_{rk} + \sum_r \langle q_p|\, q_r\rangle\,\frac{\partial}{\partial q_\mu^*} o_{rk} = 0,$$

(B.5)

multiplying by o_{lp} and sum over p

$$\sum_p o_{lp}\sum_r \frac{\partial}{\partial q_\mu^*}\langle q_p|\, q_r\rangle\, o_{rk} + \sum_p o_{lp}\sum_r \langle q_p|\, q_r\rangle\,\frac{\partial}{\partial q_\mu^*} o_{rk} = 0,$$

$$\sum_p o_{lp}\sum_r \delta_{pd}\left(\frac{\partial}{\partial q_\mu^*}\langle q_d|\, q_r\rangle\right) o_{rk} + \sum_r \underbrace{\sum_p o_{lp}\langle q_p|\, q_r\rangle}_{\delta_{lr}}\frac{\partial}{\partial q_\mu^*} o_{rk} = 0.$$

(B.6)

This yields the expression for the derivative of the o_{lk} with respect to q_μ^*

$$\frac{\partial}{\partial q_\mu^*} o_{lk} = -o_{ld} \sum_r \left(\frac{\partial}{\partial q_\mu^*} \langle q_d | q_r \rangle \right) o_{rk}. \tag{B.7}$$

We obtain the final expression for the derivatives of the one-body contributions $\mathscr{H}^{[1]}$ to the expectation value $\mathscr{H}$ with respect to q_μ^* by substituting (B.7) into (B.3)

$$\frac{\partial \mathscr{H}^{[1]}}{\partial q_\mu^*} = \sum_l \left[\frac{\partial}{\partial q_\mu^*} \langle q_d | \hat{H}^{[1]} | q_l \rangle - \sum_{kr} \left(\frac{\partial}{\partial q_\mu^*} \langle q_d | q_r \rangle \right) o_{rk} \langle q_k | \hat{H}^{[1]} | q_l \rangle \right] o_{ld}. \tag{B.8}$$

The derivatives of the two-body contributions $\mathscr{H}^{[2]}$ to the expectation value $\mathscr{H}$ with respect to q_μ^* can be analytically expressed as

$$\begin{aligned}
\frac{\partial \mathscr{H}^{[2]}}{\partial q_\mu^*} &= \frac{\partial}{\partial q_\mu^*} \left(\sum_{klmn} \langle q_k, q_l | \hat{H}^{[2]} | q_m, q_n \rangle (o_{mk} o_{nl} - o_{nk} o_{ml}) \right) = \\
&= 2 \sum_{lnm} \frac{\partial}{\partial q_\mu^*} \langle q_d, q_l | \hat{H}^{[2]} | q_m, q_n \rangle (o_{md} o_{nl} - o_{nd} o_{ml}) + \\
&+ \sum_{klmn} \langle q_k, q_l | \hat{H}^{[2]} | q_m, q_n \rangle \left(\frac{\partial}{\partial q_\mu^*} o_{mk} o_{nl} + o_{mk} \frac{\partial}{\partial q_\mu^*} o_{nl} - \frac{\partial}{\partial q_\mu^*} o_{nk} o_{ml} - o_{nk} \frac{\partial}{\partial q_\mu^*} o_{ml} \right) = \\
&= 2 \sum_{lnm} \left[\frac{\partial}{\partial q_\mu^*} \langle q_d, q_l | \hat{H}^{[2]} | q_m, q_n \rangle - \sum_{kr} \left(\frac{\partial}{\partial q_\mu^*} \langle q_m | q_r \rangle \right) o_{rk} \langle q_k, q_l | \hat{H}^{[2]} | q_m, q_n \rangle \right] \\
&\quad (o_{md} o_{nl} - o_{nd} o_{ml}),
\end{aligned} \tag{B.9}$$

where we again take into account the analytical expression of $\mathscr{H}^{[2]}$ given in Eqs. (2.14) and we apply (B.7) for the derivative of the inverse overlap matrix elements.

To conclude, the evaluation of analytical derivatives using Eqs. B.8 and Eqs. B.9 can be done quite effectively. The overall calculation is transformed to the sums over one and two-body matrix elements, their derivatives, elements of inverse single-particle overlap matrix o, and derivatives of single-particle overlap matrix n, which makes the calculation computationally manageable.

Appendix C

Parameters and the operator form of the V_{NN} and $V_{\Lambda N}$ potentials

The effective two-body V_{NN} and $V_{\Lambda N}$ potentials used in this work may consist of the following operator terms

$$
\begin{aligned}
\hat{V}_c(\hat{T}_p) &= \hat{V}(\hat{\boldsymbol{x}}_{\mathbf{1}} - \hat{\boldsymbol{x}}_{\mathbf{2}}), \\
\hat{V}_c^\sigma(\hat{T}_p^\sigma) &= \hat{V}(\hat{\boldsymbol{x}}_{\mathbf{1}} - \hat{\boldsymbol{x}}_{\mathbf{2}})(\hat{\boldsymbol{\sigma}}_{\mathbf{1}}.\hat{\boldsymbol{\sigma}}_{\mathbf{2}}), \\
\hat{V}_c^\tau(\hat{T}_p^\tau) &= \hat{V}(\hat{\boldsymbol{x}}_{\mathbf{1}} - \hat{\boldsymbol{x}}_{\mathbf{2}})(\hat{\boldsymbol{\tau}}_{\mathbf{1}}.\hat{\boldsymbol{\tau}}_{\mathbf{2}}), \\
\hat{V}_c^{\sigma\tau}(\hat{T}_p^{\tau\sigma}) &= \hat{V}(\hat{\boldsymbol{x}}_{\mathbf{1}} - \hat{\boldsymbol{x}}_{\mathbf{2}})(\hat{\boldsymbol{\sigma}}_{\mathbf{1}}.\hat{\boldsymbol{\sigma}}_{\mathbf{2}})(\hat{\boldsymbol{\tau}}_{\mathbf{1}}.\hat{\boldsymbol{\tau}}_{\mathbf{2}}), \\
\hat{V}_c^\pi &= \hat{V}(\hat{\boldsymbol{x}}_{\mathbf{1}} - \hat{\boldsymbol{x}}_{\mathbf{2}})\hat{\Pi}, \\
\hat{V}_c^{\pi\sigma} &= \hat{V}(\hat{\boldsymbol{x}}_{\mathbf{1}} - \hat{\boldsymbol{x}}_{\mathbf{2}})\hat{\Pi}(\hat{\boldsymbol{\sigma}}_{\mathbf{1}}.\hat{\boldsymbol{\sigma}}_{\mathbf{2}}), \\
\hat{T}_r &= \frac{\overleftarrow{\partial}}{\partial|\hat{\boldsymbol{x}}_{\mathbf{1}}-\hat{\boldsymbol{x}}_{\mathbf{2}}|}(\hat{\boldsymbol{x}}_{\mathbf{1}} - \hat{\boldsymbol{x}}_{\mathbf{2}})^2\hat{V}(\hat{\boldsymbol{x}}_{\mathbf{1}} - \hat{\boldsymbol{x}}_{\mathbf{2}})\frac{\overrightarrow{\partial}}{\partial|\hat{\boldsymbol{x}}_{\mathbf{1}}-\hat{\boldsymbol{x}}_{\mathbf{2}}|}, \\
\hat{T}_{\vec{r}} &= \frac{\overleftarrow{\partial}}{\partial(\hat{\boldsymbol{x}}_{\mathbf{1}}-\hat{\boldsymbol{x}}_{\mathbf{2}})}\hat{V}(\hat{\boldsymbol{x}}_{\mathbf{1}} - \hat{\boldsymbol{x}}_{\mathbf{2}})\frac{\overrightarrow{\partial}}{\partial(\hat{\boldsymbol{x}}_{\mathbf{1}}-\hat{\boldsymbol{x}}_{\mathbf{2}})}, \\
\hat{T}_r^\sigma &= \frac{\overleftarrow{\partial}}{\partial|\hat{\boldsymbol{x}}_{\mathbf{1}}-\hat{\boldsymbol{x}}_{\mathbf{2}}|}(\hat{\boldsymbol{x}}_{\mathbf{1}} - \hat{\boldsymbol{x}}_{\mathbf{2}})^2\hat{V}(\hat{\boldsymbol{x}}_{\mathbf{1}} - \hat{\boldsymbol{x}}_{\mathbf{2}})\frac{\overrightarrow{\partial}}{\partial|\hat{\boldsymbol{x}}_{\mathbf{1}}-\hat{\boldsymbol{x}}_{\mathbf{2}}|}(\hat{\boldsymbol{\sigma}}_{\mathbf{1}}.\hat{\boldsymbol{\sigma}}_{\mathbf{2}}), \\
\hat{T}_{\vec{r}}^\sigma &= \frac{\overleftarrow{\partial}}{\partial(\hat{\boldsymbol{x}}_{\mathbf{1}}-\hat{\boldsymbol{x}}_{\mathbf{2}})}\hat{V}(\hat{\boldsymbol{x}}_{\mathbf{1}} - \hat{\boldsymbol{x}}_{\mathbf{2}})\frac{\overrightarrow{\partial}}{\partial(\hat{\boldsymbol{x}}_{\mathbf{1}}-\hat{\boldsymbol{x}}_{\mathbf{2}})}(\hat{\boldsymbol{\sigma}}_{\mathbf{1}}.\hat{\boldsymbol{\sigma}}_{\mathbf{2}}), \\
\hat{T}_r^\tau &= \frac{\overleftarrow{\partial}}{\partial|\hat{\boldsymbol{x}}_{\mathbf{1}}-\hat{\boldsymbol{x}}_{\mathbf{2}}|}(\hat{\boldsymbol{x}}_{\mathbf{1}} - \hat{\boldsymbol{x}}_{\mathbf{2}})^2\hat{V}(\hat{\boldsymbol{x}}_{\mathbf{1}} - \hat{\boldsymbol{x}}_{\mathbf{2}})\frac{\overrightarrow{\partial}}{\partial|\hat{\boldsymbol{x}}_{\mathbf{1}}-\hat{\boldsymbol{x}}_{\mathbf{2}}|}(\hat{\boldsymbol{\tau}}_{\mathbf{1}}.\hat{\boldsymbol{\tau}}_{\mathbf{2}}), \\
\hat{T}_{\vec{r}}^\tau &= \frac{\overleftarrow{\partial}}{\partial(\hat{\boldsymbol{x}}_{\mathbf{1}}-\hat{\boldsymbol{x}}_{\mathbf{2}})}\hat{V}(\hat{\boldsymbol{x}}_{\mathbf{1}} - \hat{\boldsymbol{x}}_{\mathbf{2}})\frac{\overrightarrow{\partial}}{\partial(\hat{\boldsymbol{x}}_{\mathbf{1}}-\hat{\boldsymbol{x}}_{\mathbf{2}})}(\hat{\boldsymbol{\tau}}_{\mathbf{1}}.\hat{\boldsymbol{\tau}}_{\mathbf{2}}), \\
\hat{T}_r^{\tau\sigma} &= \frac{\overleftarrow{\partial}}{\partial|\hat{\boldsymbol{x}}_{\mathbf{1}}-\hat{\boldsymbol{x}}_{\mathbf{2}}|}(\hat{\boldsymbol{x}}_{\mathbf{1}} - \hat{\boldsymbol{x}}_{\mathbf{2}})^2\hat{V}(\hat{\boldsymbol{x}}_{\mathbf{1}} - \hat{\boldsymbol{x}}_{\mathbf{2}})\frac{\overrightarrow{\partial}}{\partial|\hat{\boldsymbol{x}}_{\mathbf{1}}-\hat{\boldsymbol{x}}_{\mathbf{2}}|}(\hat{\boldsymbol{\sigma}}_{\mathbf{1}}.\hat{\boldsymbol{\sigma}}_{\mathbf{2}})(\hat{\boldsymbol{\tau}}_{\mathbf{1}}.\hat{\boldsymbol{\tau}}_{\mathbf{2}}), \\
\hat{T}_{\vec{r}}^{\tau\sigma} &= \frac{\overleftarrow{\partial}}{\partial(\hat{\boldsymbol{x}}_{\mathbf{1}}-\hat{\boldsymbol{x}}_{\mathbf{2}})}\hat{V}(\hat{\boldsymbol{x}}_{\mathbf{1}} - \hat{\boldsymbol{x}}_{\mathbf{2}})\frac{\overrightarrow{\partial}}{\partial(\hat{\boldsymbol{x}}_{\mathbf{1}}-\hat{\boldsymbol{x}}_{\mathbf{2}})}(\hat{\boldsymbol{\sigma}}_{\mathbf{1}}.\hat{\boldsymbol{\sigma}}_{\mathbf{2}})(\hat{\boldsymbol{\tau}}_{\mathbf{1}}.\hat{\boldsymbol{\tau}}_{\mathbf{2}}),
\end{aligned}
\tag{C.1}
$$

where $\hat{\boldsymbol{\sigma}} = (\sigma^{(1)}, \sigma^{(2)}, \sigma^{(3)})$ ($\hat{\boldsymbol{\tau}} = (\sigma^{(1)}, \sigma^{(2)}, \sigma^{(3)})$) is the vector of the Pauli matrices $\sigma^{(i)}$ acting in spin (isospin) space and $\hat{T}_i$ denote UCOM transformed potentials. The $\hat{V}(\hat{\boldsymbol{x}}_{\mathbf{1}} - \hat{\boldsymbol{x}}_{\mathbf{2}})$ which describes the radial dependence of each operator term in (C.1) is

expressed for both V_{NN} and $V_{\Lambda N}$ potentials as a sum of Gaussians

$$\hat{V}(\hat{\boldsymbol{x}}_{\mathbf{1}} - \hat{\boldsymbol{x}}_{\mathbf{2}}) = \sum_i \gamma_i \exp\left(-\frac{(\hat{\boldsymbol{x}}_{\mathbf{1}} - \hat{\boldsymbol{x}}_{\mathbf{2}})^2}{2\kappa_i}\right), \tag{C.2}$$

where the parameters γ_i and κ_i determining the shape of $\hat{V}$ differ for each particular operator term in (C.1). The Gaussian form significantly simplifies the analytical calculation of matrix elements which are the essential part of the variational method.

The analytical calculations of the two-body matrix elements $\langle q_k; q_l | \hat{V}(\hat{T}) | q_m; q_n \rangle$ of individual operator terms (C.1) in the FMD basis for $\hat{V}(\hat{\boldsymbol{x}}_{\mathbf{1}} - \hat{\boldsymbol{x}}_{\mathbf{2}})$ expanded as the sum of Gaussians (C.2) were already performed in Ref. [34].

a) V_{NN} potentials

Volkov V2 potential

The effective Volkov V2 potential [66] is originally given in the form

$$\hat{V}_{NN} = \hat{V}(\hat{\boldsymbol{x}}_{\mathbf{1}} - \hat{\boldsymbol{x}}_{\mathbf{2}})(1 - M + M\hat{P}^x),$$

$$\hat{V}(\hat{\boldsymbol{x}}_{\mathbf{1}} - \hat{\boldsymbol{x}}_{\mathbf{2}}) = V_a \exp\left(-\frac{(\hat{\boldsymbol{x}}_{\mathbf{1}} - \hat{\boldsymbol{x}}_{\mathbf{2}})^2}{\alpha^2}\right) + V_r \exp\left(-\frac{(\hat{\boldsymbol{x}}_{\mathbf{1}} - \hat{\boldsymbol{x}}_{\mathbf{2}})^2}{\rho^2}\right),$$

$$V_a = -60.65 \text{ MeV}, \quad \alpha = 1.80 \text{ fm},$$

$$V_r = 61.14 \text{ MeV}, \quad \rho = 1.01 \text{ fm}, \tag{C.3}$$

where M denotes the Majorana parameter and $\hat{P}^x$ stands for the Majorana exchange operator. In our calculations, we replace the $\hat{P}^x$ by the product of the spin and isospin exchange operators $\hat{P}^x = -\hat{P}^\sigma \hat{P}^\tau$ and we apply the V_{NN} potential in the form

$$\hat{V}_{NN} = \left(1 - M - \frac{M}{4}\right)\hat{V}(\hat{\boldsymbol{x}}_{\mathbf{1}} - \hat{\boldsymbol{x}}_{\mathbf{2}}) - \frac{M}{4}\hat{V}(\hat{\boldsymbol{x}}_{\mathbf{1}} - \hat{\boldsymbol{x}}_{\mathbf{2}})(\hat{\boldsymbol{\sigma}}_{\mathbf{1}}.\hat{\boldsymbol{\sigma}}_{\mathbf{2}})-$$

$$- \frac{M}{4}\hat{V}(\hat{\boldsymbol{x}}_{\mathbf{1}} - \hat{\boldsymbol{x}}_{\mathbf{2}})(\hat{\boldsymbol{\tau}}_{\mathbf{1}}.\hat{\boldsymbol{\tau}}_{\mathbf{2}}) - \frac{M}{4}\hat{V}(\hat{\boldsymbol{x}}_{\mathbf{1}} - \hat{\boldsymbol{x}}_{\mathbf{2}})(\hat{\boldsymbol{\sigma}}_{\mathbf{1}}.\hat{\boldsymbol{\sigma}}_{\mathbf{2}})(\hat{\boldsymbol{\tau}}_{\mathbf{1}}.\hat{\boldsymbol{\tau}}_{\mathbf{2}}) = \tag{C.4}$$

$$= \hat{V}_c + \hat{V}_c^\sigma + \hat{V}_c^\tau + \hat{V}_c^{\sigma\tau}.$$

We use the Volkov V2 potential with the Majorana parameter $M = 0.0$ and $M = 0.6$. The potential parameters γ_i and κ_i in these cases are given in Table C.1

Malfliet-Tjon V5

The UCOM transformed Malfliet-Tjon V5 potential [35] has the following operator
structure

$$\hat{V}_{NN} = \hat{T}_p + \hat{T}_r + \hat{T}_{\tilde{r}} + \hat{V}_c, \tag{C.5}$$

where the individual operator contributions to the potential are defined in (C.1).
The Gaussian parameters γ_i and κ_i of each operator term were determined in [34]
and are given in Table C.2.

Afnan-Tang S3M

The UCOM transformed Afnan-Tang S3M potential [35] distinguishes between the
individual spin and isospin channels, therefore, its operator structure is more com-
plex than in the previous cases

$$\hat{V}_{NN} = \hat{T}_p + \hat{T}_r + \hat{T}_{\tilde{r}} + \hat{V}_c + \hat{T}_p^\sigma + \hat{T}_r^\sigma + \hat{T}_{\tilde{r}}^\sigma + \hat{V}_c^\sigma + \hat{T}_p^\tau + \hat{T}_r^\tau + \hat{T}_{\tilde{r}}^\tau + \hat{V}_c^\tau + \hat{T}_p^{\sigma\tau} + \hat{T}_r^{\sigma\tau} + \hat{T}_{\tilde{r}}^{\sigma\tau} + \hat{V}_c^{\sigma\tau}, \tag{C.6}$$

where the definition of the individual operator terms is given in (C.1). The Gaussian
parameters γ_i and κ_i of each operator term were also determined in [34] and are given
in Table C.3.

b) YNG $V_{\Lambda N}$ potentials

For the description of the ΛN interaction we apply YNG Jülich potentials YNG-JA
and YNG-JB [21], and YNG Nijmegen potentials YNG-ND, YNG-NF, and YNG-NS
[21]. They are given in the spin-parity ^1E, ^3E, ^1O, and ^3O channels, where 1 (3)
denotes the spin-singlet (triplet) and E (O) stands for even (odd) parity. The $V_{\Lambda N}$
potential is represented in each channel by its parameters in a three-range Gaussian
form

$$\hat{V}_{\Lambda N} = \sum_i^3 (a_i + b_i k_{\mathrm{F}} + c_i k_{\mathrm{F}}^2) \exp\left(-\frac{(\hat{\boldsymbol{x}}_{\boldsymbol{\Lambda}} - \hat{\boldsymbol{x}}_{\boldsymbol{N}})^2}{\beta_i^2}\right), \tag{C.7}$$

where a_i, b_i, c_i, and β_i determined to fit the corresponding G-matrix [21] are given in
Table C.4 A typical property of the YNG potentials is their dependence on the Fermi
momentum k_{F} which characterizes the nuclear medium surrounding the Λ hyperon.
Therefore, k_{F} has to be determined for each hypernuclear system separately. We de-
scribe individual spin-parity channels using the parity projection operator $\hat{P}^\pi$ (2.21)
and the spin-singlet (spin-triplet) projection operator $\hat{P}^1$ ($\hat{P}^3$)

$$\hat{P}^1 = \frac{1}{4}(1 - \hat{\boldsymbol{\sigma}}_{\boldsymbol{1}} . \hat{\boldsymbol{\sigma}}_{\boldsymbol{2}}), \qquad \hat{P}^3 = \frac{1}{4}(3 + \hat{\boldsymbol{\sigma}}_{\boldsymbol{1}} . \hat{\boldsymbol{\sigma}}_{\boldsymbol{2}}). \tag{C.8}$$

The YNG $V_{\Lambda N}$ potential is then expressed as the sum over all spin-channel contributions ^1E, ^3E, ^1O, and ^3O

$$\hat{V}_{\Lambda N} = \hat{V}_{1E}\hat{P}^1\hat{P}^+ + \hat{V}_{3E}\hat{P}^3\hat{P}^+ + \hat{V}_{1O}\hat{P}^1\hat{P}^- + \hat{V}_{3O}\hat{P}^3\hat{P}^- \tag{C.9}$$

that yields the following operator structure

$$
\begin{aligned}
\hat{V}_{\Lambda N} =& \frac{1}{8}(\hat{V}_{1E} + 3\hat{V}_{3E} + \hat{V}_{1O} + 3\hat{V}_{3O}) + \frac{1}{8}(\hat{V}_{1E} + 3\hat{V}_{3E} - \hat{V}_{1O} - 3\hat{V}_{3O})\hat{\Pi} + \\
&+ \frac{1}{8}(-\hat{V}_{1E} + \hat{V}_{3E} - \hat{V}_{1O} + \hat{V}_{3O})\boldsymbol{\hat{\sigma}}_1.\boldsymbol{\hat{\sigma}}_2 + \frac{1}{8}(-\hat{V}_{1E} + \hat{V}_{3E} + \hat{V}_{1O} - \hat{V}_{3O})\hat{\Pi}\boldsymbol{\hat{\sigma}}_1.\boldsymbol{\hat{\sigma}}_2 = \\
=& \hat{V}^c + \hat{V}^\pi\hat{\Pi} + \hat{V}^\sigma\boldsymbol{\hat{\sigma}}_1.\boldsymbol{\hat{\sigma}}_2 + \hat{V}^{\pi\sigma}\hat{\Pi}\boldsymbol{\hat{\sigma}}_1.\boldsymbol{\hat{\sigma}}_2.
\end{aligned}
\tag{C.10}
$$

c) Coulomb interaction

In this work, we implement the Coulomb potential acting between protons in a form

$$\hat{V}_C = \frac{1}{4\pi\epsilon_0}\frac{e^2}{|\boldsymbol{\hat{x}_1} - \boldsymbol{\hat{x}_2}|} = \frac{\alpha}{|\boldsymbol{\hat{x}_1} - \boldsymbol{\hat{x}_2}|}, \tag{C.11}$$

where α is the fine structure constant. The two-body matrix elements of the Coulomb potential in the FMD basis can be expressed analytically [46] as

$$
\begin{aligned}
\langle q_k; q_l| \hat{V}_C |q_m; q_n\rangle &= \alpha \langle q_k; q_l| \frac{1}{|\boldsymbol{\hat{x}_1} - \boldsymbol{\hat{x}_2}|} |q_m; q_n\rangle = \\
&= \frac{\alpha}{\sqrt{\boldsymbol{\rho}_{klmn}^2}}\mathrm{erf}\left(\sqrt{\frac{\boldsymbol{\rho}_{klmn}^2}{2\alpha_{klmn}}}\right) n_{km}n_{ln},
\end{aligned}
$$

$$
\begin{aligned}
\alpha_{klmn} &= \alpha_{km} + \alpha_{ln}, & \alpha_{km} &= \frac{a_k^* a_m}{a_k^* + a_m}, & \alpha_{ln} &= \frac{a_l^* a_n}{a_l^* + a_n}, \\
\boldsymbol{\rho}_{klmn} &= \boldsymbol{\rho}_{km} - \boldsymbol{\rho}_{ln}, & \boldsymbol{\rho}_{km} &= \frac{a_m\boldsymbol{b_k^*} + a_k^*\boldsymbol{b_m}}{a_k^* + a_m}, & \boldsymbol{\rho}_{ln} &= \frac{a_n\boldsymbol{b_l^*} + a_l^*\boldsymbol{b_n}}{a_l^* + a_n},
\end{aligned}
\tag{C.12}
$$

where $\mathrm{erf}()$ stands for the error function and a_k, $\boldsymbol{b_k}$, a_l, $\boldsymbol{b_l}$, a_m, $\boldsymbol{b_m}$, a_n, and $\boldsymbol{b_n}$ are the parameters of the single-particle states $|q_k\rangle$, $|q_l\rangle$, $|q_m\rangle$, and $|q_n\rangle$, respectively (2.2). The n_{km} and n_{ln} denote the elements of the single-particle state overlap matrix (2.13).

However, the analytically expressed two-body matrix elements $\langle q_k; q_l| \hat{V}_C |q_m; q_n\rangle$ are numerically problematic when the numerator and denominator in the expression $\mathrm{erf}\left(\sqrt{z}\right)/\sqrt{z}$ are evaluated separately [72]. Therefore, we substitute this term in the

vicinity of z=0 by the Padé approximant of order [5/6]

$$\frac{1}{\sqrt{\rho_{klmn}^2}}\mathrm{erf}\left(\sqrt{\frac{\rho_{klmn}^2}{2\alpha_{klmn}}}\right) = \left[z = \frac{\rho_{klmn}^2}{2\alpha_{klmn}}\right] = 2\alpha_{klmn}\frac{\mathrm{erf}\left(\sqrt{z}\right)}{\sqrt{z}} =$$
$$= 2\alpha_{klmn}R_0^{5/6}(z), \tag{C.13}$$

where $R_0^{5/6}(z)$ denotes the Padé approximant of order [5/6] in the vicinity of z=0.

Tables of potential parameters

Table C.1: The parameters γ_i and κ_i determining the radial part (C.2) of each operator term (C.4) of the Volkov V2 V_{NN} potential [66]. We show the potential parameters calculated for the Volkov V2 potential with the Majorana parameter $M = 0.0$ and $M = 0.6$ that are used in this work.

M=0.0			M=0.6		
Term	γ_i [fm^{-1}]	κ_i [fm^2]	Term	γ_i [fm^{-1}]	κ_i [fm^2]
V_c	0.309841	0.51005	V_c	0.077460	0.51005
	-0.307358	1.62000		-0.076840	1.62000
			$V_c^\sigma, V_c^\tau, V_c^{\tau\sigma}$	-0.046476	0.51005
				0.046104	1.62000

Table C.2: The parameters γ_i and κ_i [34] determining the radial part (C.2) of each
operator term (C.5) of the UCOM transformed Malflied-Tjon V V_{NN} potential [35].

Term	γ_i [fm^{-1}]	κ_i [fm^2]	Term	γ_i [fm]	κ_i [fm^2]
V_c	12.0615649	0.001	T_r	0.0048797	0.040
	6.9548944	0.004		4.4652639	0.016
	4.5938999	0.016		1.0242148	0.064
	1.5692365	0.064		0.2123215	0.128
	0.0684969	0.128		0.4855731	0.256
	0.2954898	0.256		0.1459136	0.512
	-0.3882999	0.512		-0.0911690	0.768
	-0.2140002	1.024		0.0423697	1.024
	-0.0513097	2.048		-0.0096523	1.560
	0.0020267	3.072		0.0026643	2.048
	-0.0035886	4.096		-0.0001517	3.072
Term	γ_i [fm^{-1}]	κ_i [fm^2]	Term	γ_i [fm^3]	κ_i [fm^2]
T_p	-25.1110040	0.001	$T_{\vec{r}}$	0.0010597	0.016
	-8.0591920	0.004		-0.0801659	0.064
	-2.8301404	0.016		0.0563154	0.128
	-0.7378560	0.064		-0.1181166	0.256
	-0.9694262	0.128		-0.277750	0.512
	-1.4223256	0.256		0.0040732	1.024
	4.6797041	0.512		-0.0004244	2.048
	-6.8409021	0.768			
	5.6644282	1.024			
	-3.7329947	1.536			
	3.3334832	2.048			
	-2.1378830	2.560			
	0.7013693	3.072			
	-0.0466316	4.096			

Table C.3: The parameters γ_i and κ_i [34] determining the radial part (C.2) of each operator term (C.6) of the UCOM transformed Afnan-Tang S3M V_{NN} potential [35].

Term	γ_i [fm^{-1}]	κ_i [fm^2]	Term	γ_i [fm^{-1}]	κ_i [fm^2]	Term	γ_i [fm]	κ_i [fm^2]	Term	γ_i [fm^3]	κ_i [fm^2]
V_c	-0.0029357	2.00	T_p	0.1158416	0.750	$T_{\bar{r}}$	-0.0082271	0.500	T_r	0.0034347	0.500
	-0.0049225	1.00		0.1318780	0.700		-0.0733833	0.300		0.4716358	0.300
	-0.2089104	0.75		-0.7732964	0.600		-0.0780228	0.200		-0.3967991	0.200
	-0.0760462	0.50		-0.5044436	0.500		0.2141264	0.150		0.4591119	0.150
	-0.4632689	0.20		1.7292916	0.400		-0.1735748	0.100		-0.3828439	0.100
	3.2254556	0.10		1.7566863	0.300		0.0498074	0.050		0.6609182	0.050
	0.9594806	0.05		-0.0795525	0.250		-0.0994221	0.010		1.4397131	0.010
	0.8155171			-2.7482553	0.200		0.1056213	0.005		2.6033188	0.005
				-1.4513572	0.150		-0.1370753	0.001		21.4219625	0.001
				-3.3503734	0.100						
				8.5590782	0.075						
				-4.8663284	0.050						
V_c^σ	0.0015628	2.00	T_p^σ	-0.5581406	0.750	$T_{\bar{r}}^\sigma$	0.0145286	0.500	T_r^σ	-0.0134242	0.500
	0.0404015	1.00		0.5651690	0.700		0.0034416	0.300		-0.2152635	0.300
	0.0036147	0.75		1.0986365	0.600		0.0267688	0.200		0.3456548	0.200
	0.1426615	0.50		-1.1398884	0.500		-0.0510409	0.150		-0.2515286	0.150
	-0.2985189	0.35		-1.8836482	0.400		0.0234100	0.100		0.1057082	0.100
	0.5288508	0.20		2.8097234	0.300		-0.0001432	0.050		-0.0618081	0.050
	0.0224720	0.10		0.8623140	0.250		-0.0107496	0.010		-0.0142574	0.010
	-0.2606686	0.05		-4.5526914	0.200		0.0154212	0.005		0.0496490	0.005
				6.2336099	0.150		-0.0196858	0.001		1.2280378	0.001
				-6.0075756	0.100						
				3.0104519	0.075						
				-0.2560336	0.050						
V_c^τ	-0.0017851	2.00	T_p^τ	0.5129127	0.750	$T_{\bar{r}}^\tau$	0.0018880	0.500	T_r^τ	0.0073226	0.500
	0.0341583	1.00		-0.8229817	0.700		-0.0144841	0.300		-0.0585020	0.300
	-0.1045889	0.75		-0.2982977	0.600		0.1090859	0.200		-0.1295384	0.200
	0.4999580	0.50		1.7051646	0.500		-0.1299134	0.150		0.1855930	0.150
	-0.3293438	0.35		-0.6161632	0.400		0.0493661	0.100		-0.0431652	0.100
	0.3085573	0.20		-2.9206285	0.300		-0.0052587	0.050		0.0101528	0.050
	0.1041411	0.10		1.2564224	0.250		-0.0066201	0.010		0.0439270	0.010
	-0.2174211	0.05		3.0474881	0.200		0.0095530	0.005		0.1816626	0.005
				-2.9097208	0.150		-0.0134251	0.001		1.6667669	0.001
				3.9294926	0.100						
				-3.8651420	0.075						
				1.1486970	0.050						
$V_c^{\sigma\tau}$	-0.0001112	2.00	$T_p^{\sigma\tau}$	-0.0891321	0.750	$T_{\bar{r}}^{\sigma\tau}$	0.0082083	0.500	$T_r^{\sigma\tau}$	-0.0030896	0.500
	0.0372799	1.00		-0.0041741	0.700		0.0679274	0.300		-0.1364919	0.300
	-0.0504871	0.75		0.3570129	0.600		-0.0904771	0.200		0.1064467	0.200
	0.3213098	0.50		0.1431286	0.500		0.0363881	0.150		-0.0307065	0.150
	-0.3139314	0.35		-0.9779069	0.400		-0.0027009	0.100		0.0298981	0.100
	0.4187040	0.20		-0.2224863	0.300		-0.0086848	0.050		-0.0253245	0.050
	0.0633065	0.10		0.7510455	0.250		0.0124871	0.010		0.0142081	0.010
	-0.2390449	0.05		-0.0597689	0.200		-0.0165555	0.005		0.1165171	0.005
				1.0787701	0.150			0.001		1.4464953	0.001
				-0.6272845	0.100						
				-0.6688474	0.075						
				0.4958705	0.050						

Table C.4: The parameters a_i, b_i, c_i, and β_i of the YNG-JA, JB, ND, NF, and NS $V_{\Lambda N}$ potentials [21] determining the shape of the radial part (C.7) in different spin-parity channels.

			YNG-JA						
Ch	a_i [MeV]	b_i [MeV.fm]	c_i [MeV.fm^2]	β_i [fm]	Ch	a_i [MeV]	b_i [MeV.fm]	c_i [MeV.fm^2]	β_i [fm]
^1E	-25.82	-12.51	2.437	1.25	^1O	-14.54	3.615	-0.875	1.25
^1E	-389.4	401.2	-136.0	0.70	^1O	144.7	27.50	-5.000	0.70
^1E	859.0	-303.2	188.8	0.45	^1O	734.6	76.37	3.125	0.45
^3E	-45.01	4.620	0.7500	1.25	^3O	-25.91	5.410	0.500	1.25
^3E	-296.6	218.3	-92.50	0.70	^3O	248.1	210.9	-123.1	0.70
^3E	1094	-504.6	230.0	0.45	^3O	615.3	-1260	734.8	0.45

			YNG-JB						
Ch	a_i [MeV]	b_i [MeV.fm]	c_i [MeV.fm^2]	β_i [fm]	Ch	a_i [MeV]	b_i [MeV.fm]	c_i [MeV.fm^2]	β_i [fm]
^1E	-44.36	3.435	-2.875	1.25	^1O	-10.25	3.008	-0.7625	1.25
^1E	0.2853	-2.842	0.1562	0.70	^1O	134.2	45.22	-8.125	0.70
^1E	491.9	122.3	39.38	0.45	^1O	739.4	25.85	13.75	0.45
^3E	-32.77	-1.595	1.375	1.25	^3O	-21.36	10.29	-3.125	1.25
^3E	-430.9	379.7	-135.6	0.70	^3O	347.6	-48.10	22.50	0.70
^3E	967.8	-599.4	248.1	0.45	^3O	-10.33	277.5	-63.75	0.45

			YNG-ND						
Ch	a_i [MeV]	b_i [MeV.fm]	c_i [MeV.fm^2]	β_i [fm]	Ch	a_i [MeV]	b_i [MeV.fm]	c_i [MeV.fm^2]	β_i [fm]
^1E	-12.05	2.163	-0.8488	1.50	^1O	-6.05	0.8124	-0.2266	1.50
^1E	-302.6	125.7	-48.33	0.90	^1O	-103.1	21.65	-5.016	0.90
^1E	1178	-350	231.6	0.50	^1O	-334.4	542.6	-98.69	0.50
^3E	-12.38	2.98	-0.7153	1.50	^3O	-9.714	2.041	-0.5137	1.50
^3E	-256.7	129.1	-47.43	0.90	^3O	-108.7	20.20	-5.033	0.90
^3E	872.4	-284.8	167.7	0.50	^3O	1023	171.8	-30.58	0.50

			YNG-NF						
Ch	a_i [MeV]	b_i [MeV.fm]	c_i [MeV.fm^2]	β_i [fm]	Ch	a_i [MeV]	b_i [MeV.fm]	c_i [MeV.fm^2]	β_i [fm]
^1E	-10.71	3.086	-1.205	1.50	^1O	-3.446	0.622	-0.1691	1.50
^1E	-270.5	123.1	-44.91	0.90	^1O	1.328	0.3701	-0.3445	0.90
^1E	806.2	-188.9	141.6	0.50	^1O	1284	387.4	-88.63	0.50
^3E	-12.16	2.776	0.1632	1.50	^3O	-9.047	3.361	-0.8142	1.50
^3E	-273.3	146	-57.09	0.90	^3O	-59.88	16.42	-3.890	0.90
^3E	877.8	-242.4	177.2	0.50	^3O	748.8	411.2	-117.8	0.50

			YNG-NS						
Ch	a_i [MeV]	b_i [MeV.fm]	c_i [MeV.fm^2]	β_i [fm]	Ch	a_i [MeV]	b_i [MeV.fm]	c_i [MeV.fm^2]	β_i [fm]
^1E	-9.019	4.616	-2.101	1.50	^1O	-1.319	0.3964	0.03037	1.50
^1E	-253.9	151.5	-43.78	1.00	^1O	-2.478	-2.176	1.934	1.00
^1E	704.0	-421.8	126.6	0.55	^1O	993.6	-12.75	39.08	0.55
^3E	-9.783	0.903	1.061	1.50	^3O	-4.475	2.164	-1.773	1.50
^3E	-176.0	131.8	-39.86	1.00	^3O	10.21	-15.28	11.12	1.00
^3E	595.4	-375.0	141.8	0.55	^3O	-581	426	-0.1282	0.55

Appendix D

FMD program

In this Appendix, we give a brief introduction to the FMD program developed in this work. The main goal of the code is to calculate the ground as well as excited states of light hypernuclei and to study their structure with the FMD model. The program was written so that we were able to test critical parts of our code by comparing each step as well as results of nuclear calculations with a similar FMD code developed in GSI. The tested FMD program was then extended to hypernuclei.

We choose the object oriented C++ as the main programming language because it is suitable for the description of the complicated structure of the FMD calculations and because it simplifies future development of our code. However, some parts of the program were written in FORTRAN F77. In our calculations, we used the Linear Algebra PACkage (LAPAC) and Basic Linear Algebra Subprograms (BLAS) numerical libraries (FORTRAN F90) as well as the Eigen project libraries (C++) [82]. We implemented two optimization procedures - the DONLP2 which is based on the Sequenetial Quadratic Programming method for nonlinear optimization with equality or inequality constraints (SQP) [44] and the Limited memory Broyden-Fletcher-Goldfarb-Shanno algorithm with Box constraints (L-BFGS-B) [71]. The SQP serves as the main minimization algorithm in our FMD program. The L-BFGS-B was implemented to test the more advanced SQP algorithm.

All procedures and functions are called from different header files to keep the FMD code clear and easy-to-other improvements. Each header file *"header.h"* declares thematically close procedures and functions whose source code is written in the relevant *"header.cpp"* file. In Table D.1, we give the general overview of all components of the FMD program together with their brief description. The compilation process is done automatically by running the bash script *"FMD1comp.sh"*. The setup of the compilation process, linkage of relevant libraries, and cooperation between the parts of the code written in different programming languages are defined here. The bash script creates the executable file of the FMD program called *"FMD11"*.

Table D.1: The description of the content of the individual files of the FMD program. The V_{NN} ($V_{\Lambda N}$) potential parameters from Tables C.1-C.3 (Table C.4) are stored in the V_{NN} ($V_{\Lambda N}$) input files.

FMD	File	Description	Type
Fermionic Molecular Dynamics source files	FMD11.cpp	main body of the program	C++
	particle.h	object class to store the single-particle parameters	C++
	particle.cpp	source file to particle.h	C++
	matrices.h	procedures to calculate the auxiliary matrices	C++
	matrices.cpp	source file to matrices.h	C++
	interaction.h	procedures working with interactions	C++
	interaction.cpp	source file to interaction.cpp	C++
	observables.h	procedures calculating observables	C++
	observables.cpp	source file to observables.h	C++
	mathematics.h	mathematical functions	C++
	mathematics.cpp	source file to mathematics.h	C++
	lbfgsb1.f	L-BFGS-B algorithm [71]	f77
	timer.f	timer to L-BFGS-B algorithm	f77
	libdonlp2.a	library containing DONLP2 algorithm (SQP) [44]	f77
	donlp2def.f	file defining parameters of the DONLP2 algorithm	f77
	variation.f	file connecting C++ FMD code with DONLP2 (f77)	f77
	wigner.f	procedure calculating small Wigner d-functions	f77
	FMD1comp.sh	compilation script	bash
V_{NN} input files	VOLV2M0.0.txt	Volkov V2 M=0.0 parameters	txt
	VOLV2M0.0C.txt	Volkov V2 M=0.0 parameters + Coulomb	txt
	VOLV2M0.6.txt	Volkov V2 M=0.6 parameters	txt
	VOLV2M0.6C.txt	Volkov V2 M=0.6 parameters + Coulomb	txt
	MTV.txt	Malfliet-Tjon V parameters	txt
	MTVC.txt	Malfliet-Tjon V parameters + Coulomb	txt
	ATS3M.txt	Afnan-Tang S3M parameters	txt
	ATS3MC.txt	Afnan-Tang S3M parameters +Coulomb	txt
$V_{\Lambda N}$ files	YNG_JA	YNG JA parameters	txt
	YNG_JB	YNG JB parameters	txt
	YNG_ND	YNG ND parameters	txt
	YNG_NF	YNG NF parameters	txt
	YNG_NS	YNG NS parameters	txt
	pottrans.cpp	program generating $V_{\Lambda N}$ input file for the given k_{F}	C++
	input.txt	initial parameters of the many-body FMD state $|Q\rangle$	txt

Running the FMD program

First, we must compile the FMD code with the properly adjusted total number of particles: protons, neutrons, and Λ's. This is done in the files *"FMD11.cpp"* and *"matrices.h"* described in Table D.1. The number of Λ's has only two options - one and zero. The FMD executable file *"FMD11"* has to be loaded with the following arguments

$$FMD11 \quad -NNpotential \quad -\Lambda Npotetial \quad -none \quad -P, \tag{D.1}$$

where *"NNpotential"* and *"ΛNpotential"* denote the name of the V_{NN} and $V_{\Lambda N}$ input files in Table D.1, respectively. In the case of an ordinary nuclear system, the FMD program does not use the $V_{\Lambda N}$ input file during the calculation, however, an arbitrary $V_{\Lambda N}$ file has to be loaded. The *none* argument tells the FMD program to load the initial parameters of the FMD trial state $|Q\rangle$ (2.1) from the input file *"input.txt"*. The P argument controls the type of variation - $P = 0$ stands for the variation of the basic FMD trial state, $P = 1$ stands for the variation of the even parity projected FMD trial state, and $P = -1$ stands for the variation of the odd parity projected FMD trial state.

When the program starts running, it first loads the initial parameters of the many-body FMD state $|Q\rangle$ (2.1), V_{NN} parameters, $V_{\Lambda N}$ parameters, and the information about the type of variation P. Then it enters the optimization procedure.

The SQP algorithm minimizes the expectation value of the total Hamiltonian $\hat{H}$ (2.18) with respect to parameters of the many-body state $|Q\rangle$ and the equality bounds $< \hat{X}_{cm} >^2 = 0$, $< \hat{P}_{cm} >^2 = 0$, and box constraints $Re(a_k) > 0$ (2.19). In each iteration, the expectation value of the Hamiltonian and its gradient with respect to the parameters of the many-body FMD state are evaluated for a given set of variational parameters proposed in this iteration.

Once the minimization procedure is terminated, the FMD program stores the resulting variational parameters of the many-body FMD state $|Q\rangle$. Subsequently, the observables listed in Table D.2 of the even (odd) parity projected state $|Q; +\rangle$ $(|Q; -\rangle)$ (2.22) and the state without the parity projection $|Q\rangle$ are calculated. The resulting variational parameters and calculated expectation values are summarized in a text file

$$observables\_intrinsic\_''NNpotential''\_''\Lambda Npotential''\_n\_p\_l\_P''0, 1, -1'', \tag{D.2}$$

where n ,p, l are numbers of neutrons, protons, and Λ in the variated many-body FMD state $|Q\rangle$, respectively, and *"0,1,-1"* denote the type of the variational process.

Table D.2: The calculated observables of the many-body FMD states.

Calculated observables	
E_{B}	binding energy (2.19)
E_{i}	individual operator contributionss of $\hat{H}$ (2.18) to the E_{B}
R_{T}	total mass rms radius (A.10)
R_p	proton mass rms radius (A.12)
R_n	neutron mass rms radius (A.12)
R_Λ	Λ mass rms radius (A.12)
R_{core}	mass rms radius of the nuclear core (A.14)
R_{charge}	charge rms radius (A.15)

The total angular momentum projection described in Section 2.4.2 is performed after the minimization. In case of odd (even) number of particles the FMD program determines the parity projected angular momentum eigenstates $\left|Q; J^{+/-}\right\rangle$ as well as eigenstates without the parity projection $|Q; J\rangle$ for J=1/2 (0), 3/2 (1), 5/2 (2), 7/2 (3), and 9/2 (4). The expectation values listed in Table D.2 of each total angular momentum and parity eigenstate obtained with a sufficient numerical accuracy are summarized in the text file

$$ang\_proj\_observables\_''NNpotential''\_''\Lambda Npotential''\_n\_p\_l\_P''0, 1, -1''.$$

$$(D.3)$$

Further improvements of the FMD program

The analytical calculations of gradients during the minimization process described in Appendix B are the most critical, time consuming part of the program. The computational complexity of these calculations considerably increases with the size of the system. Therefore, further improvements in this part of the program are needed. In the future, we plan to improve the efficiency of our calculations by applying parallelization techniques which will allow us to consider heavier nuclear as well as hypernuclear systems.

Bibliography

[1] J. Beringer et al. (Particle Data Group), Phys. Rev. **D 86** (2012) 010001.

[2] P. Bydžovský, A. Gal, J. Mareš (Eds.), *Topics in Strangeness Nuclear Physics*, Lecture Notes in Physics **724** (Springer 2007).

[3] S. Bart et al., Phys. Rev. Lett. **83** (1999) 5238.

[4] D. J. Prowse, Phys. Rev. Lett. **17** (1966) 782.

[5] M. Danysz et al., Nucl. Phys. **49** (1963) 121.

[6] S. Aoki et al., Prog. Theor. Phys. **85** (1991) 87.

[7] M. Danysz, J. Pniewski, Phil. Mag. **44** (1953) 348.

[8] D. H. Davis, Nucl. Phys. **A 754** (2005) 3c.

[9] O. Hashimoto, H. Tamura, Prog. in Part. and Nucl. Phys. **57** (2006) 564.

[10] H. Tamura, M. Ukai, T. O. Yamamoto, T. Koike, Nucl. Phys. **A 881** (2012) 310.

[11] M. Agnello et al. (The FINUDA Collaboration), Phys. Lett. **B 622** (2005) 35.

[12] T. R. Saito et al., Nucl. Phys. **A 881** (2012) 218.

[13] P. Achenbach et al. (A1 Collaboration), Int. J. Mod. Phys. **E 19** (2010) 2624.

[14] H. Tamura et al., Nucl. Phys. **A 670** (2000) 249.

[15] K. Miyagawa, W. Glöcke, Phys. Rev. **B 48** (1993) 2576.

[16] A. Nogga, H. Kamada, W. Glöcke, Phys. Rev. Lett. **88** (2002) 172501.

[17] A. Nogga, Nucl. Phys. **A 914** (2013) 140.

[18] E. Hiyama et al. , Prog. Theor. Phys. **97** (1997) 881.

[19] E. Hiyama, Nucl. Phys. **A 914** (2013) 130.

[20] E. Hiyama et al., Phys. Rev. Lett. **104** (2010) 212502.

[21] Y. Yamamoto et al., Prog. Theor. Phys. Suppl. **117** (1994) 361.

[22] D. Gazda et al., Few-Body Systems **55** (2014) 857.

[23] R. Wirth et al., Phys. Rev. Lett. **113** (2014) 192502.

[24] D. J. Millener, Nucl. Phys. **A 914** (2013) 109.

[25] M. Isaka, M. Kimura, A. Dote, A. Ohnishi, Phys. Rev. **C 83** (2011) 044323.

[26] M. Isaka et al., Phys. Rev. **C 89** (2014) 024310.

[27] J. Mareš, B. K. Jennings, Phys. Rev. **C 49** (1994) 2472.

[28] D. E. Lanskoy, Nucl. Phys. **A 639** (1998) 157c.

[29] J. Cugnon, A. Lejeune, H.-J. Schulze, Phys. Rev. **C 62** (2000) 064308.

[30] R. Roth, T. Neff, H. Hergert, H. Feldmeier, Nucl. Phys. **A 745** (2004) 3.

[31] M. Chernykh et al., Phys. Rev. Lett. **98** (2007) 032501.

[32] H. Feldmeier, Nucl. Phys. **A 515** (1990) 147.

[33] H. Feldmeier, K. Bieler, J. Schnack, Nucl. Phys. **A 586** (1995) 493.

[34] T. Neff, *Fermionische Molekulardynamik mit Konfigurationsmischungen und realistischen Wechselwirkungen*, Master's thesis, (TU Darmstadt, 1998).

[35] H. Feldmeier, T. Neff, R. Roth, J. Schnack, Nucl. Phys. **A 632** (1998) 61.

[36] R. Guardiola, A. Faessler, H. Müther, A. Polls, Nucl. Phys. **A 371** (1981) 79.

[37] R. A. Malfliet, J. A. Tjon, Nucl. Phys. **A 127** (1969) 161.

[38] T. Neff, *Short-Ranged Central and Tensor Correlations in Nuclear Many-Body Systems*, Ph.D. thesis, (TU Darmstadt, 2002).

[39] T. Neff, H. Feldmeier, Nucl. Phys. **A 738** (2004) 357.

[40] T. Neff, H. Feldmeier, R. Roth, Nucl. Phys. **A 752** (2005) 321c.

[41] H. Feldmeier, J. Schnack, Rew. Mod. Phys. **72** (2000) 3655.

[42] Y. Kanada-En'yo, H. Horiuchi, Prog. Theor. Phys. Supp. **142** (2001) 205.

[43] H. Horiuchi, K. Ikeda (Eds.), *Cluster models and other topics*, (World Scientific Publishing, 1986).

[44] P. Spellucci, Math. Prog. **82** (1998) 413.

[45] T. Ring, P. Schuck, *The Nuclear Many- Body Problem*, (Springer, 2004).

[46] T. Neff, H. Feldmeier, Eur. Phys. J. Special Topics **156** (2008) 69.

[47] R. E. Marshak, S. Okubo, Ann. Phys. **4** (1958) 166.

[48] R. B. Wiringa, R. A. Smith, T. L. Ainsworth, Phys. Rev. **C 29** (1984) 1207.

[49] R. B. Wiringa, V. G. J. Stoks, R. Schiavilla, Phys. Rev. **C 51** (1995) 38.

[50] R. B. Wiringa, S. C. Pieper, J. Carlson, V. R. Pandharipande, Phys. Rev. **C 62** (2000) 014001.

[51] R. B. Wiringa, S. C. Pieper, Phys. Rev. Lett. **89** (2002) 182501.

[52] A. R. Bodmer, Q. N. Usmani, J. Carlson, Phys. Rev. **C 29** (1984) 684.

[53] P. M. M. Maessen, T. A. Rijken, J. J. de Swart, Phys. Rev. **C 40** (1989) 2226.

[54] T. A. Rijken, V. G. J. Stocks, Y. Yamamoto, Phys. Rev. **C 59** (1999) 21.

[55] T. A. Rijken, Y. Yamamoto, Phys. Rev. **C 73** (2006) 044007.

[56] T. A. Rijken, Y. Yamamoto, Phys. Rev. **C 73** (2006) 044008.

[57] J. Haidenbauer, U.-G. Meißner, Phys. Rev. **C 72** (2005) 044005.

[58] Y. Akaishi, T. Harada, S. Shinmura, Khin Swe Myint, Phys. Rev. Lett. **84** (2000) 3539.

[59] H. Nemura, Y. Akaishi, Y. Suzuki, Phys. Rev. Lett. **89** (2002) 142504.

[60] S. Weinberg, Phys. Lett. **B 251** (1990) 288.

[61] S. Weinberg, Nucl. Phys. **B 363** (1991) 3.

[62] S. Weinberg, Phys. Lett. **B 295** (1992) 114.

[63] H. Polinder, J. Haidenbauer, U.-G. Meißner, Nucl. Phys. **A 779** (2006) 244.

[64] J. Haidenbauer et al., Nucl. Phys. **A 915** (2013) 24.

[65] D. R. Entem, R. Machleidt, Phys. Rev. **C 68** (2003) 041001.

[66] A. Volkov, Nucl. Phys. **74** (1965) 33.

[67] I. R. Afnan, Y. C. Tang, Phys. Rev. **175** (1968) 1337.

[68] B. Holzenkamp, K. Holinde, J. Speth, Nucl. Phys **A 500** (1989) 485.

[69] E. R. Cohen, B. N. Taylor, Rev. Mod. Phys. **59** (1986) 1121.

[70] P. J. Mohr, B. N. Taylor, D. B. Newell, Rev. Mod. Phys. **84** (2012) 1527.

[71] R. H. Byrd, P. Lu, J. Nocedal, SIAM J. on Sc. and Stat. Comp. **16,5** (1995) 1190.

[72] T. Neff, *private communication.*

[73] J. E. Purcell et al., Nucl. Phys. **A 848** (2010) 1.

[74] D. Shiner, R. Dixson, V. Vedantham, Phys. Rev. Lett. **74** (1995) 3553.

[75] D. H. Davis, Contemp. Phys. **27** (1986) 91.

[76] M. Bedjidian et al., Phys. Lett. **B 83** (1979) 252.

[77] M. Isaka, *private communication*

[78] E. Hiyama, Y. Yamamoto, T. Motoba, M. Kamimura, Phys. Rev. **C 80** (2009) 054321.

[79] National Nuclear Data Center, Chart of nuclides [online] URL:<http://www.nndc.bnl.gov> [cit. 2.5.2015].

[80] I. Sick, Phys. Rev. **C 77** (2008) 041302(R).

[81] D. R. Tilley et al., Nucl. Phys. **A 708** (2002) 3.

[82] The Eigen project [online] URL:<http://eigen.tuxfamily.org> [cit. 2.5.2015].